Faculty of Aerospace Engineering
Aerodynamics and Wind Energy

Numerical Study On The Impact Of Self Induced Gravity Waves On Offshore Wind Farms

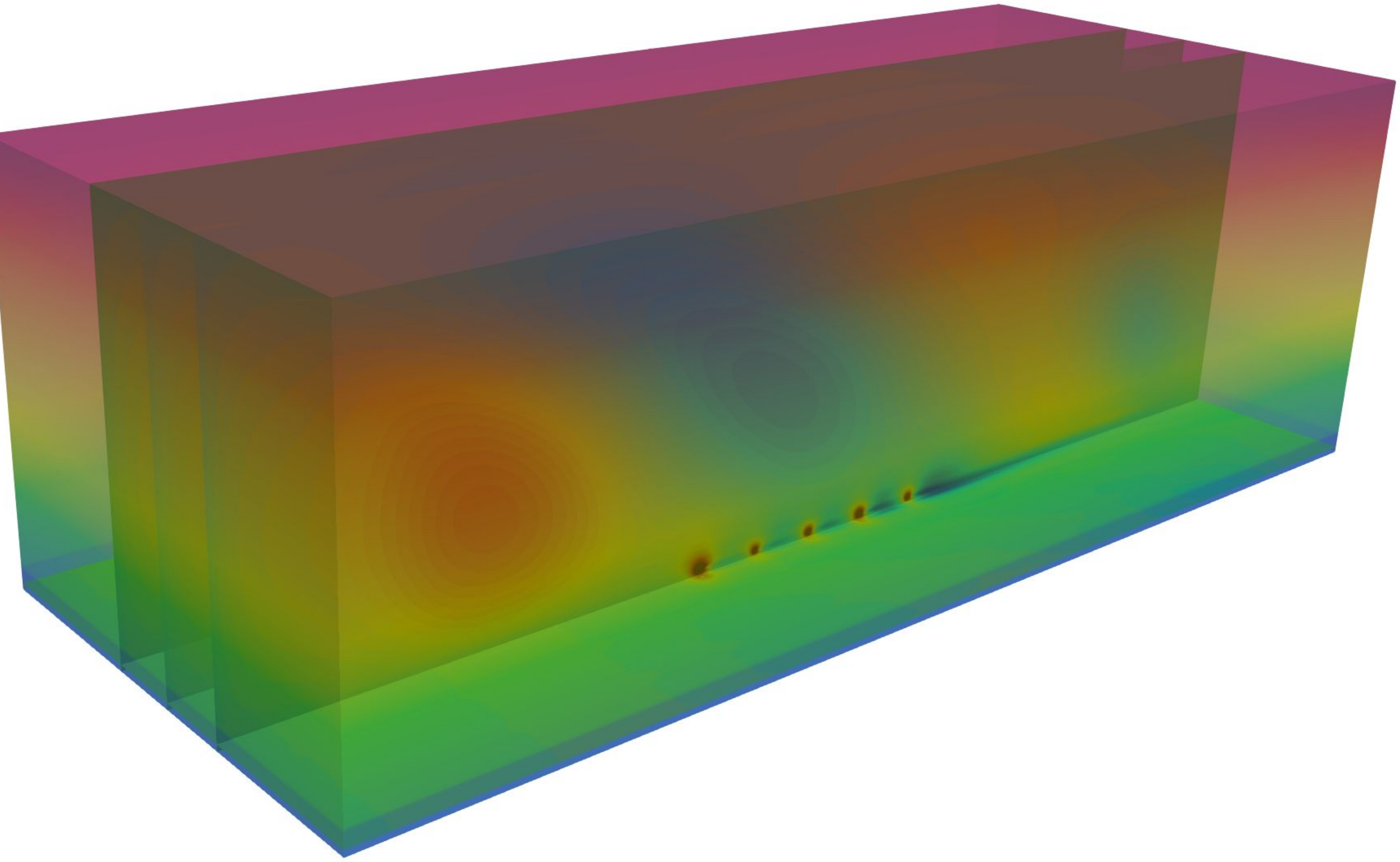

Hrishikesh Sivanandan

Master Thesis

Supervisors:
Prof.dr. S.J. (Simon) Watson
Dr.ir. DJN (Dries) Allaerts

Numerical Study On the Impact of Self Induced Gravity Waves On Offshore Wind Farms

by

Hrishikesh Sivanandan

to obtain the degree of Master of Science (Aerospace Engineering)
at the Delft University of Technology,
to be defended publicly on Wednesday, September 22, 2021 at 08:30 AM.

Student number:	4861442	
Project duration:	August 15, 2020 – September 22, 2021	
Thesis committee:	Prof. Dr. S.J. Watson,	TU Delft, supervisor
	Dr. Ir. D. Allaerts,	TU Delft, co-supervisor
	Dr. Ir. R.P. Dwight,	TU Delft, committee member
	Dr. Ir. S. Basu,	TU Delft, committee member

Dedicated to Amma and my beloved parents

Acknowledgements

My journey at Delft has always been similar to the convergence of a CFD RANS simulation. Throughout the last three years, I have always heard many forms of the same message. On seeing me overwhelmed, my loved ones always said, ”take it one step at a time”. Moreover, my thesis supervisors kept repeating this statement in another way. Almost every meeting I was told, ”Hrishikesh, change one parameter at a time”. Well, this is perhaps the biggest life lesson that I have been taught here at TU Delft.

First and foremost, I am grateful to Professor Simon Watson for taking me in as a master thesis student under his supervision and allowing me to learn and grow throughout the phase of the master thesis. Further, I am thankful to Professor Dries Allaerts for his patience, guidance and motivation throughout these testing times. Furthermore, I am grateful to Ir. Julia Steiner for providing me with the skeleton of the two CFD solvers being used in the present study.

Secondly, I am grateful to my parents for their everlasting love, support, faith and kindness throughout my life. I can never fully repay the kindness and love that you both have showered upon me in this lifetime. Further, I am grateful to my soul mate, Deepti Gnanaseelan, for her continued love, patience and support throughout the phase of my master studies. Thank you for lighting up my life with your presence. Furthermore, I am grateful to Dr. Kala Raj and Dr. C Gnanaseelan, for their love, emotional support and immense trust in me. Moreover, I am also indebted to Arjav Anand Amur, Ghanshyam Chandrashekhar, Ravi Tej Gadamsetti and Prasath Varadharajan for allowing me to stay at their homes in the final days of my thesis.

Also, I am grateful to Dr. V. Ratna Kishore for helping me understand Openfoam during the initial master thesis days. Further, I am thankful to Prof. Dr. Ir. Murali Rangarajan, for being there throughout all these phases and inspiring me to outgrow myself at each difficult moment. Also, I express my gratitude to Ms. Aneesha Kaza for helping me layout the initial plan and task distribution of my master thesis. I am thankful to Abhratej Sahoo, Haris Shahzad, Ata Onur Başkaya, Akash Pandey and Bora Orçun Çakır for being there as true pillars of support through the initial days of my master studies at TU Delft. I am eternally grateful to have been your peer in most of the group assignments. I am grateful to Manish Gunalan, Meghana Amaregouda, Vaibhav Viswanath, Sumeet Bhonsle and Dr. Anupama Nair for always being there to emotionally support me through this entire journey. Furthermore, I am indebted to Anirudh Shukla for inspiring me to join TU Delft.

Lastly, but most importantly, I would like to thank Amma, the embodiment of divinity, for making these miracles happen. I am always grateful for your abundant/ omnipresent grace and inspiration to push forward in these testing times.

Hrishikesh Sivanandan
Delft,
September 2021

Contents

List of Figures

List of Tables

Nomenclature

ϵ	Turbulent Kinetic Energy Dissipation Rate
θ	Potential Temperature
Fr	Froude Number
g	Acceleration due to gravity
k	Turbulent Kinetic Energy
Ri	Richardson Number

1

Introduction

The history of wind energy dates back to the end of 19^{th} century, when Charles Brush created electricity from the 'brush mill' (see Figure 1.1a). Similar efforts were undertaken by Poul la Cour who studied optimizing wind turbine aerodynamics, and investigated whether electrolysis would provide a method to store electricity. Further, towards the mid-twentieth century, there was widespread urbanization of the rural areas due to the rising population. This led to the idea of generating electricity from wind power. The manifestation of this newborn idea was a prototype of the popular Smith and Putnam turbine, having a capacity of > 1MW (see Figure 1.1b).

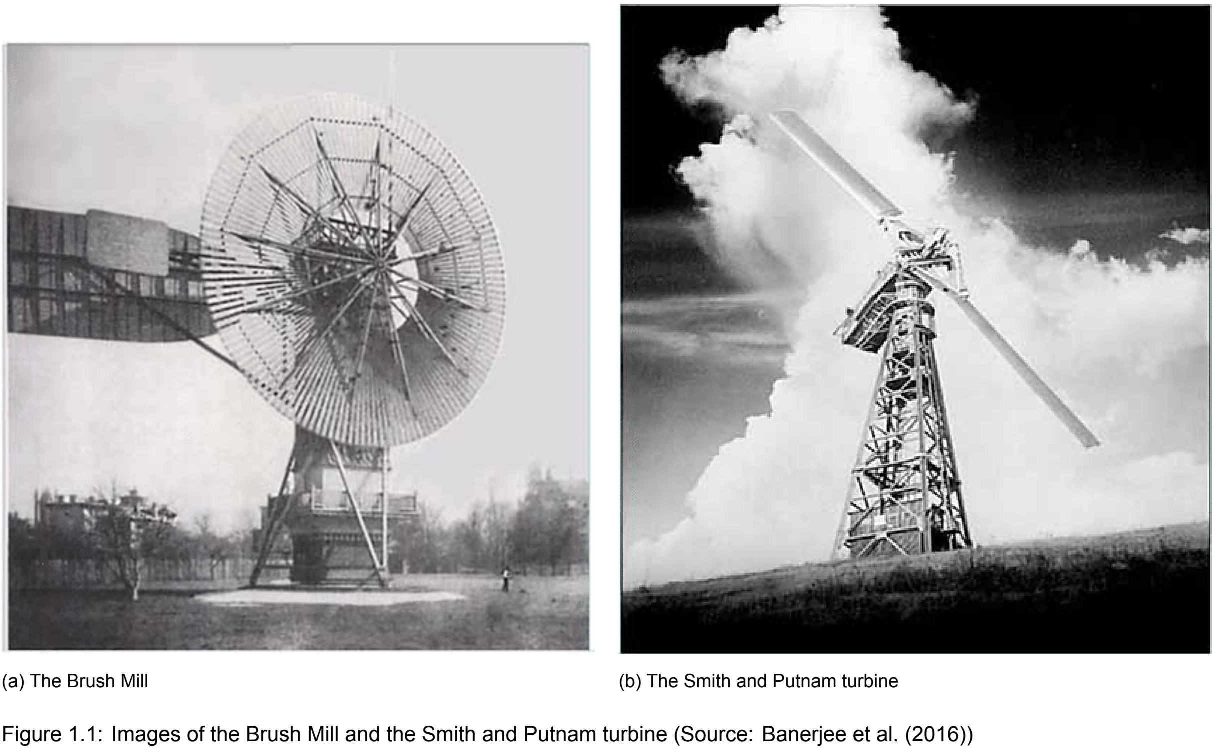

(a) The Brush Mill

(b) The Smith and Putnam turbine

Figure 1.1: Images of the Brush Mill and the Smith and Putnam turbine (Source: Banerjee et al. (2016))

Further, in the 1970s and 1980s, the oil crises lead to renewed interest in wind turbine technology. Over the years, from the 1980s to the 2000s, there was a gradual and also an abrupt scaling up of wind turbines. Large organizations such as Boeing and NASA joined the quest to scale up wind turbines. While the big organizations were trying to abruptly scale up wind turbines, the smaller counterparts were gradually scaling up their turbines from small sizes to bigger ones. This gradual scaling up encompassed experimentation with prototypes built, implementing customer feedback and site analysis. This proved to be a more successful approach, as the design was continuously improved based upon previous design experiences and turbines built.

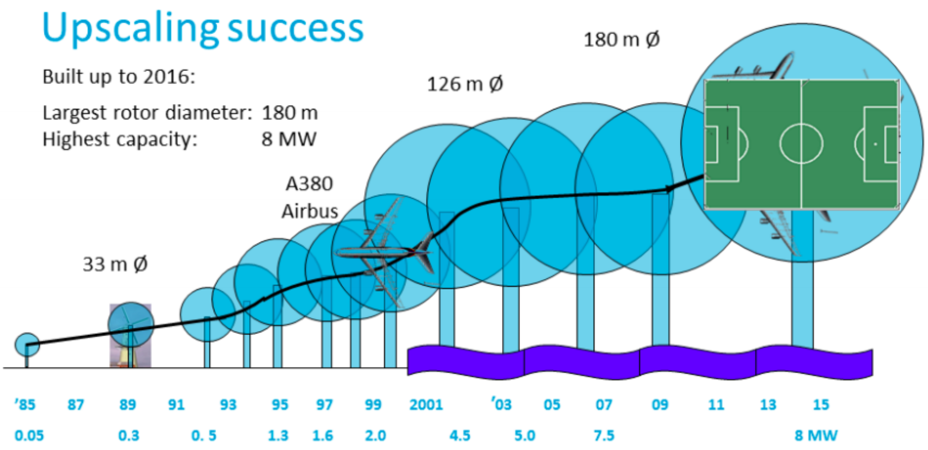

Figure 1.2: Gradual scaling up of rotor diameter with time *(Reproduced from TU Delft reader - Introduction to Wind Turbines (Physics and Technology))*

In recent times, it has been customary to place many wind turbines together, in order to minimize costs related to grid infrastructure (transmission and distribution), and also to reduce the costs related to operation and maintenance. These groups of wind turbines are commonly referred to as wind farms. While the first wind farm installed at Crotched Mountain, in southern New Hampshire in 1980 had a total capacity of 0.6MW, the recent onshore wind farm at Gansu, China has an installed capacity as high as 7965 MW (≈ 8 GW). This sheds light on how wind energy has become a popular choice of generating electricity.

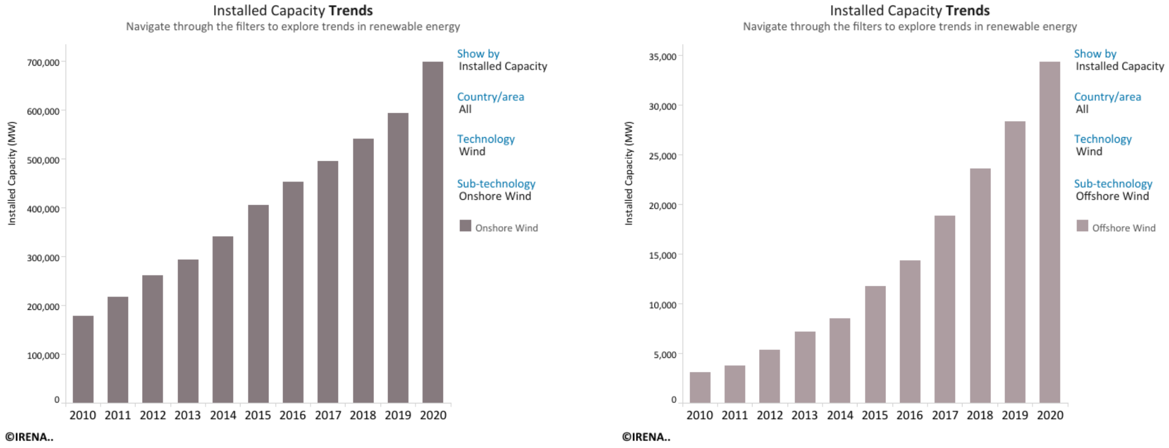

(a) Total installed onshore wind capacity

(b) Total installed offshore wind capacity

Figure 1.3: Reproduced from International Renewable Energy Agency IRENA Statistics

Further, in countries with low land area and/or large population density, difficulties arise in finding suitable sites for onshore wind farms. In these nations, offshore wind energy has become popular. In the recent years, despite the COVID-19 pandemic, there has been an increase in the installed capacity of onshore and offshore wind energy as shown in Figure 1.3a, and Figure 1.3b respectively.

However, before setting up a wind farm, it is imperative to thoroughly assess the on-site wind resource behaviour. This is required in order to optimize the turbine layout to maximize power generation, minimize fatigue loading of turbines and reduce uncertainties in power production forecasts. While the wind characteristics at a particular site is available through recorded meteorological data from weather centres and satellite data, these are not always available at the exact location of the prospective farm. This gap is bridged using prediction techniques like the wind atlas methodology that enables the transfer of detailed wind resource information from one location (predictor) to the other (the predicted). The predicted wind atlas is either observational (the predictor is a real world meteorological station) or numerical (the predictor is a grid point in a mesoscale modelling domain). Experimental observation campaigns using LIDAR's at Østerild, Perdigão, Alaiz, Kassel and other locations as a part of the New European Wind Atlas project (Mann et al., 2017). Further, other projects like the European Wind Atlas (Troen and Lundtang Petersen, 1989), Russian Wind Atlas (Starkov et al., 2000) helped predict the wind resource behaviour at multiple sites across the world.

Further, in case of large wind farms, Frandsen (1992) proposed a theory that the energy extracted by the wind farm causes a flow deceleration within the ABL, leading to a lower availability of incoming kinetic energy at each individual turbine. This theory was further supported by Calaf et al. (2010), who performed Large Eddy Simulations (LES) on an infinitely large wind farm. Further, Meneveau and Charles (2011) showed that the ABL - wind farm interaction has a significant impact on the power production for moderately large wind farms such as Nysted and Horns Rev I.

Although the flow physics within the Atmospheric Boundary Layer (ABL) has been extensively studied over many years, the interaction of the ABL and large wind farms is a new and emerging field of research (Allaerts, 2016). In this regard, understanding the role of atmospheric conditions in altering the wind characteristics within an operational farm through experimental observations is very challenging, as the atmosphere is constantly changing over time. It is affected by the presence of orography, land to sea transition and other complex weather phenomena. Thus, Computational Fluid Dynamics (CFD) proves to be an ideal tool, that provides a controlled environment for systematic variation of each atmospheric factor affecting the flow. The present dissertation investigates one such complex ABL - wind farm interaction, involving the excitation of Atmospheric Gravity Waves (AGWs) by wind farms. This would be achieved by performing numerical simulations using an open-source CFD code based on the OpenFOAM and SOWFA environments.

At this point, it is necessary to introduce certain basic concepts pertaining to the atmosphere, which are relevant to the present thesis. These include the ABL, thermal stability, the Conventionally Neutral Boundary Layer (CNBL), the capping inversion.

1.1. The Atmospheric Boundary Layer

The term *boundary layer* is defined in Anderson (2011) as :

"The thin region of flow adjacent to a surface, where the flow is retarded by the influence of friction between the solid surface and the fluid"

In the case of the atmosphere, the earth surface or sea surface forms a solid boundary for the wind flow, which further gives rise to the Atmospheric Boundary Layer (ABL) (Allaerts, 2016). The ABL is the lowest part of the atmosphere that is directly affected by the presence of the surface of the earth (Hu, 2015). Alternatively, Stull (1988) defines the ABL

"as that part of the troposphere that is directly influenced by the presence of the earth's surface, and responds to surface forcing with a timescale of about an hour or less".

The flow physics within the ABL is quite complex, involving three-dimensional turbulence. Turbulence is generated within the atmosphere through wind shear and is adversely impacted by buoyancy, which can create or dissipate the same. The thermal stability within the atmosphere has a close relation to the ABL depth and structure (Allaerts, 2016).

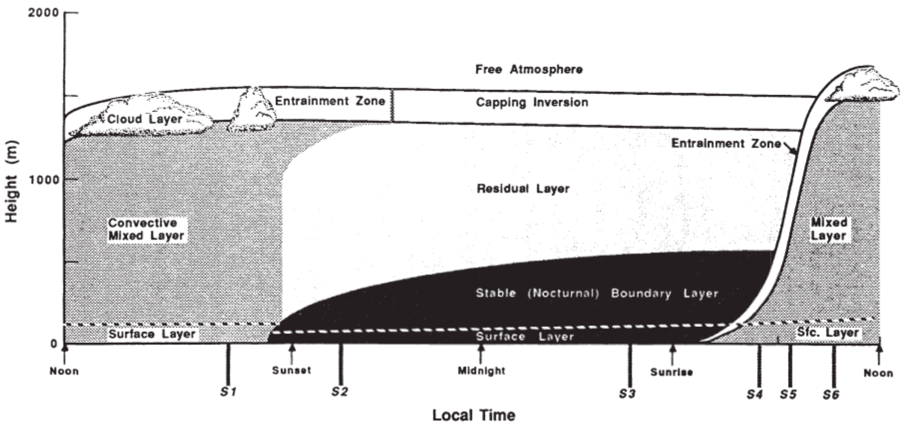

Figure 1.4: The structure of the ABL during a diurnal cycle in a region of high pressure over land. (Reproduced from the work of Stull (1988))

1.2.Thermal stability

Buoyancy plays a pivotal role in the creation and destruction of turbulence in the ABL. This is because it can either accelerate or decelerate vertical motions of air parcels, which manifests turbulence generation or destruction (Allaerts, 2016). The direction of the buoyancy force is dependent on the magnitude of the background temperature lapse rate with respect to the adiabatic lapse rate. The difference between these gives rise to the three stability types - unstable, neutral and stable. These are shown in Figure 1.5.

To further understand the tendency of the air parcel in each of the three stability conditions, consider the vertical displacement of the air parcel sans heat exchange with its surroundings (the neutral case). The parcel would compress or expand, followed by a density and temperature change in accordance with the universal gas law. Since the air parcel's density remains equal to its surroundings always, it does not experience a buoyancy force. Thus, the motion of the air parcel remains unaffected (as the buoyancy force is absent). The neutral stability is observed when the decrease in background temperature with height matches the adiabatic lapse rate $g/c_p = 9.8K/km$ with g depicting the acceleration due to gravity, c_p depicting the specific heat of dry air at constant pressure (as shown in Figure 1.5(a).

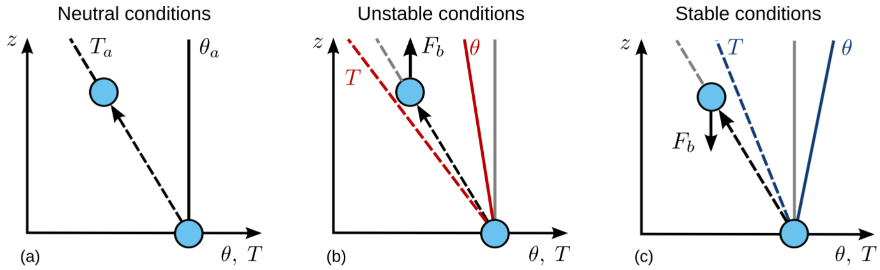

Figure 1.5: Vertical profiles of potential temperature (shown by solid lines) and temperature (shown by dashed lines) for the neutral, stable and unstable conditions. The motion of the air parcel is depicted by the circle which moves upwards. F_b depicts the buoyancy force direction. (The figure has been reproduced from Allaerts (2016) (Pg. 16))

The stable condition (see Figure 1.5(b)) arises when the background temperature decreases at a lesser rate than its adiabatic counterpart. The shifted air parcel is now cooler than its surroundings after moving upwards. It then experiences a downward buoyancy force. Lastly, in the unstable condition (see Figure 1.5(c)), the background temperature decreases with an increase in height at a greater rate than the adiabatic lapse rate. The air parcel is warmer than its surroundings after moving upwards, which pushes it further upwards due to the resultant buoyancy force.

The description of the three stability types can be further simplified by defining the potential temperature (θ). The potential temperature of an air parcel at a particular pressure P is the temperature attained by the parcel if brought to a standard reference pressure P_0 (usually 100kPa) in an adiabatic manner (Stull, 1988). Mathematically, it is given as: $\theta = T\left(\frac{P_0}{P}\right)^{R/C_p}$ where, C_p is the specific heat capacity at a constant pressure of air and R is the gas constant of dry air. The three stability cases can be defined as the variation of potential temperature with height. The neutrally stable case is when $\frac{d\theta}{dz} = 0$, the unstable case is when $\frac{d\theta}{dz} < 0$ and the stable case is when $\frac{d\theta}{dz} > 0$. For the remainder of this thesis, the term potential temperature has been referred to as *potential temperature* or *temperature*.

Moreover, it should be noted, that the thesis considers only dry air without accounting for its humidity content, as this is beyond the scope of the present work. After having introduced the three stability types, it is imperative to mention the conditions in which these are encountered in the atmosphere.

When latent heat release and radiation are absent, surface heating or cooling determines the stability condition within the ABL. The neutral condition results when there is no heat flux present at the surface of the earth. This is the simplest case of the ABL, which has been extensively studied using DNS by Coleman et al. (1990), Coleman (1999), Deusebio et al. (2014); LES by Mason and Thomson (1987), Andren et al. (1994), Momen and Bou-Zeid (2016) and RANS by Yan et al. (2016), Parente et al. (2011), Han and Stoellinger (2020). The neutral BL is also referred to as the Ekman BL, owing to the work of Ekman (1905) who studied the importance of the Coriolis effect on boundary layer flow in the ocean. In the following section, the Conventionally Neutral Boundary Layer, which is the focus of the present study, is further elaborated as they often occur under offshore conditions (Sood et al., 2020).

Further, Stable Boundary Layers are formed by the presence of negative heat flux at the surface. This cools the air near the surface, which gives rise to the stable condition. In this condition, air parcels of higher density are placed closer to the ground as compared to its low density counterparts that are placed higher up. This is a stable condition that tends to suppress vertical turbulent motions. As observed from Figure 1.4, the growth of the SBL begins after sunset due to which it is called nocturnal BL. SBL is much thinner as compared to their neutral and convective counterparts. Also, they have smaller and weaker turbulent eddies, which inhibit mixing (Allaerts, 2016).

On the other hand, a Convective Boundary Layer (CBL) (the unstable condition) is caused by the presence of a positive heat flux at the ground level. It can also arise due to radiative cooling or due to the presence of heat radiation and clouds. In all cases, air with higher density is placed above air with low density, which creates an instability. The instability creates convective circulations and high turbulent intensities. From Figure 1.4, it can be observed that CBL's occur during the daytime, when the surface is heated by the presence of the sun. CFD LES studies of the CBL have been performed by several authors such as Moeng and Sullivan (1994), Sullivan et al. (1994), Kim et al. (2003) as mentioned in Allaerts (2016).

1.3. The Conventionally Neutral Boundary Layer (CNBL)

The traditional stability types within the ABL are neutral, stable and unstable, based on the heat flux exchange at the surface of the earth. However, in the 1970s, the Brunt–Väisälä frequency appeared as a scaling parameter in the expression for the height of the ABL. Considering the assumptions of the Boussinesq approximation, the mathematical definition of the Brunt–Väisälä frequency (N) is given as:

$$N = \sqrt{\frac{g}{H_\rho}} = \sqrt{\frac{g}{\theta_0}\frac{\partial\theta}{\partial z}} \tag{1.1}$$

where in Equation 1.1, H_ρ is the density scale height and θ_0 is the reference potential temperature, g is the acceleration due to gravity. In the case of the Neutral Boundary Layers, the terms truly neutral and conventionally neutral were introduced for the flows developing against a neutral or stably stratified fluid (Zilitinkevich and Baklanov, 2002). As mentioned in the previous section, the occurrence of the NBL is common in the offshore conditions. However, based on the atmospheric data covering a period of more than 85 years, (Hess, 2004) found that the occurrence of a truly neutral BL is one which does not seem to exist in the atmosphere or it is so rare that it has not been well observed.

As reported by Allaerts (2016), the formation of CNBLs can be observed over large lakes or large water bodies that are semi enclosed due to the advection of the boundary layer air from land. The CNBL has been studied extensively by Csanady (1974) and Smedman et al. (1997). Further, the flow over an infinitely wide wind farm placed within a CNBL has been performed by Allaerts and Meyers (2014).

The structure of the CNBL has been shown in Figure 1.6. The neutral boundary layer is capped by an inversion layer above. Further above the capping inversion, is the non-turbulent free atmosphere, which has potential temperature variation ranging between 1K/km and 10K/km (Sorbjan, 1996). In the free atmosphere, the balance between the Coriolis force and the horizontal pressure gradient (also called the geostrophic balance) determines the resultant wind velocity G (Allaerts, 2016).

$$f_c G sin\alpha = \frac{1}{\rho_0}\frac{\partial p_\infty}{\partial x} \tag{1.2}$$

$$-f_c G cos\alpha = \frac{1}{\rho_0}\frac{\partial p_\infty}{\partial y} \tag{1.3}$$

where, α represents the angle between the geostrophic velocity vector and the x-axis, $f_c = 2\Omega sin(\phi)$ is the Coriolis parameter (where Ω represents the angular velocity of the earth's rotation about its own axis, ϕ represents the latitude). As can be observed from Figure 1.6, in the free atmosphere, the pressure gradient is normal to the direction of flow.

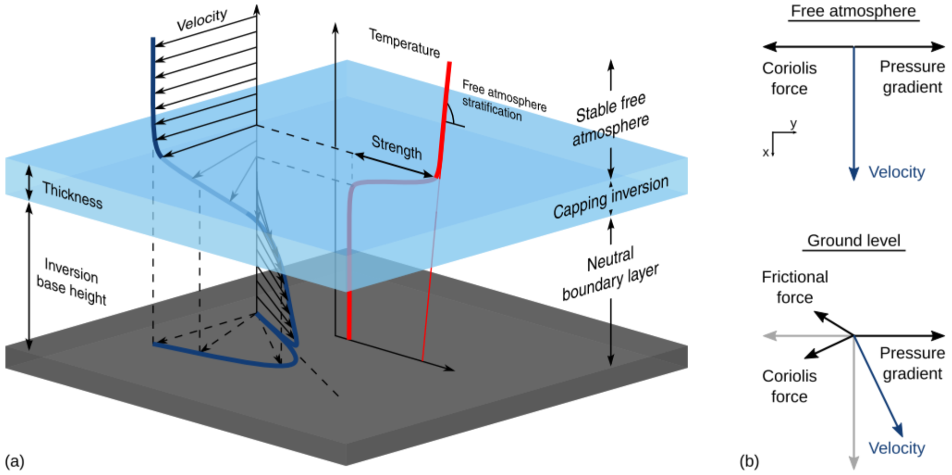

Figure 1.6: (a)The three layer structure of the atmosphere showing the variation of potential temperature and velocity with height in the three layers as shown in Allaerts and Meyers (2017), Allaerts (2016), Allaerts and Meyers (2015); (b) The horizontal force balance in the free atmosphere and at the ground level (The figure has been reproduced from Allaerts (2016))

As one moves, closer to the ground, i.e. within the neutral BL, the magnitude of the flow velocity is reduced due to the friction with the ground. This causes the Coriolis force to be reduced, thereby rotating the resulting wind vector towards the pressure gradient. Further, the capping inversion is a thin layer interfacing the turbulent neutral boundary layer (below) with the free atmosphere above. The potential temperature within the capping inversion sees a steep change with height. The capping inversion has a dominant impact on the flow behaviour within the boundary layer. It controls the height of the boundary layer, by limiting the penetration of turbulent gusts into the free atmosphere. Also, most of the direction change of the wind velocity vector occurs within the inversion layer. The importance of the capping inversion will be discussed later in the following section.

1.4. The Capping Inversion

While the location of the Capping Inversion has been described in the previous section, it is important to understand its topology and numerical implementation within the present thesis. Further, it is necessary to shed light upon the impact of each of these parameters on the flow physics within the BL.

The boundary layer flow is affected by two major parameters of the capping inversion. They are the height of the base of the capping inversion and the inversion strength. The effect of the capping inversion is negligible when it is located above the equilibrium height of the theoretical truly neutral case. This was translated by Arya (1975), Arya (1978) and Allaerts (2016) into a similarity parameter h_* defined mathematically as:

$$h_* = \frac{|f_c|h}{u_*} \tag{1.4}$$

This relates ABL height with the Rossby-Montgomery scale $(u_*/|f_c|)$ (where u_* is the friction velocity). Further, Hess (2004), studied the impact of the presence of the capping inversion on the structure of the neutral, barotropic Planetary Boundary Layer(PBL) by comparing predictions by various CFD models and field observations. They reported that for values of $h_* > 0.15$ the impact of the CI is on the structure of the planetary boundary layer becomes insignificant in terms of entrainment and mixing.

Further, Csanady (1974) found an asymptotic depth beyond which no further entrainment takes place. This depth was dependent upon the strength of the capping inversion. This was confirmed by Tjernström and Smedman (1993) through a measurement campaign carried out over the Baltic Sea. Lastly, Tennekes (1973) found that the gradient of potential temperature at heights above ABL has no impact when the inversion strength or height is high.

The variation of potential temperature across the inversion layer is represented through two models. The first is a zeroth order jump model (see Lilly (1968), Tennekes (1973), Sachsperger et al. (2015)), where the inversion layer is shown by a sharp temperature jump at a particular height. In this model, the thickness of the capping inversion is not considered. Further, a first order model (see Betts (1974),van-Zanten et al. (1999)), assumes a finite inversion thickness while assuming a finite temperature variation across the inversion thickness. While, both of these representations are non-physical and their comparison with field observations or numerical simulations yields unsatisfactory results when used to estimate the height of the boundary layer, the first order jump model is chosen to represent the initial temperature jump across the capping inversion in the present study. This is because it is easy to define the capping inversion (in terms of its base height, thickness and temperature jump using the first order model).

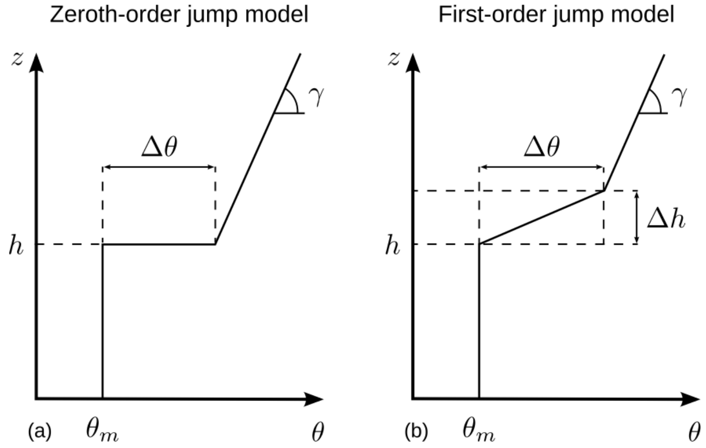

Figure 1.7: The vertical profile of the Capping Inversion as shown by (a) The zeroth order jump model (b) The first order jump model (The figure has been reproduced from Allaerts (2016))

The impact of the capping inversion with regard to wind farm performance was studied by Allaerts and Meyers (2015). The study reported a lower power output for an increased capping inversion strength, and also an increase in the power output of the farm upon increasing base height of capping inversion. The boundary layer growth is limited by the capping inversion and that the entrainment rate is heavily dependent upon the capping inversion strength as mentioned in (Allaerts and Meyers, 2014).

After having defined the relevant atmospheric factors, it is imperative to understand their impact upon the flow in and around wind farms. With regard to the same, the following sections introduce the topic of wind farm wakes, the effect of stability on the wind farm wakes, the impact of the wind farms on the ABL and lastly introduces the topic of the present research AGW excitation by wind farms.

1.5. Wind Farm Wakes

The turbines placed in a wind farm extract energy from the incoming wind. The energy extraction leads to the formation of a region of reduced wind speed and increased turbulence behind each turbine. This region is referred to as the wind turbine wake or the turbine wake region. The momentum deficit in the wake region is recovered downstream through transfer of energy through turbulence from the free stream to the wake region. The exact distance at which the complete recovery of turbine wakes varies, as reported by multiple studies. While Ammara et al. (2002) assumed the turbine wake recovery to be extended to 10D, Mehta et al. (2014) measured increased turbulence intensity at 15D. Recent experimental studies by Chamorro and Porté-Agel (2010) and numerical studies by Wu and Porté-Agel (2011) found wake effects to be prevalent until 20D downstream. Further, Vermeer et al. (2003) segregated the wake region into the near wake region extending between up to lengths of 2D-4D down stream of the turbine and a region of far wake further downstream. While the near wake is strongly influenced by the geometry of the turbine blade (as reported by Crespo et al. (1999)), the far wake is influenced by the incoming flow conditions, the power and thrust coefficients of the turbine.

The main aspects of the near-wake flow region such as the shedding of the root and tip vortices has been extensively studied both experimentally by Whale et al. (2000), Grant and Parkin (2000), Zhang et al. (2012), Zhang et al. (2013), Lignarolo et al. (2016), Wei et al. (2017) and numerically by Ivanell et al. (2010a), Lu and Porté-Agel (2011), Ivanell et al. (2010b), Mirocha et al. (2015), Sarmast et al. (2016), Tabib et al. (2017). Further, the flow characteristics in the far wake region has been studied through field measurements (Banta et al., 2015, Barthelmie et al., 2004, Bingöl et al., 2010, Marathe et al., 2016, Smalikho et al., 2013), lab experiments (Bastankhah and Porté-Agel, 2014, 2017, Chamorro and Porté-Agel, 2009, Medici and Alfredsson, 2006, Singh et al., 2014) and numerical simulations (Lee et al., 2013, Porté-Agel et al., 2020, Wu and Porté-Agel, 2011, 2013).

While the turbines placed upstream extract energy from the incoming flow, their wakes cause a lower availability of incoming wind power at the downstream turbines in large wind farms. Further, the size, spread of the wake region, its recovery rate depend on the mean wind speed and direction. These are dependent on atmospheric factors such as the thermal stability that further determines the turbulence intensity (Hansen et al., 2012).

1.6. Impact of wind farms on ABL

The presence of wind farms has an impact on local meteorology, and this has been studied through numerical weather prediction models and field observations. Keith et al. (2004) used climate model simulations to study the impact of the large-scale use of wind power upon the local and global climates through the extraction of kinetic energy and altering the turbulent transport within the ABL. The study reported that very large amounts of wind power extraction can cause a non-negligible climate change at continental scales.

Further, the velocity deficit regions are found to extend for considerable distances, downstream of the wind farm. Christiansen and Hasager (2005) studied satellite images and found that the wakes of the Horns Rev I and Nysted offshore wind farms extended up to downstream distances of $20\,km$. Using the Weather Research and Forecasting model, Fitch et al. (2012) found similar velocity deficits downstream of an idealized wind farm. Due to the presence of velocity deficits over large downstream distances, the presence of one wind farm can result in reduced efficiency at neighbouring wind farms located downstream. This was confirmed by power measurements of the Nysted wind farm before and after installation of the Rødsand II Wind Farm (which was located upstream of the Nysted) carried out by Nygaard (2014). The study reported lower wind power generation (therefore lower efficiency) at the Nysted farm once the Rødsand II Wind Farm became operational.

Thus, offshore wind farms have a significant impact on the ABL. In recent times, with an increase in the number of offshore wind farms, (Allaerts and Meyers, 2017, 2018, Wu and Porté-Agel, 2017) suggested that these can excite Atmospheric Gravity Waves (AGWs). These AGWs alter the flow ahead of the farm and within it, thereby causing power fluctuations at the level of individual turbines. While the physics of AGWs has been extensively studied independently as mountain lee waves since the 1940s, AGWs excited by wind farms and the impact they have on wind power generation is a new-found topic of research.

1.7. Atmospheric Gravity Waves

AGWs are oscillations in buoyancy in a stably stratified fluid, where gravity plays the role of a restoring force (Rauber and Ramamurthy, 2015). They originate from various sources, of which the most notable ones include topography, convection, and wind shear. Further, the less notable ones include flow adjustment in unbalanced flows in the vicinity of frontal systems and jet streams, body forcing that accompanies localized wave dissipation and interaction among waves (Fritts and Alexander, 2003). Further, AGWs have a unique ability to transport and distribute energy in a more rapid manner as compared to the mean flow (Nappo, 2002, Rauber and Ramamurthy, 2015). Early works on AGWs were carried out by Queney (1948), Scorer (1949) and Gossard and Munk (1954). Among these works, Queney (1948), Scorer (1949), studied AGWs as lee waves caused by the airflow over mountains. Among the notable works which have studied AGWs as two-dimensional responses to two-dimensional topography are Long (1955), Durran and Klemp (1987) and Lott (1998). Further, AGWs were also studied as responses to three-dimensional topographic perturbation using measurement programs (Nastrom and Fritts, 1992) and numerical studies, which yielded estimates of mountain wave amplitudes, scales and momentum fluxes (Fritts and Alexander, 2003). The effect of AGWs on the wind velocity, turbulence fluctuations within the lowest part of the atmosphere (called the Atmospheric Boundary Layer(ABL)) was studied by Zaitseva et al. (2018), Jia et al. (2019). The most significant impact of AGWs upon the atmosphere is the transport of mean-flow horizontal momentum (wave stress) in the vertical direction, and this in turn affects the general circulation and the stable ABL. In the case of a stable ABL, the wave stress may be as high as the friction stress on the ground (Nappo, 2012). The major source of wave stress is orography (the presence of hills, mountains). Mountain waves strongly affect the momentum balance (Nappo, 2012). Akin to mountains, very large wind farms act as partially permeable mountains which redirect the flow upwards, which generates gravity waves (Allaerts and Meyers, 2017). These further induce considerable changes in the regional pressure field in and around the farm that further causes velocity fluctuations over the entire wind farm (Smith, 2009).

The present work sheds light on the effect of self-induced AGWs on an offshore wind farm. Further, the impact of the thermal stratification in the free atmosphere and the capping inversion on the characteristics of the excited AGWs and the effect that these AGWs have on the power output of the farm is studied. Also, the impact of the base height of the capping inversion on the excited AGW characteristics and power output is investigated. The exact values of thermal stratifications in the free atmosphere, the capping inversion and the height of the capping inversions considered are introduced in the next chapter.

1.8. Summary

The current chapter presents a brief history of wind turbine technology. Further, it introduces the various losses observed in wind farms. It also gives an extensive introduction to the concepts of boundary layer meteorology that are relevant to the present thesis topic. Furthermore, it sheds light upon the impact of the various atmospheric parameters on the wind farm performance. Lastly, the chapter introduces the topic of the present thesis, which is studying the impact of self-induced AGWs on an offshore wind farm.

The following chapter presents a detailed review of literature involving the impact of mesoscale phenomena such as the Coriolis force upon the air flow in and around wind farms, and also the excitation of AGWs by offshore wind farms. Furthermore, the identified research question and its novelty is presented. Lastly, the chapter also presents a list of simulations that would present the answer to the posed research question.

2

Literature Review and Analysis

The present chapter sheds light on the important atmospheric factors (such as thermal stability, the Coriolis force) that affect the flow in and around large wind farms. Further, it introduces the relevant literature pertaining to AGW wind farm interactions, while also citing literature that is focused on blockage (deceleration of flow ahead of a wind farm). The first section and its respective sub-sections cite recent, relevant research articles and discusses the main findings in each work. The next section discusses the limitations in the current body of knowledge and how the present work would fill the gaps therein.

2.1. Relevant Literature and their respective findings

The present section cites relevant literature and lists the important findings. The cited works are further categorized into sub-sections based on the respective topics investigated.

2.1.1. Impact of Atmospheric Stability on Wind Farms

The concept of *thermal stability* or *atmospheric stability* was introduced in section 1.2. In relation to wind farms, it affects the mechanical turbulence in the wake region, and also determines the ambient turbulent intensity (Allaerts, 2016). Further, Hansen et al. (2012) had proved atmospheric stability and turbulence intensity were correlated. They reported that as the atmosphere becomes more unstable, the turbulence intensity increases. It also reported a notable quasi-linear relationship between the turbulence intensity and maximum power deficit, where the slope is highly dependent upon the wind turbine spacing. Further, a power down the line analysis showed that the maximum deficit was between the first two turbine rows, while no considerable drop in power generation was observed for further consecutive rows of turbines placed further downstream.

Furthermore, Abkar and Porté-Agel (2013) used LES to study the influence of stratification in the free atmosphere on the ABL flow inside and above a large wind farm and the effect it has on power extraction by the turbines within the farm. The study considers two Free Atmosphere Lapse Rates (FALR) ($\Gamma = 1K/km$ and $\Gamma = 10K/km$), two aerodynamic surface roughness lengths viz. $0.1\,m$ and $0.01\,m$, two turbine layouts - staggered and aligned and two turbine spacing values. It reported that, for very large wind farms, vertical entrainment of kinetic energy from the external atmosphere is the only source of kinetic energy, which increases the height of the boundary layer. The results reported a shunted BL growth for a higher lapse rate ($\Gamma = 10K/km$) in the free atmosphere. This further lowered the entrainment of the kinetic energy from the free atmosphere to the surface layer, which then caused a 35% reduction in the power output.

Also, Abkar and Porté-Agel (2014) used 3D LES to study the flow in and around an infinite wind farm having a staggered turbine layout operating under two FALR values $\Gamma = 1K/km$ and $\Gamma = 10K/km$. An energy budget analysis was carried out to understand the effect of various physical processes that affect the energy balance while varying the FALR and inter-turbine spacing. The study reported that a stronger free atmosphere stratification would reduce the entrainment of energy from there, leading to lower BL height. Further, an increase in the farm density led to an increase in the height of the BL. Further analysis of the mean kinetic energy budget within the ABL showed an increase in the work performed by the pressure gradient upon the BL, which balanced the energy extraction by the turbines. The results showed that the entrainment of kinetic energy from the mean flow in the free atmosphere increased with an increase in the density of turbines within the wind farm and a decrease in the static stability of the free atmosphere. Furthermore, the study reports an increase in the shear production and dissipation with an increase in density of the wind farm and a decrease in the stratification of the free atmosphere.

Further, Abkar and Porté-Agel (2015) observed that the atmospheric stability has a tremendous impact upon the spatial variation of mean velocity deficit, wake meandering characteristics and turbulence statistics in the near wake region. The wake growth is higher in the convective (unstable) case vis-à-vis its stable counterpart. Also, the wake growth and wake meandering was found to be higher in the convective case as opposed to its stable and neutral counterparts. A higher turbulence intensity in the incoming wind in the convective or unstable condition led to a higher turbulence entrainment flux into the wake, which further led to a higher amount of wake recovery in the unstable case. With regard to production, dissipation, transport of turbulence, it was found that the turbulence dissipation and production reach a maximum near the upper edge of the wake. This was due to high turbulent fluxes and wind shear present in this region. The turbulence production decreased downwind of the turbine with an increase in the amount of atmospheric stratification.

Allaerts and Meyers (2015) carried out LES to study the flow over an infinite array of wind turbines operating in a Conventionally Neutral Boundary Layer (CNBL). A simplified model of the atmosphere was used in the study consisting of three layers viz. (i) the surface layer; (ii) the Capping Inversion (CI); (iii) the free atmosphere (refer Figure 1.6 for details)

Further, the study defined the Capping Inversion Strength (CIS) as the potential temperature difference between its bottom and top layers [1]. Three values of the same viz. $0K, 2.5K$ and $10K$ were considered. The study reported that varying the capping inversion characteristics (base height and strength) led to a change in the power extracted by the turbines. The study considered CI base heights of $200m, 500m, 1000m$ and $1500m$. With an increasing inversion strength or height, a decrease in the BL growth rate was observed. However, in the absence of a capping inversion layer, there was a three-fold increase in the growth rate of the BL as compared to the baseline case. The results also showed that an increase in the strength of the inversion layer from $2.5\ K$ to $10\ K$ caused a decrease of $13 \pm 0.2\%$ in the power output of the wind farm. Also, the height of the base of the inversion layer has a significant impact upon the power output, which showed an increase of $31 \pm 0.4\%$ with increase in the inversion base height from $500\ m$ to $1500\ m$.

2.1.2. Impact of Coriolis Force on Wind Farms

Paul van der Laan et al. (2015) used CFD - RANS to simulate the interactions between two wind farms. A simplified version of the $k - \epsilon$ model is used to model the ABL. The study quantifies the impact of Coriolis force on wake interactions between two wind farms. The study reported that while considering a single wind turbine wake, the Coriolis force had minimal effect on the wind farm. However, they observed a large impact of the same while considering an entire wind farm (in the present case, the Rødsand 2 wind farm that operated in the wake of the Nysted wind farm). The wakes of the turbines placed in the wind farm upwind (Nysted) deflected towards the right (due to the Coriolis force), which caused it to align with the curved layout of the downstream (Rødsand 2) wind farm. The study recommended that since the effect of the Coriolis force is found to be significant in the RANS simulations, the same should be considered in future studies involving perusal of wind farm wake interaction.

Further, Paul van der Laan and Sørensen (2016) investigated the impact of Coriolis force upon the wake of a wind farm located in the Northern Hemisphere. To study the same, two different representations

---

[1] This is also the definition used in the present study

of a wind farm were used, viz. (i) A region of high roughness; (ii) A 5×5 actuator disc array. For the model using the roughness change, the wake of the wind farm turned in the counter-clockwise direction due to the Coriolis force imbalance. Further, for the actuator disc array representation, the wind farm wake deflected in the clockwise direction. However, using a single turbine model, it was found that the deflection was caused due to the wind veer present on-site and not due to the Coriolis force itself.

Also, Howland et al. (2020) used LES to study the Coriolis effects observed within and trailing a large finite wind farm. The study found that the ABL had a significant dependence upon the direction of the geostrophic wind. This comes out as a result of the horizontal component of the earth's rotation. Due to the horizontal component of the Earth's rotation, the mean velocity, veer profiles and Reynolds shear stress profiles would be a function of the geostrophic wind direction within a CNBL. As the Reynolds stresses were being redistributed as a function of direction of the geostrophic wind, the momentum balance within the BL was found to be altered.

2.1.3. Impact of Self Induced AGWs on wind farms

AGWs have been studied as mountain lee waves since the 1940s. However, the possibility of AGWs triggered by very large wind farms was first investigated by Smith (2009), who developed a linear quasi-analytical model of the response of the atmosphere to the drag force induced by the turbines in a very large wind farm. The study observed that the change in potential temperature played a crucial role in controlling reduction of the wind speed over the farm. The conservation of mass (continuity relation) leads to an upward displacement of the top of the boundary layer to accommodate horizontal convergence. In the process of pushing up the stratified layer of air, air parcels of different temperatures get displaced and this causes temperature anomalies. These further create adverse pressure gradients that decelerates the incoming flow upstream of the farm. A favourable pressure gradient is created above the farm which increases the flow velocity in the farm, which prevents additional deceleration of the flow due to the turbine drag. This results in a nearly uniform overall wind speed over the entire wind farm. The vertical displacement of the BL also generates trapped gravity waves in the inversion layer above and also gravity waves that propagate in the vertical direction in the free atmosphere. The results show that, in the sub-critical case [2], the gravity waves in the inversion layer can propagate upstream, thereby changing the pressure field there. Furthermore, the upstream propagation of the waves on the inversion creates an adverse pressure gradient, which decelerates the incoming air flow, resulting in a reduced flow velocity at the first turbine row. In the super-critical case, these gravity waves are unable to move upstream. The signal seen upstream is due to the gravity waves propagating in the vertical direction. Further, close to critical conditions($Fr = 1$), a strong reduction in wind velocity over the entire farm was observed. However, a flow acceleration was observed on the sides of the wind farm. The study showed that AGWs cause fluctuations in the incoming flow velocity over the entire wind farm. However, the study assumes the linear theory to be valid. Thus, any change in the turbine drag, density or the BL height results in a proportional change in the wind speed and pressure perturbation.

Further, Lu and Porté-Agel (2011) conducted 3D CFD-LES using the GEWEX Atmospheric Boundary Layer Studies (GABLS) case to study the wind turbine wake characteristics in a wind farm of infinite span-wise length operating in a stable ABL. Akin to AGWs perturbed by the presence of mountains, they found that when a wind turbine is placed in a SBL, buoyancy waves are induced. Further, the study observed that the kinetic energy extraction is dependent on turbine spacing, i.e. a smaller turbine spacing resulted in a higher extraction of kinetic energy from the mean flow. It reported a buoyancy frequency of about 0.01 Hz within the range of the wind turbine height, with a dominance of the first mode in the large scale fluctuations and its resonant modes. This led to a fluctuation in the energy output at each turbine present within the farm. Further, the SBL gave rise to asymmetric disc loading due to high wind shears. There

---

[2] The Froude number (Fr) is used to categorize the flow of air as sub-critical ($Fr < 1$), super-critical ($Fr > 1$) and critical ($Fr = 1$). The Froude number is the ratio of the wind speed to wave speed on the inversion.

Mathematically, it is given as: $Fr = \frac{U}{\sqrt{g'H}}$ where U is the velocity of flow above the BL, H is the BL height and $g' = g(\Delta\theta/\theta)$, that accounts for the gravity (g) and CIS ($\Delta\theta$) i.e. the change in potential temperature across the capping inversion were shear forces observed in the vertical and horizontal direction. The vertical shear force was due to the change in wind speed with height, while its horizontal counterpart is due to the change in the wind direction caused by the inclusion of the Coriolis force. These shear forces drive the turbulent energy away from the wind turbine centre.

Wu and Porté-Agel (2017) used LES to study the flow around a wind farm of finite stream-wise length placed in a CNBL for two lapse rates within the free atmosphere, viz. $\Gamma = 1K/km,\ 5K/km$. The study reported that for $\Gamma = 1K/km$, the wind flow within and around the wind farm never reach the fully developed regime. However, in the case of $\Gamma = 5K/km$, a vertical deflection of the airflow at the exit and inlet, triggered standing AGWs. The triggered AGWs cause a flow deceleration at the inlet and acceleration at the exit. At the inlet, for an FALR of $\Gamma = 5K/km$, a 35% deficit in the turbine power output was observed as compared to the weakly stratified case. At $\Gamma = 1K/km$, for a super-critical flow ($Fr > 1$), the gravity waves did not have any upstream effects and thus the blockage seen in this case was primarily caused by the presence of downstream turbines.

Allaerts and Meyers (2017) studied the effect of self-induced AGWs upon an offshore wind farm operating within a CNBL using LES. The atmosphere is represented as three layers viz. the neutral surface layer, the capping inversion and the free atmosphere aloft at prescribed altitudes as shown in Figure 1.6. The incoming BL heights were varied ($300\,m$, $500\,m$ and $1000\,m$). These were generated in a separate precursor LES. At an incoming BL height of $300\,m$, the inversion layer was displaced vertically as the BL developed. This further led to an AGW excitation in the free atmosphere and the inversion layer, which further caused a pressure perturbation on the BL. Overall, the AGWs were found to redistribute the kinetic energy of the mean flow throughout the farm, and this effect was the highest in the case of low heights of the incoming BL.

Allaerts et al. (2018) used a fast wind farm BL model combined with ERA reanalysis data to study the effect of gravity waves induced by the wind farm upon the annual energy yield of a Belgian Dutch wind farm located offshore. The atmosphere is modelled as a set of three consecutive layers: a surface layer (where the wind turbines are placed), a second layer that extends till the top of the capping inversion and the third layer that depicts the free atmosphere. The study reported an estimated annual energy loss of $4 - 6\%$ caused by the presence of self-induced gravity waves. However, in some cases, the study reported a negative velocity reduction, which is indicative of an acceleration in front of the farm. As a consequence of the wind acceleration ahead of the farm, the power generation increases. It should be noted that the representation of the entire atmosphere as a three layer model does not hold well in all cases, as there are possibilities of existence of multiple inversion layers and also that of a heterogeneous stratification of the free atmosphere.

Allaerts and Meyers (2018) studied the impact of self-induced gravity waves and the efficiency of a wind farm operating under the transition from neutral to stable conditions using the LES code SP Wind. The results obtained throw light upon the effect of stable stratification upon the performance of large wind farms. The wind farm gravity waves induce an adverse pressure gradient, which decelerates the flow upstream of the farm. This reduces the power generated by the first row of wind turbines as compared to a wind turbine operating in isolation. Further, the wake recovery was delayed in the wind farm under stable conditions, due to lack of turbulent mixing. Also, it was found that the wind farms only extract energy from a very shallow part of the BL. AGW's were excited in all the cases simulated, and the amplitudes showed an increasing behaviour with time and also with the stability of the surface layer (simulated by the higher surface heat flux). The intensity of the gravity waves was found to be dependent upon multiple factors such as the rising wind farm drag, Froude number fluctuations and the dispersion caused by vertically propagating gravity waves. However, the study considers an infinitely wide wind farm.

Allaerts and Meyers (2019) performed a sensitivity analysis using a fast BL model in a 2D mode with data from previous LES runs over an infinitely wide wind farm. The sensitivity of the wind farm induced gravity waves to the layout of the wind farm and the atmospheric state is investigated while also considering three-dimensional effects. The work reported that gravity wave excitation is the highest when the critical $Fr = 1$. However, the effect upon the energy extraction was observed to be maximum when the Froude number is slightly less than unity. This is attributed to the trade-off that occurs between the amplitude and upstream impact of gravity waves. The presence of surface friction and internal gravity waves dissipates the perturbation energy.

It was also observed that the impact of gravity waves was minimal for very wide or long wind farm arrays. The impact is maximum at the aspect ratio of about 1.5 [3]. Further, it was also found that the AGW induced power losses increases with turbine height and farm size. Among the factors affecting the AGW activity, the most crucial ones are the free atmosphere stratification, the convexity of the wind profile and the difference in direction between the wind within the BL and the geostrophic wind. For the present study, the wind speed and the Brunt–Väisälä frequency [4] is considered to have a constant value in the free atmosphere. However, under realistic conditions, this would not be the case.

2.1.4. AGWs caused by topography ahead of wind turbine/farm

Yang et al. (2015) used LES to study the effect of having an upstream 3D hill of finite span-wise length upon the wake recovery of a wind turbine placed downstream. Three different hill heights are considered - $h_{hill} = z_h - 0.5D$, $h_{hill} = z_h$ and $h_{hill} = z_h + 0.5D$, where D is the diameter of the turbine, h_{hill} is the height of the hill and z_h is the hub height of the turbine. The study reported that for the case ($h_{hill} = z_h - 0.5D$), when the turbine is placed at 6D and 8D downstream of the hill, the impact of the upwind hill on the wake of the turbine is minimal (in terms of TKE and time averaged downwind velocity). In the cases $h_{hill} = z_h$ and $h_{hill} = z_h + 0.5D$, the turbine wake recovers faster than that over a flat terrain. However, the study only considers a single wind turbine and not a large wind farm.

Ollier et al. (2018) studied the effect of upstream gravity waves upon a given wind farm layout using Ansys Wind modeller with a k-ϵ turbulence model. The effects of the Coriolis force were not considered. The study modelled a hill of infinite span-wise length upstream of a wind farm array (having a finite span-wise and stream-wise length). Standing AGWs of $4.9\ km$ wavelength were created, which oscillated through the wind farm. There is significant variation of velocities at the disc plane of each of the turbines based on the position of the same relative to the position and shape of the gravity waves. While all the turbines are incident with wind speeds above the cut in wind speed, a 76% lower power output was observed at the far eastern edge and a 29% variation in power output was observed in the control case.

Draxl et al. (2020) observed AGWs occurring in a stably stratified atmosphere in the lee of the Cascade mountains using Geostationary Operational Environmental Satellite (GOES) data and numerical simulations. The study reported a variation of 11% power output caused by mountain waves. In the presence of waves of shorter wavelengths, a portion of the wind farm experienced lower wind velocities, while the other is exposed to higher wind velocities. The increased wind speeds in portions of the farm compensated for the reduced counterparts in the other portions, and the effects of the gravity waves upon the wind farms become minimal. In the period of occurrence of gravity waves with longer wavelengths, entire wind farms can experience a lull or excess in wind speeds. The study points out that there is a need to understand the effect of simultaneous high and low wavelength gravity waves upon wind farm outputs.

2.1.5. Blockage

In the present study, the term blockage will be mentioned several times. Therefore, it is imperative to define blockage (in the context of the present study).

The term blockage has been used in multiple studies to define the deceleration ahead of the incoming wind upstream of the farm. However, a comprehensive definition of blockage is missing from all the works perused. A qualitative definition of blockage is given by (Bleeg et al., 2018). The study differentiates the induction of an individual turbine and the blockage due to the farm itself. The presence of

---

[3] The aspect ratio is the ratio of span-wise to stream-wise length

[4] The Brunt–Väisälä frequency is that frequency at which a parcel of air when disturbed in the vertical direction would oscillate in a statically stable environment (Vallis, 2017)

the farm blockage is identified through measurements upstream of three unnamed wind farms before and after their commissioning. Further, the study also includes RANS simulations which point to ”wind-farm-scale” blockage. This manifests reduced wind speeds just upstream of each farm. At distances of 2D upstream, the relative slowdown is 3.4%. Furthermore, the average slowdown is 1.9% at 7D-10D upstream. However, the study lacks a mathematically quantified definition of ’wind-farm-scale’ blockage.

Another study, by Branlard et al. (2020), defines blockage as the reduction of upstream wind speed due to the energy extraction by the turbine. The effect is referred to as ”wind farm blockage” and the affected area is referred to as the induction zone. These are used interchangeably throughout the work. Further, the study does not consider the large scale array effects and the two-way interaction of the wind farm with the ABL.

Also, Segalini and Dahlberg (2020) conducted an experimental study to quantify wind farm blockage. The study aims to quantify the velocity decrease at the first row of wind turbines due to the presence of other turbines downstream (the rest of the farm). Several staggered layouts have been studied. An empirical correlation formula has been derived to relate turbine spacing, number of rows and velocity decrease. However, since this is an experimental study, scaled versions of the turbine are used. Also, the incoming wind profile does not have the characteristics of a fully developed ABL.

From the works mentioned above, it is understood that the wind farm blockage, can be qualitatively described as the reduction in wind velocity ahead of the first turbine row due to the presence of the rest of the farm placed behind and next to the same. In the present study, AGW induced blockage is caused by the adverse pressure gradient upstream of the farm. It is quantified by the relative drop of the incoming wind velocity ahead of the first turbine row at a given upstream distance ($\approx 10D$). Thus, if the value of velocity magnitude is lower ahead of the farm at a given upstream distance, it is deemed to represent a case of higher blockage and vice-versa.

2.2. Discussion

Early studies of wind turbine wakes had accounted for the impact of the atmospheric stability on them (Högström et al., 1988, Magnusson and Smedman, 1994). However, a detailed analysis of the impact of stability on wake characteristics, such as wake spread, meandering was carried out using CFD by Churchfield et al. (2012), Keck et al. (2014), Mirocha et al. (2015) and Abkar and Porté-Agel (2015); using wind tunnel studies by Chamorro and Porté-Agel (2010), Zhang et al. (2013) and using experimental observations by Subramanian et al. (2018). They commonly concluded that the wind turbine wake recovery is faster in unstable conditions as compared to stable or neutral conditions. These results were commonly reported for the Lilligrund and Horns Rev farms by Barthelmie et al. (2010) and, Hansen et al. (2012) respectively.

Further, the impact of the atmospheric stability within the free atmosphere upon the flow in and around an infinite wind farm was studied by Abkar and Porté-Agel (2013), Abkar and Porté-Agel (2014). Also, Allaerts and Meyers (2015) shed light upon the impact of the stability within the capping inversion and its base height on the wind farm operating within a CNBL. However, all of them consider a farm having an infinite length in the stream-wise and span-wise directions.

Further, Paul van der Laan et al. (2015) used RANS and reported $10 - 15\%$ losses in Rødsand II while operating in the lee of the Nysted farm. While Dörenkämper et al. (2015) predicted a deflection towards the pressure gradient related to the reduced wind speed, other studies, such as Fitch et al. (2012),Paul van der Laan et al. (2015) found a deflection towards the Coriolis force due to increased turbulent mixing. Further, Volker et al. (2015) showed the opposite direction of wake turning, depending upon the wind farm wake parameterization used in WRF.

Furthermore, Paul van der Laan and Sørensen (2016) used RANS to investigate the interaction between the Coriolis force and the wind farm wake. The study reported opposite wake deflection in two simulations based on varying wind farm representations. Also, (Gadde and Stevens, 2019) used LES to simulate the flow over 30 turbines represented as actuator disks in a CNBL and SBL. The study reported that the flow at wind turbine hub height deflects counter-clockwise at the entrance of the farm and clockwise at a further downstream distance. Thus, there is no consensus in literature on the direction in which the wind farm wakes turn due to the Coriolis effect.

Further, the impact of self-induced AGWs on wind farms have been studied by Lu and Porté-Agel (2011), Allaerts and Meyers (2017), Allaerts and Meyers (2018), Allaerts and Meyers (2019). However, all of them consider a wind farm of infinite span-wise and a finite stream-wise length. Since these studies consider farms having a finite stream-wise length, they observe AGWs excited by the wind farm as compared to studies with infinite stream and span-wise lengths mentioned above. Also, since the studies consider an infinitely wide (infinite span-wise length) wind farm, the stream wise flow deceleration is entirely converted to an upward flow deflection. This may lead to over-prediction of the AGW excitation as it does not account for a flow around the farm in the span-wise direction. Thus, a study involving flow simulation around a large wind farm of finite span-wise length remains imperative.

While (Yang et al., 2015) studied the flow over a hill of finite stream-wise and span-wise lengths placed ahead of a wind turbine, the study does not mention the occurrence of impact of AGWs generated by the hill. Further, (Ollier et al., 2018) studied the impact of the AGWs generated by a two-dimensional ridge on a wind farm of finite span-wise length placed downstream. Also, (Draxl et al., 2020) studied the impact of gravity waves occurring in the wake of the Cascade mountains on the wind farm placed there using the GOES satellite data. The study reports the presence of gravity waves generated by the presence of the hill upstream of the farm. However, none of these investigate the impact of self-induced gravity waves upon offshore wind farms of finite span-wise length. Some of the atmospheric conditions that were found to affect the spatial and temporal behaviour of gravity waves are studied by the literature mentioned above are - (i)The atmospheric stability in the surface layer, the inversion layer and the free atmosphere; (ii) The strength of the capping inversion layer; (iii) The height of the inversion layer

In the present study, the impact of these parameters upon the characteristics of the AGWs excited by a moderately sized offshore wind farm operating in a CNBL is studied. To the best of the author's knowledge, no simulations have been carried out to study the effect of self-induced gravity waves considering an offshore wind farm of finite span-wise length. This would be the novelty of the present research work.

2.3. The Research Question

The research question that then needs answering is:

"How does the thermal lapse rates in the capping inversion and free atmosphere affect the generation and propagation of self-induced gravity waves generated by an offshore wind farm of finite span-wise length?"

Further, in order to answer the research question, and understand the impact of each atmospheric parameter on the excitation and propagation of self-induced AGWs, the following parameters are varied one at a time :

- The Capping Inversion Strength (CIS) - Two values of the same are considered $2.5K$ and $10K$. These are common values for offshore conditions as mentioned in (Allaerts and Meyers, 2017, Sorbjan, 1996)
- The Free Atmosphere Lapse Rate (FALR) - $1K/km$ and $10K/km$ are considered based on their common occurrence under offshore conditions as mentioned in (Abkar and Porté-Agel, 2014, Sorbjan, 1996)
- The Capping Inversion Height (CIH) - $500\ m$ and $1000\ m$ are considered as in the work by (Allaerts and Meyers, 2015, 2017)

The choice of these values for each of the parameters is justified by the fact that they commonly occur under offshore conditions. This is as observed in the literature mentioned beside each parameter.

2.4. Summary

The present chapter sheds light on the current literature that study the flow in and around large wind farms. Further, the contributing factors to the excitation of AGWs are identified. Furthermore, two values of each parameter are chosen for a comparative study. Lastly, the exact research question that would be answered by the present thesis is identified and the novelty of the present research work is stated.

3

Simulation Methodology

In the present chapter, the reason for choosing RANS to investigate the present problem is stated along with the governing equations solved in the CFD solution methodology. Also, the chapter sheds light upon the Rayleigh damping layers used to damp out spurious AGW reflections and the Actuator disk model used to represent wind turbines in the present study.

3.1. Why RANS/URANS?

Since the present study performs flow simulations in and around an entire wind farm, the flow domain is $O(1000km^3)$. The Reynolds number (Re) of such flows is very large ($Re \approx O(10^7)$). Thus, a complete resolution of all turbulent length and time scales (including the dissipative scales $O(10^{-3})$) using Direct Numerical Simulations (DNS) would prove to be computationally expensive and impossible to achieve with the currently available state-of-the-art HPC resources.

The next available high fidelity tool in CFD is LES, which has been used in many of the studies (Allaerts and Meyers, 2017, Lu and Porté-Agel, 2011, Wu and Porté-Agel, 2017). LES involves resolving the large eddies while modelling the smaller ones (as an effective viscosity). This is done using low pass filtering and involves finer mesh resolution, which makes it computationally expensive.

The main focus of the present study is to investigate the impact of self-induced AGWs on an offshore wind farm (in terms of velocity and power deficits). While investigating the same, it is necessary to understand the time averaged flow behaviour around the wind farm. This can be achieved using RANS. Further, since the study considers a CNBL, there is no heat flux leaving or entering the bottom of the domain. Also, the CNBL is capped with warmer air in the capping inversion and free atmosphere aloft. These are potential sources of heat flux that can increase the potential temperature at the ground level through entrainment and mixing. Therefore, the potential temperature in the CNBL can change with time, causing a growth of the BL. This temporal evolution can be modelled using an Unsteady RANS (URANS) solver (*solverWithoutTurbine*). The ABL growth caused by the turbulent entrainment of warm air from above is balanced by the CIS at some point. After a few hours, the BL growth rate is minimal and a quasi-steady URANS solution is attained. The vertical profiles of this quasi-steady state are referred to as the fully developed CNBL profiles. These are used as initial and boundary conditions to the main set of simulations, which can then be modelled as a steady RANS solution. The RANS solver used in the present study is called *steadySolverWithoutTurbine*.

Also, RANS has been previously used in the analysis of flow around wind farms by (Ollier et al., 2018, Paul van der Laan and Sørensen, 2016, Paul van der Laan et al., 2015). These studies focus on the mesoscale phenomena such as the impact of the Coriolis force on wind farms and also AGW's. Thus, the choice of RANS would be a good balance between computational power and accuracy, while also being a time tested tool to analyze the present flow problem.

3.2. Governing Equations of flow

The Navier-Stokes equations that govern fluid motion are essentially the Newton's second law for fluids. The flow within the atmosphere can be described by the compressible Navier-Stokes equations (Wyngaard, 2010). They describe an entire range of time and length scales present in atmosphere, ranging from large planetary scales ($\approx 10^5$ km) to mesoscales (≈ 5km) up to dissipative scales of atmospheric turbulence ($\approx 10^{-3}$ m). Further, the compressible equations support a plethora of flow phenomena which include AGWs, Rossby waves and three-dimensional turbulence related motion.

In the case of compressible Newtonian fluids, the momentum equation is as follows:

$$\underbrace{\rho\left(\frac{\partial \mathbf{U}}{\partial t} + \mathbf{U}\cdot\nabla\mathbf{U}\right)}_{1} = \underbrace{-\nabla p}_{2} + \underbrace{\nabla\cdot\left(\mu(\nabla\mathbf{U} + (\nabla\mathbf{U})^T) - \frac{2}{3}\mu(\nabla\cdot\mathbf{U})\mathbf{I}\right)}_{3} + F_{external} \tag{3.1}$$

where in Equation 3.1 $\mathbf{U}$ is the velocity field of the fluid, p is the pressure of the fluid, ρ is the fluid density and μ the fluid dynamic viscosity. In Equation 3.1, terms marked 1 are inertial forces, 2 depict pressure forces, 3 depict viscous/ frictional forces. Lastly, the $F_{external}$ terms depict external forces acting on the fluid such as the buoyancy force ($\rho\mathbf{g}$), the Coriolis force, the forces arising due to Rayleigh damping and the forces exerted due to the presence of the actuator disks.

Along with momentum conservation equations (Newtons second law), the mass conservation equation is the continuity equation which is

$$\frac{\partial \rho}{\partial t} + \nabla\cdot(\rho\mathbf{U}) = 0 \tag{3.2}$$

Here, the Boussinesq approximation is introduced. It is a widely used method to solve non-isothermal flow problems, such as those related to natural convection. The Boussinesq approximation assumes that density variations have no impact on the flow fields, other than giving rise to buoyancy forces. It assumes that the variation of density is only significant in the buoyancy term $\rho\mathbf{g}$ and can be neglected in the rest of the equation.

The inertia force terms in Equation 3.1 get multiplied by a constant density ρ_0 and the buoyancy considers density as a pressure and temperature dependent quantity. Thus, Equation 3.1 becomes:

$$\rho_0\left(\frac{\partial \mathbf{U}}{\partial t} + \mathbf{U}\cdot\nabla\mathbf{U}\right) = -\nabla p + \nabla\cdot\left(\mu(\nabla\mathbf{U} + (\nabla\mathbf{U})^T) - \frac{2}{3}\mu(\nabla\cdot\mathbf{U})\mathbf{I}\right) + \rho\mathbf{g} + \mathbf{F}_{\mathbf{TURBINES}} + \mathbf{F}_{\mathbf{DAMPING}} + \mathbf{F}_{\mathbf{CORIOLIS}} \tag{3.3}$$

The density ρ is then expressed as the sum of a reference density (ρ_0) and a fluctuation component $\Delta\rho$. The continuity and momentum equations yield Equation 3.4 and Equation 3.5 respectively:

$$\underbrace{\frac{\partial(\rho_0 + \Delta\rho)}{\partial t}}_{temporal} + \underbrace{\nabla\cdot((\rho_0 + \Delta\rho)\mathbf{U})}_{convection} = 0 \tag{3.4}$$

$$\begin{aligned}\underbrace{\frac{\partial(\rho_0 + \Delta\rho)\mathbf{U}}{\partial t}}_{temporal} + \underbrace{\nabla\cdot((\rho_0 + \Delta\rho)\mathbf{U}\mathbf{U})}_{convection} = -\nabla p + \nabla\cdot(\mu((\nabla\mathbf{U} + (\nabla\mathbf{U})^T)) - \frac{2}{3}\mu(\nabla\cdot\mathbf{U})\mathbf{I} + \underbrace{(\rho_0 + \Delta\rho)\mathbf{g}}_{buoyancy} \\ + \mathbf{F}_{\mathbf{TURBINES}} + \mathbf{F}_{\mathbf{DAMPING}} + \mathbf{F}_{\mathbf{CORIOLIS}}\end{aligned} \tag{3.5}$$

The Boussinesq approximation allows the treatment of density as a constant in the temporal and convection terms ($\rho = \rho_0$). The only effect of density changes is in the gravity related or buoyancy force terms. This further reduces the continuity equation to its incompressible form

$$\nabla\cdot\mathbf{U} = 0 \tag{3.6}$$

Further, substituting the result of the continuity equation in the momentum equation causes the term $-\frac{2}{3}\mu(\nabla\cdot\mathbf{U})\mathbf{I} = 0$. Furthermore, assuming a constant dynamic viscosity (μ), the momentum equation becomes:

$$\rho_0\left(\frac{\partial \mathbf{U}}{\partial t} + \mathbf{U}\cdot\nabla\mathbf{U}\right) = -\nabla p + \mu\nabla^2\mathbf{U} + \rho\mathbf{g} + \mathbf{F}_{\mathbf{TURBINES}} + \mathbf{F}_{\mathbf{DAMPING}} + \mathbf{F}_{\mathbf{CORIOLIS}} \tag{3.7}$$

Dividing Equation 3.7 by reference density (ρ_0) yields:

$$\left(\frac{\partial \mathbf{U}}{\partial t} + \mathbf{U}\cdot\nabla\mathbf{U}\right) = -\frac{1}{\rho_0}\nabla p + \nu\nabla^2\mathbf{U} + \underbrace{\frac{\rho}{\rho_0}\mathbf{g}}_{buoyancy} + \mathbf{F}_{\mathbf{TURBINES}} + \mathbf{F}_{\mathbf{DAMPING}} + \mathbf{F}_{\mathbf{CORIOLIS}} \tag{3.8}$$

In order to depict the density variation based on change in temperature, the coefficient of thermal expansion needs to be introduced. Mathematically, it is defined as:

$$\beta = -\frac{1}{\rho_0}\left(\frac{\partial \rho}{\partial T}\right)_p \tag{3.9}$$

Making a linear approximation to Equation 3.9 yields $\beta = -\frac{1}{\rho_0}\left(\frac{\partial \rho}{\partial T}\right)_p \approx -\frac{1}{\rho_0}\frac{\rho-\rho_0}{T-T_0}$; $\rho-\rho_0 \approx -\rho_0\beta(T-T_0)$ and $\rho \approx \rho_0[1-\beta(T-T_0)]$. The buoyancy term can be rewritten as:

$$\frac{\rho\mathbf{g}}{\rho_0} = [1-\beta(T-T_0)]\mathbf{g} \tag{3.10}$$

Substituting this into (Equation 3.8) reduces to:

$$\left(\frac{\partial \mathbf{U}}{\partial t} + \mathbf{U}\cdot\nabla\mathbf{U}\right) = -\frac{1}{\rho_0}\nabla p + \nu\nabla^2\mathbf{U} + \underbrace{[1-\beta(T-T_0)]\mathbf{g}}_{buoyancy} + \mathbf{F}_{\mathbf{TURBINES}} + \mathbf{F}_{\mathbf{DAMPING}} + \mathbf{F}_{\mathbf{CORIOLIS}} \tag{3.11}$$

The Boussinesq approximation holds only when the density variation($\Delta\rho$) is very small as compared to the background density (ρ_0) i.e. $\frac{\Delta\rho}{\rho_0} << 1$.

3.3. Reynolds Averaged Navier Stokes (RANS) equations

The RANS equations are time-averaged equations of fluid motion. The fundamental idea behind the equations is the Reynolds decomposition, where an instantaneous quantity is decomposed into its time averaged and fluctuating components (Reynolds, 1895). For example, the quantity of flow velocity $\mathbf{U}$ can be written as:

$$\mathbf{U}(x,y,z,t) = \overline{\mathbf{U}(x,y,z)} + \mathbf{u}'(x,y,z,t) \tag{3.12}$$

where, in Equation 3.12, $\overline{\mathbf{U}}$ is the time average of the flow velocity ($\overline{\mathbf{U}} = \lim_{T\to\infty}\int_{t_0}^{t_0+T}\mathbf{U}dt$, where t_0 is an arbitrary start sampling time) and $\mathbf{u}'$ are the fluctuating components of the same. Further, the properties of the averaging are listed in the following subsection.

3.3.1. Properties of Reynolds Averaging

$$\overline{u'} = 0 \tag{3.13}$$

$$\overline{u+v} = \overline{u} + \overline{v} \tag{3.14}$$

$$\overline{\overline{u}} = \overline{u} \tag{3.15}$$

$$\overline{u\cdot v} = \overline{u}\cdot\overline{v} \tag{3.16}$$

$$\overline{\frac{\partial u}{\partial s}} = \frac{\partial \overline{u}}{\partial s} \tag{3.17}$$

Substituting the velocity as its mean flow and fluctuating component and incorporating the properties of the Reynolds averaging procedure, the equations of continuity in the RANS form is:

$$\nabla\cdot\overline{U} = 0 \tag{3.18}$$

In the case of the momentum equations written below, the buoyancy, Coriolis, turbine and Rayleigh damping forces are clubbed into the $F_{external}$ term. The X, Y, Z momentum equations in the RANS form are as follows:

$$\overline{U}\frac{\partial \overline{U}}{\partial x} + \overline{V}\frac{\partial \overline{U}}{\partial y} + \overline{W}\frac{\partial \overline{U}}{\partial z} + \frac{\partial \overline{u'u'}}{\partial x} + \frac{\partial \overline{v'u'}}{\partial y} + \frac{\partial \overline{w'u'}}{\partial z} = -\frac{1}{\rho_0}\frac{\partial p}{\partial x} + \nu\nabla^2\overline{U} + F_{external(X)} \tag{3.19}$$

$$\overline{U}\frac{\partial \overline{V}}{\partial x} + \overline{V}\frac{\partial \overline{V}}{\partial y} + \overline{W}\frac{\partial \overline{V}}{\partial z} + \frac{\partial \overline{u'v'}}{\partial x} + \frac{\partial \overline{v'v'}}{\partial y} + \frac{\partial \overline{w'v'}}{\partial z} = -\frac{1}{\rho_0}\frac{\partial p}{\partial y} + \nu\nabla^2\overline{V} + F_{external(Y)} \tag{3.20}$$

$$\overline{U}\frac{\partial \overline{W}}{\partial x} + \overline{V}\frac{\partial \overline{W}}{\partial y} + \overline{W}\frac{\partial \overline{W}}{\partial z} + \frac{\partial \overline{u'w'}}{\partial x} + \frac{\partial \overline{v'w'}}{\partial y} + \frac{\partial \overline{w'w'}}{\partial z} = -\frac{1}{\rho_0}\frac{\partial p}{\partial z} + \nu\nabla^2\overline{W} + F_{external(Z)} \tag{3.21}$$

The occurrence of fluctuating quantities on the right-hand side of Equation 3.19, Equation 3.20 and Equation 3.21 is the source of the turbulence closure problem. In the present case, a second order turbulence closure based on two transport equations for the turbulent kinetic energy (k) and turbulent dissipation rate (ϵ) (Koblitz et al., 2015, Sanz Rodrigo et al., 2017, Sogachev et al., 2012) is used in the present case. The $k - \epsilon$ model (Hargreaves and Wright, 2007) has been widely used for studying ABL flows by Apsley and Castro (1997),Paul van der Laan et al. (2015), Paul van der Laan and Sørensen (2016) and also used to study AGWs (Ollier et al., 2018). The transport equations for k and ϵ are:

$$\frac{\partial k}{\partial t} = B + P - \epsilon + \frac{\partial}{\partial z}\left(\frac{K_m}{\sigma_k}\frac{\partial k}{\partial z}\right) \tag{3.22}$$

$$\frac{\partial \epsilon}{\partial t} = \frac{\epsilon}{k}(C^*_{\epsilon 1}P - C_{\epsilon 2}\epsilon + C_{\epsilon 3}B) + \frac{\partial}{\partial z}\left(\frac{K_m}{\sigma_\epsilon}\frac{\partial \epsilon}{\partial z}\right) \tag{3.23}$$

where in Equation 3.22, Equation 3.23, σ_k and σ_ϵ are Schmidt numbers [1] for k and ϵ, B and P are the buoyancy production rates and shear production rates of k respectively. Further, $C_{\epsilon 2}$ and $C_{\epsilon 3}$ are model coefficients. Furthermore, the eddy viscosity is defined as $K_m = C_\mu k^2/\epsilon$, where C_μ is the coefficient which equals the square of the ratio of shear stress and turbulent kinetic energy in equilibrium. The model coefficients used are $C_{\epsilon 1} = 1.52$,$C_{\epsilon 2} = 1.833$,$\sigma_k = 2.95$,$\sigma_\epsilon = 2.95$,$C_\mu = 0.03$ as mentioned in Sanz Rodrigo et al. (2017). Further details of the solver are as mentioned in section 2 of Sanz Rodrigo et al. (2017).

Further, as buoyancy effects are significant to the present flow problem, it is necessary to solve a conservation equation for the potential temperature (θ). In the present study, the radiative and phase-change heat transfer effects are assumed to be absent. The energy equation written in terms of the conservation of potential temperature is as follows:

$$\frac{\partial \theta}{\partial t} = -\nabla \cdot u\theta + \nabla \cdot \kappa_{eff}\nabla\theta \tag{3.24}$$

where, in Equation 3.24, κ_{eff} is the sum of the viscous and turbulent contributions of the thermal diffusion coefficient. The diffusion related terms in the momentum equation are simulated assuming an isotropic eddy viscosity, which relates the turbulent fluxes to the gradients of the mean flow quantities. $w\theta = \frac{K_m}{Pr}\frac{\partial \theta}{\partial z}$ where Pr - the Prandtl number [2] is assumed to be equal to 1. The eddy viscosity K_m is the product of the mixing length and velocity scales.

3.4.The external force terms

In Equation 3.19, Equation 3.20 and Equation 3.21, the external force terms include the gravity/ buoyancy force, the Coriolis force, the turbine force and the forces arising due to the implemented Rayleigh damping layer. The definition and the mathematical expressions for these external forces are explained in the following subsections.

---

[1] Schmidt number is a dimensionless quantity which is the ratio of the kinematic viscosity (momentum diffusivity) and mass diffusivity

[2] The Prandtl number is a dimensionless number which is defined as the ratio of momentum diffusivity to thermal diffusivity

3.4.1. The Coriolis force

It is calculated as

$$\mathbf{F_{CORIOLIS}} = -2\vec{\Omega} \times \mathbf{v} \tag{3.25}$$

whereupon further resolution of the vectors ($\vec{\Omega}$ and $\mathbf{v}$) in the (X, Y, Z) directions, the component orthogonal to the velocity over the earth surface is given as $2\omega v sin\phi$ where ω is the rate of the earth's rotation and ϕ is the latitude of the location of interest. The Coriolis parameter (f) is calculated as $f = 2\omega sin\phi$.

3.4.2. Actuator Disk forces

In the present study, turbines are modelled as actuator disks. Since the main focus of the present study is to study the impact of self-induced AGWs on an offshore wind farm, a complete resolution of the boundary layer phenomena at each turbine is unfeasible. Thus, the turbines are modelled as actuator disks. Further, the impact of the tower mounting the wind turbine is neglected in the present study.

Earlier studies involving flow simulation around large wind farms such as (Allaerts, 2016, Allaerts and Meyers, 2015, 2017, Meyers and Meneveau, 2010b, Wu and Porté-Agel, 2015) have used actuator disks to represent the wind turbines. In the current study, non-rotating Actuator Disks (AD) is used to represent individual turbines, in which the tangential forces are neglected.

The traditional implementation of the Actuator Disk Model (ADM) in OpenFoam6 (OF6) is based on the classical ADM (Jenkins et al., 2001), where the Actuator Disk is defined as a cylinder of a user-defined radius and thickness with specified values of the thrust coefficient (C_T) and the power coefficient(C_P). Further, this implementation of the ADM uses the undisturbed reference velocity to calculate the thrust force that the turbine exerts upon the flow. In the case of very large wind farms, due to the considerable amount of interaction between wind farm wakes, the definition of the upstream velocity at each individual turbine and the point where it is sampled is ambiguous and a disk-based approach is more accurate. Thus, a disk based approach is necessary. In this approach, the disk-based thrust coefficient $C_T^{'}$ represents the overall effect of the blade lift and drag forces on the air flow at the actuator disk. It is mathematically calculated as:

$$C_T^{'} = \frac{C_T}{(1-a)^2} \tag{3.26}$$

Further, the disk based thrust force exerted by the turbine is calculated as:

$$\delta F_x = -\frac{1}{2} C_T^{'} \rho_0 \overline{V}^2 \delta A \tag{3.27}$$

where, in Equation 3.27, $\overline{V}$ is the velocity magnitude perpendicular to the actuator disk (unlike the reference velocity used in the traditional implementation). The disk based approach was previously used in Calaf et al. (2010), Meyers and Meneveau (2010a), Allaerts (2016), Wu and Porté-Agel (2013). The current thesis considers an NREL 15 MW turbine having a rotor diameter of $240\,m$ and a hub height of $150\,m$. The details of the wind turbine can be found in (Gaertner et al., 2020). Also, the study only considers turbines operating in region 2, i.e. below the rated wind speed. In this region, an optimal Tip Speed Ratio (TSR) is maintained by varying the generator torque. In this region, the thrust coefficient remains constant, which further allows for the turbines to be represented by actuator disks of constant C_T. This region is depicted by the constant design thrust coefficient of 0.804 in Figure 3.1.

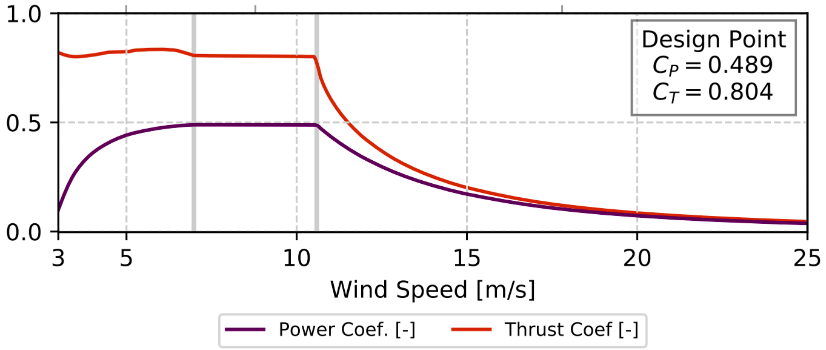

Figure 3.1: Thrust and power curves of 15MW International Energy Agency (IEA) wind turbine (Reproduced from: (Gaertner et al., 2020))

Further, based on the classical AD theory, the axial induction factor (a) is calculated by equating $4a(1-a) = 0.804$. Solving this yields values of $a = 0.72136$ and $a = 0.2787$. Since the ADM is invalid at induction factors ($a > 0.5$), the value of $a = 0.2787$ is considered. This is used along with the design thrust coefficient ($C_T = 0.804$) to get $C_T^{'} = 1.5453$. Similar representations have been used by (Nilsson et al., 2015) to represent the turbines operating within the Lilligrund wind farm ($C_T = 0.812 \implies C_T^{'} = 1.58$) and studies of the Horns Rev I farm ($C_T = 0.78 \implies C_T^{'} = 1.45$) (see (Munters et al., 2016, Richard J.A.M. Stevens and Meneveau, 2015). Further, the effect of the tower is neglected in the present study.

3.4.3. Rayleigh damping layer

As the flow develops in and around the wind farm, AGWs are triggered in the Free Atmosphere and the capping inversion. These AGW's reflect at the domain boundaries (Allaerts, 2016). The reflected waves propagate downwards and contaminate the model solutions. In order to damp out these spurious AGW reflections, damping layers are implemented (Warner, 2010).

This is achieved by implementing a wave absorbing layer (also called sponge layer) having enhanced values of artificial horizontal or vertical diffusion (viscosity). Further, the absorbing layer may need to be thick, which would require a large computational overhead (Warner, 2010). (Klemp and Lilly, 1978) has defined the upper half of their domain as the absorbing layer. In the Rayleigh damping term, the prognostic equation would be of the form (Warner, 2010):

$$\frac{\partial x}{\partial t} = \tau(z)(x - \overline{x}) \tag{3.28}$$

where x is any dependent variable,$\overline{x}$ is the reference value of the variable and $\tau(z)$ is the damping coefficient which increases within the domain (Klemp and Lilly, 1978). Furthermore, Klemp and Lilly (1978) had determined the depth of the damping layer at the top of the domain to be of the order of one vertical wave length. As the hydrostatic assumption holds good in the present case (similar to the work by Allaerts (2016)), the vertical wavelength (λ_z) of the AGW can be mathematically defined as:

$$\lambda_z = 2\pi U/N \tag{3.29}$$

where in Equation 3.29, N is the Brunt–Väisälä frequency as mentioned in Equation 1.1. In the free atmosphere, the two values of atmospheric stratification considered in the present study are $1K/km$ and $10K/km$. Based on these values, the vertical wavelengths calculated come out to be $10803\,m$ and $3416.2\,m$ respectively. The Rayleigh damping layer was also implemented in Lu and Porté-Agel (2011), Hills and Durran (2012), Abkar and Porté-Agel (2013), Allaerts and Meyers (2017), Gadde and Stevens (2019) and Haupt et al. (2020). While Lu and Porté-Agel (2011), Abkar and Porté-Agel (2013) have implemented a Rayleigh damping layer at $300\,m$ following the GABLS case description, there is no mention of the values of other damping parameters such as the height and maximum Rayleigh damping coefficient. Further, Hills and Durran (2012) had implemented a $16km$ thick damping layer (starting at

$20\ km$ and extending till the top of the domain) with a maximum coefficient of $0.005s^{-1}$. However, this study considers the flow over a 3D mountain ridge and not a wind farm.

Allaerts and Meyers (2017) implemented a $10\ km$ thick Rayleigh damping layer, having a cosine profile (smoothly increasing) damping coefficient of $0.0001s^{-1}$. However, the study uses LES and also assumes a wind farm having an infinite span-wise length. Gadde and Stevens (2019) implemented a Rayleigh damping layer with a damping coefficient of $0.016s^{-1}$ considered in the top $1\ km$ of the computational domain. Lastly, Haupt et al. (2020) who studied the 2D flow over a 100 m tall hill had mentioned that a strong damping layer can cause the gravity waves to reflect off the damping layer. The damping strength of $0.005s^{-1}$ was used in all cases. They examined the effects of the domain length and the inflow and outflow damping layers and found that shortening the downstream side of the domain and not using outflow damping resulted in the formation of upstream spurious wave patters. Placing a Rayleigh damping layer at the exit seemed to mitigate the problem. The study shortened the domain length upstream of the hill and placed damping layers at the inlet, exit and top of the domain and found that the solution obtained reasonably agreed with its analytical counterpart. However, this is for a 2D case with a hill and not a wind farm. Further, the study uses LES and not RANS.

The Rayleigh damping appears as an external force term $F_{DAMPING}$ in the momentum equations. Mathematically, it can be expressed as:

$$F_{DAMPING} = c(U_{ref} - U) \tag{3.30}$$

In Equation 3.30, c is calculated from the expressions:

$$c = \frac{c_{max}}{2}\left(1 - f \cdot cos\left(\Pi\frac{z - z_{start}}{w}\right)\right) \tag{3.31}$$

where in Equation 3.31,z_{start} is the start height of the Rayleigh Damping Layer, c_{max} is the amplitude of the damping value and w is the thickness of the damping layer.

3.5. Solver Algorithm

In the present study, two CFD RANS solvers (authored by Julia Steiner, a PhD scholar at TUDelft (personal communication)) has been used. One is a steady state RANS solver - *steadySolverWithoutTurbine* and the other is a URANS solver *solverWithoutTurbine*.

The steady RANS solver - *steadySolverWithoutTurbine* is built upon the existing *buoyantBoussinesqSimpleFoam* solver. This is a steady-state solver used for buoyant, turbulent flow of incompressible fluid which uses a SIMPLE (Semi-Implicit Method for Pressure Linked Equations)[3] algorithm for pressure velocity coupling. The major modification to the original *buoyantBoussinesqSimpleFoam* solver is the solution of an additional transport equation of potential temperature. The URANS solver - *solverWithoutTurbine* is based on the architecture of the Unsteady RANS solver - *buoyantBoussinesqPimpleFoam*. This is a transient solver used for buoyant, turbulent flow of incompressible fluid which uses PISO (Pressure-Implicit with Splitting of Operators) algorithm for pressure velocity coupling.

3.6. Simulation suite

In order to understand the impact of each atmospheric parameter viz. thermal stratification in the free atmosphere (Free Atmosphere Lapse Rate (FALR)), the Capping Inversion Height (CIH) and Capping Inversion Strength (CIS) each of these parameters should be varied individually. Since the present study considers two values of each of the three parameters, a total of eight simulations are planned. Each of these cases are numbered from 0 to 7 as shown in the table Table 3.1 below:

---

[3] The SIMPLE algorithm has been discussed in detail in the appendix

NAME	***CIS [K]***	***CIH [m]***	**FALR [K/km]**
Case0	2.5	500	1
Case1	2.5	500	10
Case2	2.5	1000	1
Case3	2.5	1000	10
Case4	10	500	1
Case5	10	500	10
Case6	10	1000	1
Case7	10	1000	10

Table 3.1: Suite of planned simulations

Further, each simulation is preceded by a precursor single column model simulations. The justification of the same as a suitable precursor simulation will be discussed later in Chapter 5.

3.7. Summary

The present chapter provides an overview of the two CFD RANS solvers used in the present study. Further, the RANS equations are presented. This is followed by the numerical implementation of the wind turbines, the Rayleigh damping layers and the Coriolis force. These appear as the external force terms in the momentum equations. Lastly, the chapter also sheds light on the suite of the planned simulations which need to be performed in order to achieve the research objective. The next chapter presents the setup and results of the benchmark simulations which have been carried out to test the efficacy of the two solvers - *steadySolverWithoutTurbine* and *solverWithoutTurbine*.

4

Benchmark studies

In order to validate the working of the two CFD solvers - i.e. *steadySolverWithoutTurbine* and *solverWithoutTurbine* being used to simulate the present case, two benchmark simulations were carried out, one for each of the solvers. The first simulation tests the efficacy of the URANS solver - *solverWithoutTurbine* to obtain fully developed ABL profiles, and the second study tests the ability of the RANS solver *steadySolverWithoutTurbine* to simulate steady flow over wind turbines.

4.1.Benchmark 1 -*solverWithoutTurbine*

In the present section, the use of the Unsteady RANS (URANS) solver - *solverWithoutTurbine* is tested to predict velocity, horizontal flow direction and potential temperature profiles within a Conventionally Neutral Boundary Layer (CNBL). Two simulations of neutral ABL developing against two stable background lapse rates of $\gamma = 1K/km$ and $\gamma = 10K/km$ are considered. The results are compared with Abkar and Porté-Agel (2013)(WiRE LES), Allaerts (2016)(SP Wind) and Pedersen et al. (2014a)(NCAR LES).

4.1.1. Case setup

The simulation is set up to match cases n_{01} and n_{04} of Pedersen et al. (2014a). The case setup for the URANS simulation is summarized in the Table 4.1

Reference temperature (θ_o)	290 K
Free Atmosphere Lapse Rate (γ)	1K/km and 10K/km
Aerodynamic surface roughness (f_c)	0.01
Geostrophic wind speed (G)	10 m/s
Latitude considered (ϕ)	$43.43°$
Coriolis parameter ($f_C = 2\Omega(sin\phi)$)	0.0001 s^{-1}
Domain size ($L_x \times L_y \times L_z$)	$20m \times 20m \times 2000m$
Grid resolution ($\delta x \times \delta y \times \delta z$)	$10m \times 10m \times 10m$
Number of grid points ($N_x \times N_y \times N_z$)	$2 \times 2 \times 200$

Table 4.1: Case setup for bench-marking the first solver

The atmospheric flow is simulated in a Single Column Model (SCM) of the atmosphere. A single column model is one in which the physical domain sizes in the stream-wise and span-wise directions are small as compared to the height of the domain. As the study considers horizontally homogeneous conditions, the physical extent of the domain in the horizontal directions would have no impact on the solutions obtained. Thus, this warrants the use of the SCM approach.

The physical extent of the domain is $20\ m$ in the stream-wise and span-wise directions, and $2000\ m$ in the vertical direction. The vertical height of the domain is equal to those considered in the other studies. Furthermore, the bottom surface is a *zeroGradient* [1] patch for all the following flow variables - k, ϵ, θ. The boundary condition for velocity at the bottom wall is a *noSlip*. All the lateral faces in the span-wise and stream-wise directions have *cyclic* or *periodic* boundary conditions. The initial value of velocity is $10m/s$. Further, the initial value of potential temperature have a uniform linear gradient of $1K/km$ and $10K/km$.

4.1.2. Results and Discussion

The simulations are advanced in time for 24 hours. The planar averaged profiles of the horizontal velocity magnitude ($\sqrt{u^2 + v^2}$), the horizontal flow direction ($\phi = tan^{-1}\left(\frac{v}{u}\right)$), and the potential temperature (θ) become quasi-steady after about 20 hours. Figure 4.3 shows the vertical planar averaged profiles of these quantities averaged over the last hour.

The plots of variation of planar velocity magnitude in the vertical direction non-dimensionalise the vertical height with the height of the BL ($h1$). Each of the studies considered in the present benchmark case define $h1$ differently. While, Abkar and Porté-Agel (2013)(WiRE LES) calculates $h1$ as the height at which the momentum flux reaches 5 percent of the magnitude at the surface, Allaerts (2016)(SP-Wind), considers the boundary layer height $h1$ as the centre of the inversion layer which is determined by a best fit analysis of the steady state vertical potential temperature profile as predicted by Rampanelli and Zardi (2004). However, Pedersen et al. (2014b) does not indicate the method of calculating $h1$. In the present study, the definition of $h1$ is similar to Allaerts (2016), i.e. it is the centre of the inversion layer.

The base of the inversion layer is identified as the height at which the potential temperature begins to show variation from the uniform value. Further, the top of the inversion layer is the height above the inversion base at which the potential temperature first equals the lapse rate in the free atmosphere ($\Gamma = 1K/km$ or $\Gamma = 10K/km$). The centre of the inversion layer is taken as the geometric mean of the base and top of the inversion layer.

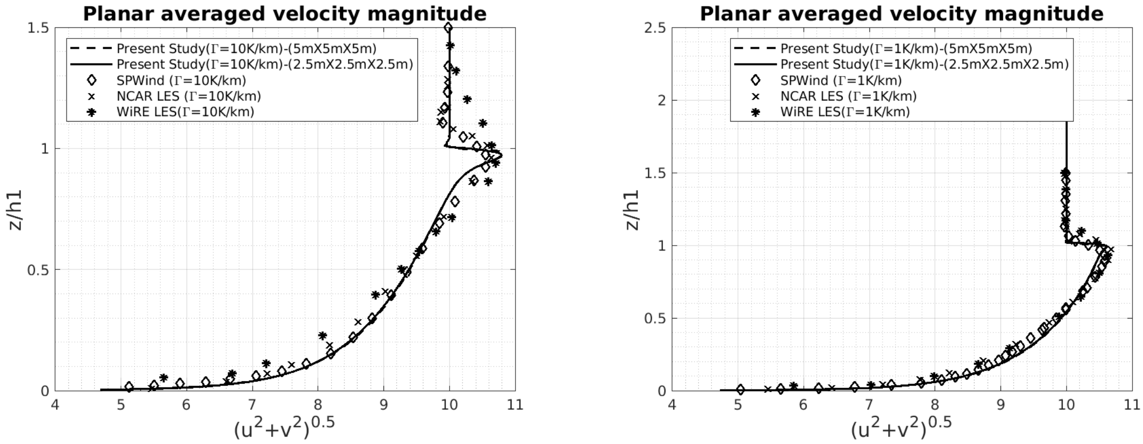

(a) Vertical profile of Planar averaged velocity magnitude for $\Gamma = 10K/km$ (in m/s)

(b) Vertical profile of Planar averaged velocity magnitude for $\Gamma = 1K/km$ (in m/s)

Figure 4.1: Vertical profiles of planar velocity magnitude (in m/s) of the present study model vis-à-vis other LES codes Allaerts (2016) (SPWind), Pedersen et al. (2014a) (NCAR LES) and Abkar and Porté-Agel (2014) (WiRE LES)

From Figure 4.1a, Figure 4.1b, it can be observed that the vertical profiles of the planar horizontal velocity ($\sqrt{u^2 + v^2}$) correspond reasonably with the values predicted by other LES codes, viz. WiRE LES, NCAR LES, SPWind. Also, the sharp change in the planar avergaed horizontal velocity magnitude and the maximum value of the super geostrophic velocity below the ABL height match reasonably well with other LES solvers. However, it should be noted that the velocity magnitude shows a sharp jump of

---

[1] *zeroGradient* condition extrapolates the quantity to the patch from the nearest cell value

velocity at the boundary layer height. The reason for the jump in velocity can be understood as follows: in the free atmosphere, the wind velocity magnitude equals, $10m/s$ and this is the geostrophic velocity. Further, in the layer below the inversion base (the surface layer), the wind velocity magnitude is affected by the friction with the earth surface. Thus, the velocity magnitude is less than the geostrophic velocity in this region. Across the inversion, the geostrophic velocity in the free atmosphere is matched with the reduced velocity values below the inversion. This gives rise to the sharp jump in the velocity magnitude. Further, the occurrence of the super geostrophic velocity below the top of the ABL is common in the cases of a neutral boundary layer capped by an inversion (Blackadar, 1957, Pedersen et al., 2014b). Furthermore, the reason for the existence of the super geostrophic velocity (jet) is due to the interaction of the alternate horizontal stress and momentum components, which is induced by the Coriolis force (Van Der Laan et al., 2021, Wyngaard, 2010).

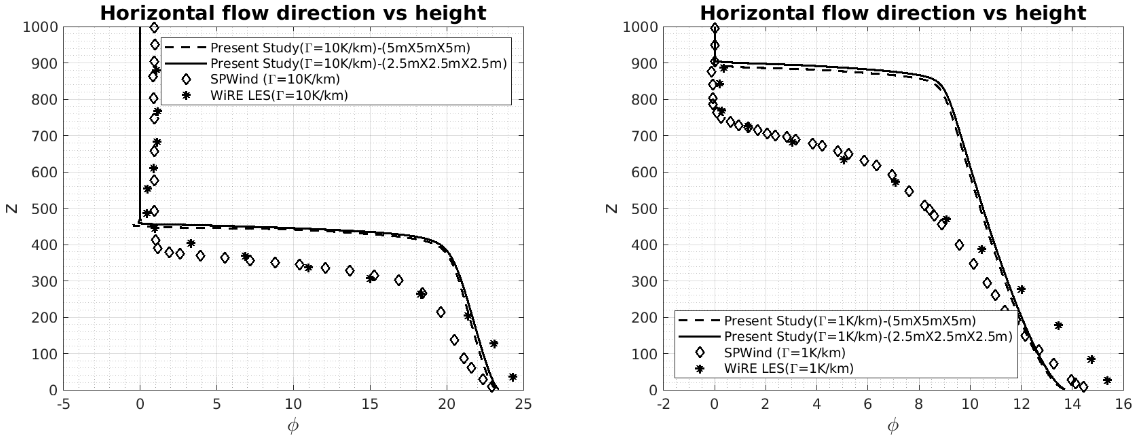

(a) Vertical profile of planar averaged horizontal flow direction $\phi = tan^{-1}(v/u)$ ($\Gamma = 10K/km$)

(b) Vertical profile of planar averaged horizontal flow direction $\phi = tan^{-1}(v/u)$ ($\Gamma = 1K/km$)

Figure 4.2: Vertical profiles of planar averaged horizontal flow direction of the present study vis-à-vis other LES codes Allaerts (2016) (SPWind), Pedersen et al. (2014a) (NCAR LES), Abkar and Porté-Agel (2014) (WiRE LES)

A change in flow direction can be observed in Figure 4.2a and Figure 4.2b. This is because, in the free atmosphere, the wind velocity vector is the result of the pressure gradient force and the Coriolis force (the geostrophic balance). However, in the layer below the base of the inversion layer, the Coriolis force (which is linearly dependent on the wind velocity magnitude) is lower due to the reduced velocity magnitude in this region. Therefore, the direction of the resultant flow changes, and it becomes more aligned with the imposed pressure gradient. Across the inversion layer, the flow turns from the geostrophic direction in the free atmosphere to the resultant direction within the surface layer. This is observed as a sharp change in the horizontal flow direction in Figure 4.2a and Figure 4.2b. However, the URANS solver is unable to smoothly resolve the change in the wind direction and wind velocity above and below the inversion layer.

Further, from Figure 4.3, it can be observed that the values predicted by the current solver agree reasonably well with the other LES codes for $\Gamma = 10K/km$ while for $\Gamma = 1K/km$ the values are within the same order of magnitude as predicted by other LES solvers. [2].

---

[2] The comparative values for the other LES solvers are obtained by digitizing values from Allaerts (2016) using the web plot digitizer - Automeris

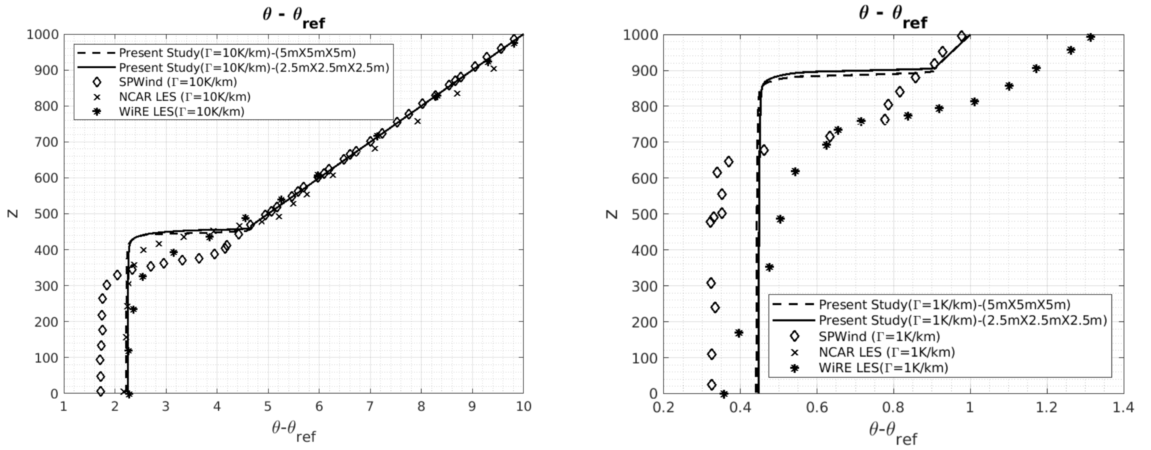

(a) Variation of potential temperature (in K) with height for $\Gamma = 10K/km$ (b) Variation of potential temperature (in K) with height for $\Gamma = 1K/km$

Figure 4.3: Vertical profiles of potential temperature of the present study vis-à-vis other LES codes Allaerts (2016) (SPWind), Pedersen et al. (2014a) (NCAR LES), Abkar and Porté-Agel (2014) (WiRE LES)

In the present benchmark study, the height of the inversion base, its thickness and strength are the quasi-steady outcome of a URANS solution. However, for the main set of simulations, the initial base height of the capping inversion and its strength are user specified values, which are allowed to develop further into quasi-steady profiles. Therefore, an over-predicted value of h_1 as seen in Figure 4.5d is acceptable.

4.2. Benchmark 2 - steadySolverWithoutTurbine

In the present section, the ability of the steady RANS solver - *steadySolverWithoutTurbine*, to perform flow simulations around wind turbines (represented as actuator disks) is tested. In order to achieve this, the case is set up to match the wind tunnel test setup of the 4th Blind Test Experiment (BT4) organized by NOWITECH and Norwegian Research Cluster for Offshore Wind Energy (NORCOWE) in 2015 (Bartl and Sætran, 2017, Sætran and Bartl, 2015, Stergiannis et al., 2016).

4.2.1. Case setup

Two model wind turbines (each having rotor diameter $D = 0.894m$) are placed one behind the other at three axial separation distances, viz. $x/D = 2.77, 5.18, 9$. Further, the wind tunnel experiments use three controlled turbulent uniform inflow conditions. These turbulent inflow conditions are achieved by placing an evenly spaced turbulence grid at the wind tunnel inlet which generates a desired amount of Turbulence Intensity (TI) at the upstream turbine, while maintaining a uniform wind speed across the test section. Further, the velocity is measured at three points (2.77D,5.18D and 8.5D) downstream of the first turbine.

The computational domain is designed to match the dimensions of the wind tunnel test section (see Figure 4.4). Also, the initial and boundary conditions are chosen to mimic the wind tunnel experiment based on the study carried out by (Stergiannis et al., 2016).

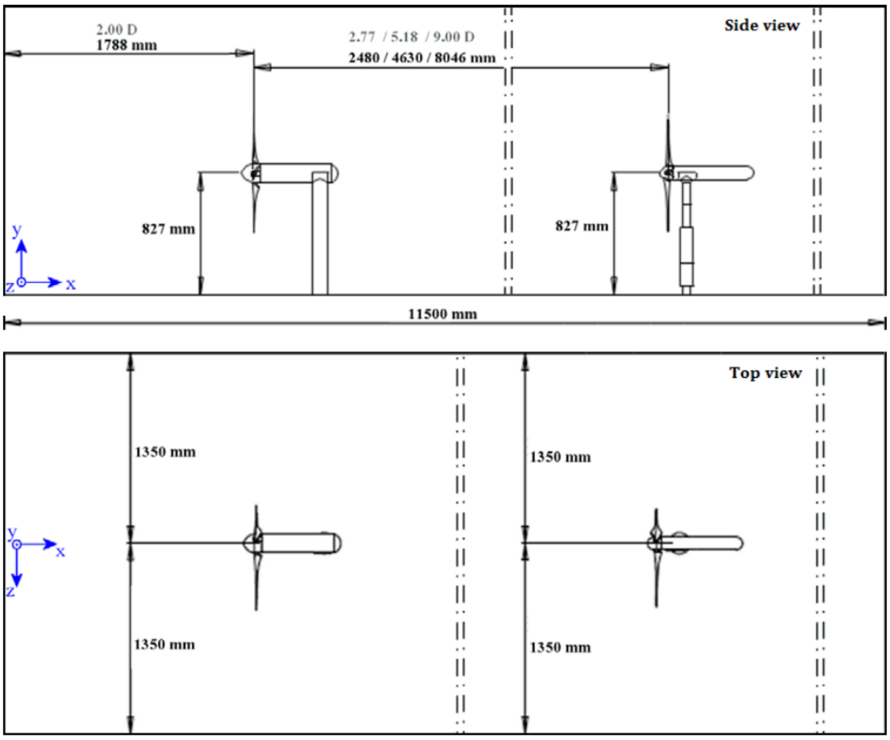

Figure 4.4: Dimensions of the wind tunnel test section (figure reproduced from Sætran and Bartl (2015),Stergiannis et al. (2016))

The *blockMesh*[3] utility of OpenFOAM is used to generate a structured hexahedral grid having a grid resolution of $5\,mm$ in all directions. Further, the turbines are represented as classical actuator discs (based on the OpenFoam implementation of the ADM) having the same diameter as that of the model turbine with specified values of power and thrust coefficients (values give in Table 4.2).

	Upstream Turbine	**Downstream Turbine**
C_P	0.468	0.270
C_T	0.833	0.569

Table 4.2: The power coefficient (C_P) and thrust coefficient (C_T) values are the experimental values for T_1 and T_2 for test case B_3 from Table 5 (Bartl and Sætran (2017))

The boundary conditions of the inflow, outflow boundaries are as shown in Table 4.3. Further, slip conditions are assumed for $\overline{U}, k, \epsilon$ at all the lateral boundaries.

	Dirichlet (Fixed Value)	***Neumann (zeroGradient)***
Inlet	$\overline{U}, k, \epsilon$	p
Outlet	p=0	$\overline{U}, k, \epsilon$

Table 4.3: Types of boundary conditions implemented at the inlet and exit of the domain

The boundary conditions are tuned to obtain the inflow conditions of the B_3 case (see (Bartl and Sætran, 2017)). Further, $\overline{U} = 11.5 m/s$ and the values of k, ϵ are calculated using the following relations:

$$k = \frac{3}{2}(\overline{U}.TI)^2 \tag{4.1}$$

$$\epsilon = C_\mu^{0.75}\frac{k^{1.5}}{l} \tag{4.2}$$

---

[3] The blockMesh utility of OF6 is used to create parametric meshes with grading or with curved edges

where the turbulent length scale (l) is found for the test case B_3 as $0.065m$ from (Bartl and Sætran, 2017). The inlet values were adjusted to get $TI = 10\%$ at the first turbine position, similar to the experimental setup. Further, the wind turbines are placed at an axial separation distance of $9D$.

4.2.2. Results and Discussion

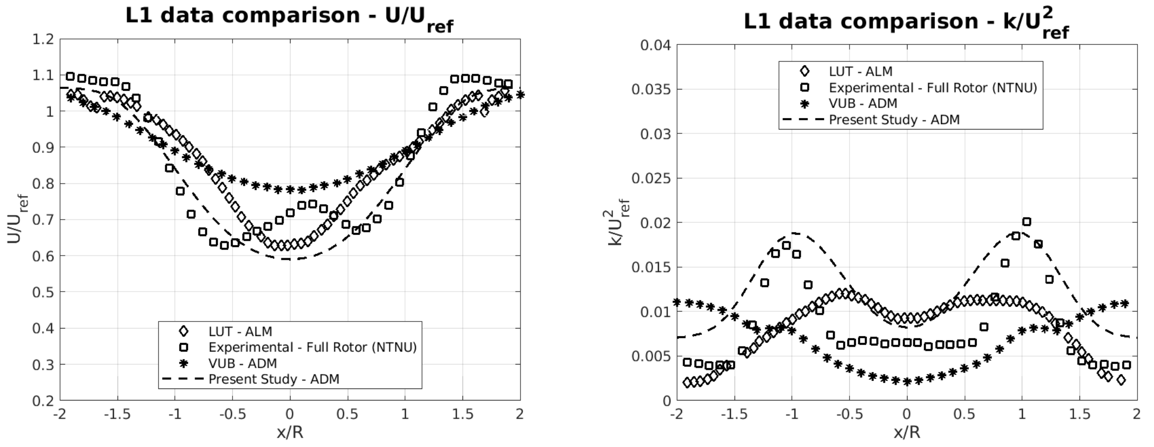

(a) Non-dimensional velocity profile at 2.77D or L1 (b) Non-dimensional profile of TKE at 2.77D or L1

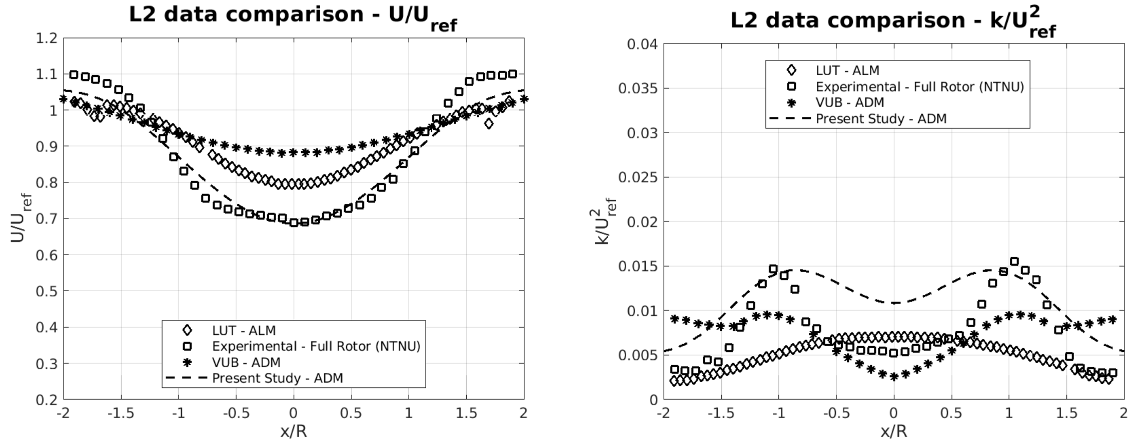

(c) Non-dimensional velocity profile at 5.18D or L2 (d) Non-dimensional profile of TKE at 5.18D or L2

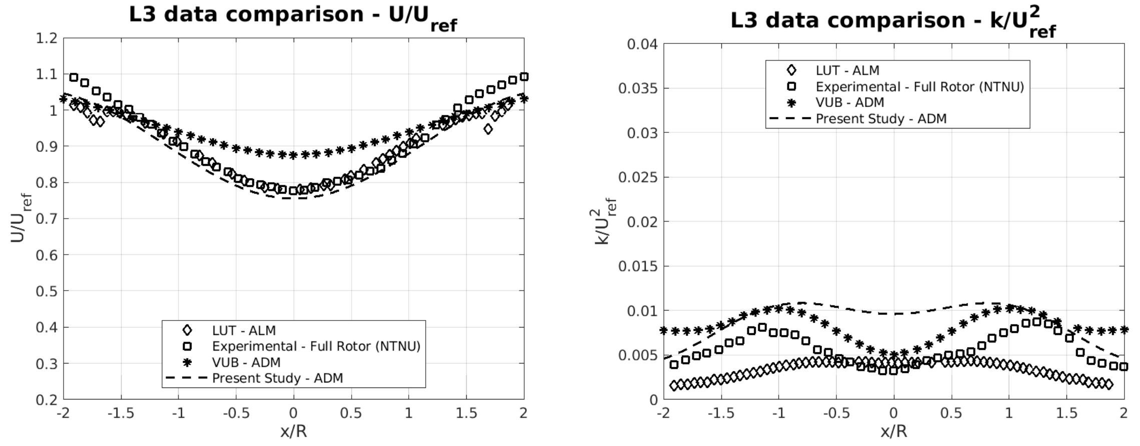

(e) Non-dimensional velocity profile at 8.5D or L3 (f) Non-dimensional profile of TKE at 8.5D or L3

Figure 4.5: Non-dimensional profiles of velocity, Turbulent Kinetic Energy(TKE) compared with experimental values and other computational studies modelling the same (Bartl and Sætran (2017), Stergiannis et al. (2016) - The values obtained by Łódź University (LUT(ALM)) and Experimental - Full Rotor (NTNU) are extracted from Figure 8 in Bartl and Sætran (2017) using the graph digitizer Automeris)

The numerical results are compared with its experimental counterparts and the Actuator Line Model of the wind turbine (as implemented by Łódź University of Technology (LUT)) and an Actuator Disc Model (as implemented by Vrije University, Brussels (VUB)) (Bartl and Sætran, 2017). The horizontal profiles of the velocity and the Turbulent Kinetic Energy (TKE) at the hub height of the turbine are recorded at positions $2.77D$ (L1), $5.18D$ (L2) and $8.5D$ (L3) downstream of the first turbine. The velocity magnitude and TKE values are normalized by the reference velocity $U_{ref} = 11.5m/s$ and, U_{ref}^2 respectively.

The results shown in Figure 4.5 show non-dimensional velocity profiles (see Figure 4.5a, Figure 4.5c and Figure 4.5e). The velocity profiles as predicted by the ADM and ALM exhibit an upside down symmetric profile about the axis of the turbine. This is indicative of a uniformly loaded actuator disk. However, the values predicted by the experiment show a non-symmetric velocity deficit in the near wake region (L1). This is caused by the advection of the tower wake into the rotating rotor wake, as shown by experiments (Bartl and Sætran, 2017, Schümann et al., 2013). The presence of the actuator disks in the flow field results creates a shear layer at the circumference of the disk. This leads to the turbulence generation shown by the double peaks in the non-dimensional TKE plots (see Figure 4.5b, Figure 4.5d and Figure 4.5f).

From Figure 4.5a, it can be observed that the velocity deficit behind the actuator disks as predicted by the current benchmark study shows a difference as compared to the experimental values. This is because the turbine is modelled as an Actuator Disk at the hub height of the model turbine. As the tower and nacelle have not been modelled and are neglected in the present benchmark study, the impact of vortex shedding from the same is absent in the velocity deficit plots. However, the minimum amount of velocity deficit is similar in both the cases. Further, at a downstream distance of 5.18D (L2) from the first turbine (Figure 4.5c), the velocity deficit predicted by the present study is in good agreement with its experimental counterpart. The impact of the tower wake on the wake of the upstream turbine is not clearly visible. This may be attributed to the turbulent mixing occurring in the wake of the farm (Schümann et al., 2013). Also, the velocity deficit assumes an inverted Gaussian profile. Further downstream, at L3 (see Figure 4.5e), the inverted Gaussian profile of velocity deficits are well-developed and the predicted velocity deficit values are in very close agreement with its experimental counterparts. Also, in this region, there is a further decrease in the velocity deficit. This can be attributed to the wake recovery occurring due to turbulent mixing in the wake of the first turbine.

Further, the shearing of the flow at the disk circumference creates a symmetric non-dimensional profile of TKE. The two peaks are due to the flow shear at the circumference, which leads to the creation of tip vorticity. The thickness of the actuator disk defines the amount of turbulence generation and dissipation (Daaou Nedjari et al., 2020). Daaou Nedjari et al. (2020) had found that the thickness of the actuator disk should be close to the chord length of the turbine to get an accurate depiction of the near wake velocity deficits and also to reduce the difference in the far wake velocity deficits. However, Daaou Nedjari et al. (2020) does not specify the exact value of ideal actuator disk thickness. The model turbines used in the present study show a radial variation of the chord length (see Table 5 in Sætran and Bartl (2015)). Thus, an average of these values are taken as the actuator disk thickness ($\approx 50mm$). From Figure 4.5b, at 2.77D downstream of the first turbine, it can be observed that the peaks due to the turbulence generation at the disk circumference show a greater spread as compared to its experimental counterpart. This can be attributed to the difference in geometry of the actuator disk as compared to the actual model turbines. Further, upon comparing Figure 4.5d and Figure 4.5f, it can be observed that at L3, the tip vortex decays to about 50% of the magnitude at 5.18D. This is because of the wake mixing and absence of any further flow perturbations that reduce the amount of the TKE at downstream distances.

Therefore, it can be concluded that the actuator disk model can be used to represent turbines in a large scale wind farm.

4.3. Summary

The present chapter presents the results of each benchmark simulation for the RANS and the URANS solvers. Furthermore, the results obtained are discussed and validated against existing literature. The following chapter presents the case setup of the planned simulation suite, followed by the discussion of the results obtained. Lastly, conclusions are drawn based on the successful simulations performed.

5

Wind farm in a CNBL

The present chapter sheds light on the case setup and results of the flow simulations over an entire wind farm of finite span-wise and stream-wise length. Further, the chapter is divided into two main sections, which are further divided into subsections. The first section provides an overview of the setup of the precursor simulations, followed by a presentation and discussion of results obtained therein. This is followed by the case setup of the main simulation suite and the results obtained therein.

5.1. Pre-cursor Simulations - Single Column Model (SCM)

While most of the literature perused in Chapter 2 focuses on flow over large wind farms, they often assume cyclic or periodic boundary conditions on the adjacent lateral faces (relative to the incoming flow) (infinite span-wise length) (Allaerts and Meyers, 2017, 2018, 2019, Lu and Porté-Agel, 2011) or all the lateral faces (infinite farm) (Abkar and Porté-Agel, 2013, 2014, Allaerts and Meyers, 2015). The present study considers a wind farm having a finite span-wise and stream-wise length.

To include the wind-farm entrance effects and the development of the boundary layer, most of the earlier works (Allaerts and Meyers (2017) and Munters et al. (2016)) employ a concurrent precursor method developed by Stevens et al. (2014). An alternative approach is to run a separate precursor simulation (Keck et al., 2014, Paul van der Laan and Sørensen, 2016, Paul van der Laan et al., 2015, Wu and Porté-Agel, 2013) and use the data as initial and boundary conditions for the main set of simulations containing the wind turbines. Since, the aforementioned studies assume horizontally *heterogeneous* conditions, the precursor simulations are run on a grid (without turbines) having similar physical dimensions as the main simulations.

However, in the present study, fully developed ABL profiles at the inlet are obtained by carrying out precursor URANS simulations using an SCM of the atmosphere. An SCM is one where the height of the domain is much higher compared to the grid dimensions in the stream-wise and span-wise directions. As the present study assumes horizontal homogenous conditions, the fully developed ABL profiles would be independent of the physical lengths of the domain in the stream-wise and span-wise directions (similar to the first benchmark study).

Single column URANS models can be used as a proxy to 3D models used in heterogeneous wind conditions. They provide an economically viable solution to test different ABL settings (Rodrigo et al., 2018). Previously, the single column model has been used to obtain vertical profiles of potential temperature, velocity and other flow variables in several studies (see Sanz Rodrigo et al. (2017), Rodrigo et al. (2018), Calaf et al. (2011)).

5.1.1. Case Setup - SCM

To set up flow simulations using the SCM, a grid of dimensions $20\ m \times 20\ m$ in the horizontal directions and $10\ km$ in the vertical direction is set up (equal to the vertical dimension of the grid containing turbines). Further, a latitude of $43.43°$ is assumed to represent the location of the wind farm. This value has been used previously in the studies carried out by Allaerts (2016), Allaerts and Meyers (2017), Gadde and Stevens (2019).

The initial values of each flow variable (U, k, ϵ) define the flow characteristics within the CNBL, and the vertical profile of θ defines the strength and base height of the capping inversion located above the CNBL. Low inversion base heights are common under offshore conditions (Allaerts and Meyers, 2015). For example, Brost et al. (1982) has shown capping inversion heights to be as low as $400\ m$. These heights are also reported by other measurement campaigns (Grant, 1986, NICHOLLS, 1985). Such low inversion layer heights have a strong influence on wind farm performance (Allaerts and Meyers, 2015). Therefore, in the present study, two inversion heights are considered viz. $500\ m$ and $1000\ m$ based on their common occurrence under offshore conditions (Allaerts and Meyers, 2015, Sorbjan, 1996).

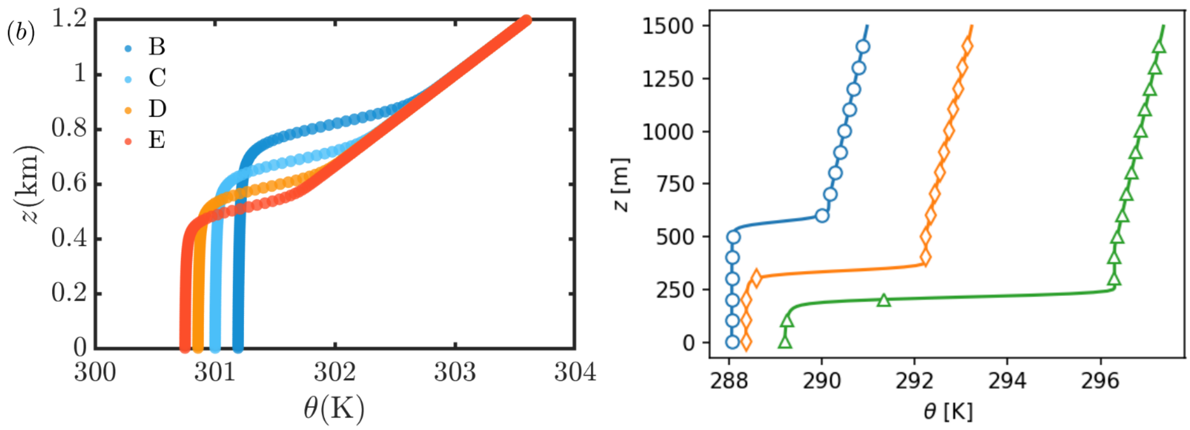

(a) Vertical profiles of θ for various test cases (Liu et al., 2021)

(b) Vertical profiles of θ for various test cases (Sood et al., 2020)

Figure 5.1: Vertical profiles of potential temperature for various cases as reported by Sood et al. (2020) and Liu et al. (2021)

Further, Hess (2004) had estimated the capping inversion strength and thicknesses of the marine stratocumulus experiments. They were in the range between $2.7\ K - 8.7\ K$ and $50\ m - 150\ m$ respectively (see Figure 5.3 for typical profile shapes obtained in (Liu et al., 2021, Sood et al., 2020)). In the present study, an average capping inversion thickness between the two values $(110m)$ and two values of the CIS $(2.5\ K$ and $10\ K)$ are considered. Further, the FALR of $1\ K/km$ and $10\ K/km$ are chosen. These are typical values as reported by Sorbjan (1996) and have been previously used by Allaerts and Meyers (2015), Allaerts (2016), Abkar and Porté-Agel (2013).

The computational setup (specifically the boundary conditions) of the SCM should represent a vertical column of the atmosphere under offshore conditions. To achieve the same, cyclic or periodic boundary conditions are applied on all lateral faces of the single column model. The single column model is initialized with a uniform geostrophic wind speed of $10\ m/s$ (in the positive X direction). The reference potential temperature is set to $T_0 = 290\ K$ which is also the temperature at the ground (similar to the first benchmark study). Further, the drag due to the ocean waves are modelled as an aerodynamic surface roughness length (z_0) set to $0.0002m$ (Allaerts, 2016, Sullivan et al., 1994). A horizontal pressure gradient forcing having a fixed value of $0.001Pa/m$ is applied within the domain in the span-wise direction.

Furthermore, the initial vertical profiles of potential temperature is implemented using a first-order model. The first-order model is better than its zero order counterpart, as it allows the definition of the capping inversion characteristics, such as its base height and strength and a finite thickness (see Figure 1.7). Observational studies and measurements have indicated that a first order jump model does not accurately define the potential temperature variation that is prevalent in the actual atmosphere. However, this can be used to describe the initial values of the precursor simulation. A smoothly varying vertical profile of θ akin to the case of Rampanelli and Zardi (2004) can be achieved in two ways.

The first method is to prescribe the initial vertical profile for θ with a first order model. This would inherently define the base height, thickness and strength of the Capping Inversion (CI), and the Free Atmosphere (FA) stratification. Further, the CFD simulations are advanced in time till a quasi-steady (equilibrium) state is developed. In this case, the user has complete control over the capping inversion height and strength. Another method, is to assume an initial linear variation of potential temperature (having the same magnitude as the FALR) with height and let the CNBL develop over time.

This is similar to the approach adapted in the first benchmark study. However, in this case, the user has no control on the Capping Inversion Height (CIH) and the Capping Inversion Strength(CIS). They are determined by the balance of the turbulent entrainment from the free atmosphere above and the capping inversion strength. The present study employs the former method to define the capping inversion characteristics.

Further, the *setFieldsABL* utility of SOWFA is used to set up the initial field values of the flow variables such as pressure, potential temperature,$\mathbf{U}$,k and ϵ within the domain [1]. The simulations are then advanced in time for 24 hours. After ≈ 20 hours, the values of all flow variables (U, θ, k, ϵ) attain a quasi-steady state. The field values of each flow variable is further averaged over the last hour and used as input (initial and boundary conditions) for the main simulation suite.

5.1.2. Results and Discussion - Single Column Model

The URANS simulations were found to be sensitive to the time step value considered, as it used the Pressure-Implicit with Splitting of Operators (PISO) algorithm for pressure velocity coupling. A small time step of $< 0.5\, s$ is considered in order to maintain the Courant number ($C < 0.5$) [2]. This ensures the stability of the transient simulations by ensuring that the system of equations remains diagonally dominant.

The results shown in Figure 5.2 depict the temporal evolution of planar averages [3] of each of the flow variables with height $U_{planar}, \theta, k, \epsilon$ over a period of 24 hours for Case 0 (CIS=$2.5K$; $CIH = 500m$; $FALR = 1K/km$). The plots show the temporal variation (after every 6 hours (21600 s)) of vertical profiles of planar averaged velocity ($\sqrt{u^2+v^2}$), horizontal flow direction, θ, k and ϵ.

From Figure 5.2a, it can be observed that the initial vertical profile (at $t = 0s$) of the planar averaged velocity is a uniform value of $10m/s$. The vertical profiles exhibit a transient behaviour over the first ≈ 20 hours, after which they become quasi steady. The shapes of the vertical profiles of planar averaged velocity are similar to the CNBL profiles shown in Sood et al. (2020) and Liu et al. (2021) (as shown in Figure 5.3).

Further, from Figure 5.2b, the change in the horizontal flow direction can be observed with time. A sharp change in the horizontal wind direction above and below the inversion can be observed. This is because above the inversion layer, the wind direction is a result of the Coriolis force and the applied pressure gradient forcing, and below the inversion, the Coriolis force is reduced due to the reduced wind speed. This causes the wind to turn into the direction of the applied pressure gradient forcing.

---

[1] The utility takes as input - the variation of the field values with height and distributes them throughout the cells within the domain depending on the height coordinate of the cell height specified in the input. The original *setFieldsABL* utility has been modified to accommodate k and ϵ profiles

[2] The Courant number is the dimensionless value which depicts the amount of time a particle stays in one cell of the mesh. Mathematically, it is calculated as $C = u\frac{\Delta t}{\Delta x}$

[3] average of all values in an XY slice at a particular height

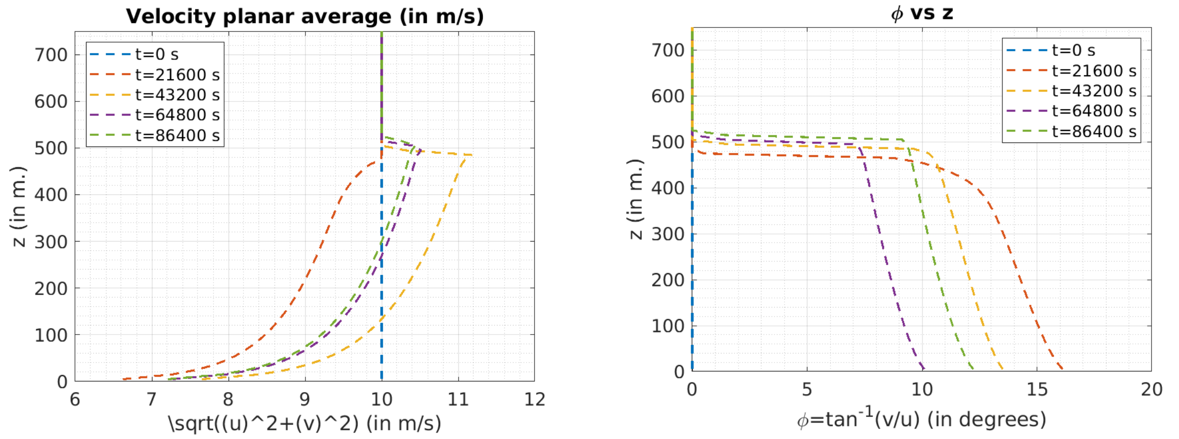

(a) Evolution of the planar velocity $\sqrt{u^2 + v^2}$ over 24 hours (b) Evolution of horizontal flow direction $tan^{-1}\frac{V}{U}$ profiles over 24 hours

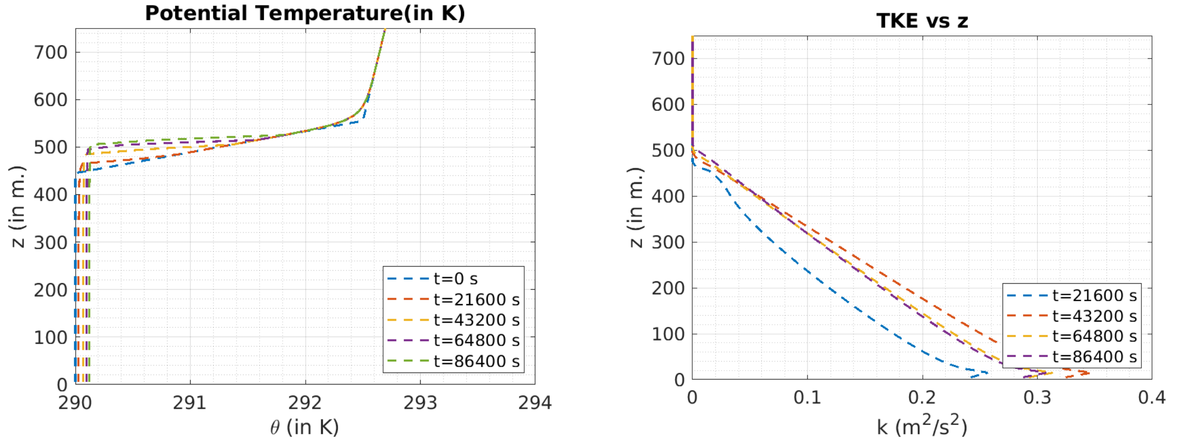

(c) Evolution of the θ over time (d) Evolution of the TKE profiles over 24 hours

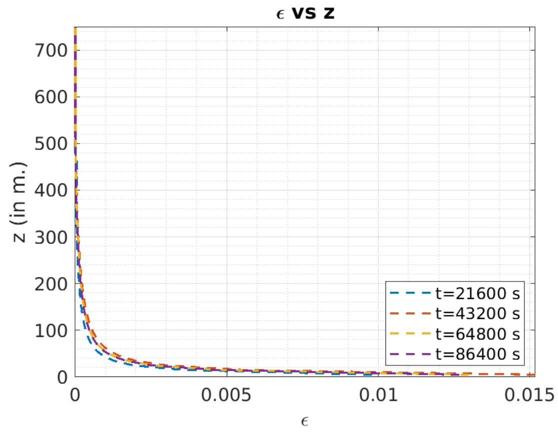

(e) Evolution of ϵ over 24 hours

Figure 5.2: Evolution of profiles of the flow variables over 24 hours for Case 0 (CIS=2.5K; CIH=500m; FALR=1K/km)

From Figure 5.2a, it can be observed that the initial vertical profile (at $t = 0s$) of the planar averaged velocity is a uniform value of $10m/s$. The vertical profiles exhibit a transient behaviour over the first ≈ 20 hours, after which they become quasi steady. The shapes of the vertical profiles of planar averaged velocity are similar to the CNBL profiles shown in Liu et al. (2021). Further, from Figure 5.2b, the change in the horizontal flow direction can be observed with time.

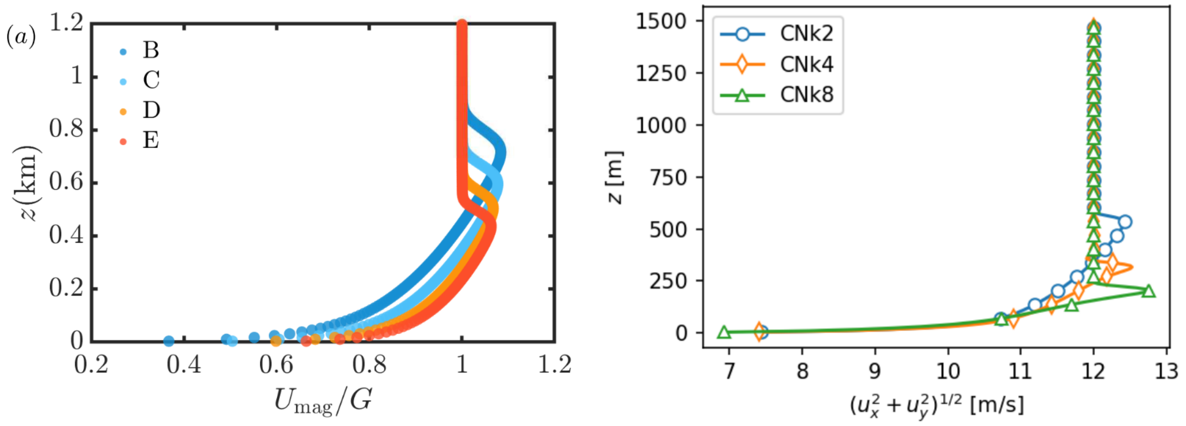

(a) Vertical profiles of $\sqrt{u^2 + v^2}$ for various test cases (Liu et al., 2021) (b) Vertical profiles of $\sqrt{u^2 + v^2}$ for various test cases (Sood et al., 2020)

Figure 5.3: Vertical profiles of planar velocity magnitude for various cases as reported by Sood et al. (2020) and Liu et al. (2021)

The sharp change in the direction of the wind above and below the inversion can be observed from here. This is because above the inversion layer, the wind direction is a result of the Coriolis force and the applied pressure gradient, and below the inversion, the Coriolis force is reduced due to the reduced wind speed. This causes the wind to turn to the direction of the applied pressure gradient.

Further, from Figure 5.2c, the temporal evolution of the vertical profiles of θ can be observed. The initial temperature profile shows a first-order temperature variation with altitude. Based on the initial temperature profile, it can be observed that warmer air is placed above the neutral boundary layer. Over time, the warm air from above is entrained in to the neutral surface layer below. This raises the temperature at the ground and eventually creates a smooth variation of temperature with altitude (similar to the analytical profiles obtained by (Rampanelli and Zardi, 2004)).

After ≈ 20 hours, further entrainment of warm air from the warm upper layers is balanced by the strength of the capping inversion. This is the quasi-steady state, where the growth of the CNBL is of the order of a few $mm/hour$. Similar quasi-steady behaviour is observed in the case of k and ϵ (see Figure 5.2d and Figure 5.2e respectively). Higher values of the two variables are observed at the ground level due to the presence of the ground itself, which negatively perturbs the flow. Similar graphs depicting the temporal behaviour of the relevant flow variables for the remaining cases (Cases 1 - 7) have been included in the appendix.

As the flow variables exhibit a quasi-steady behaviour, their values are averaged after 23 hours (82800 s). These averaged values are then used to set up the initial and boundary conditions for the main simulations. Since the horizontal flow direction (ϕ) at the hub height $\neq 0°$ (i.e., perpendicular to the actuator disk) (see Figure 5.2b, the entire vertical profile of ϕ needs to be rotated such that the flow remains perpendicular to the actuator disk at the hub height and the applied pressure gradient remains in the same direction with respect to the velocity components obtained in the quasi-steady solution.

5.2. Main Simulation suite

The wind farm considered in the present study contains twenty-five NREL 15MW research turbines, each having a hub height of $150\ m$ and a rotor diameter(D) of $240\ m$ (Gaertner et al., 2020). The turbines are modelled as actuator disks having the same disk diameter and placed at the same hub height as the actual turbine. The tower on which the nacelle rotor assembly is mounted is neglected in the present study.

Previously, Wu and Porté-Agel (2013) studied the flow around a wind farm having an aligned turbine layout with separation distances of 5D and 4D in the stream-wise and span-wise directions, respectively. Further, Chamorro and Porté-Agel (2011) simulated flow around an aligned turbine layout having 5D, 7D stream-wise turbine separation distances and 4D span-wise turbine separation distance. Furthermore, (Allaerts, 2016) considered a turbine separation distance of 7.5D and 5D in the stream and span-wise directions. Thus, in the present study, the turbines are laid out in an aligned manner having a stream-wise separation of $7D$ and a span-wise separation of, $4D$ as these are typical values of turbine separation distances that are chosen by other CFD studies.

5.2.1. Case setup

The wind farm layout and the Rayleigh damping layers are as shown in Figure 5.4. The case set up of the main domain containing the turbines (their ADM representations) is as shown in Figure 5.4 and Figure 5.5. The mesh is divided into two blocks. The bottom block extends $100\,m$ above the top of the prescribed inversion layer top height and has a resolution of $25\,m$ in all directions. Furthermore, the turbines and their wakes have a refined mesh resolution of $12\,m$. The top of the domain has a mesh resolution of $(100\,m, 200\,m, 25\,m - 100\,m)$ in the (X, Y, Z) directions.

A grid-independent study was attempted in the present case. However, a refinement of the grid in the block above the inversion layer led to a divergence in the simulations. The reason for the same is unknown and further research needs to be carried out to understand why this happens.

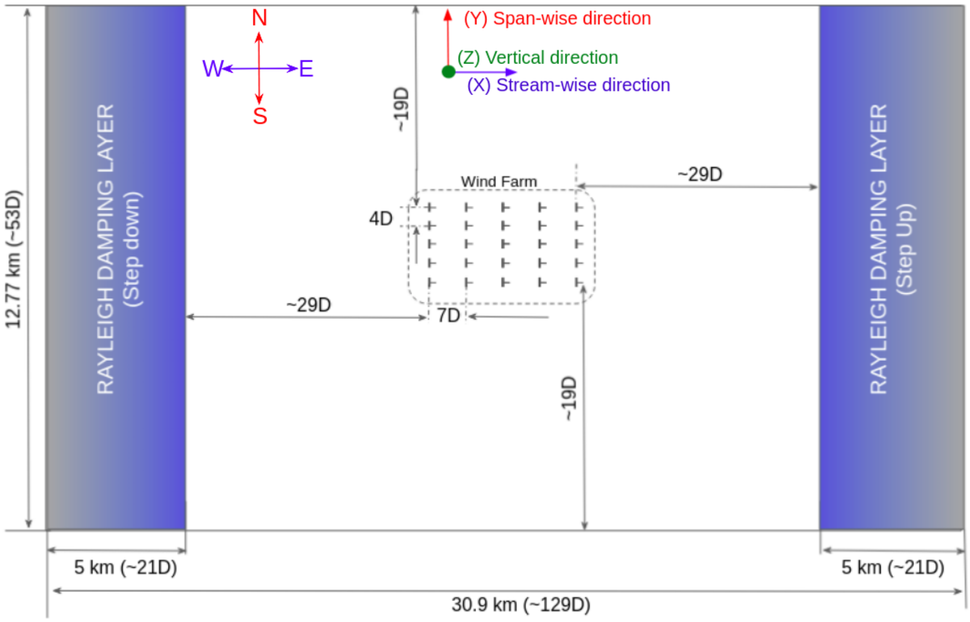

Figure 5.4: Planar view of the case setup being used in the current study (XY plane) (Top View)

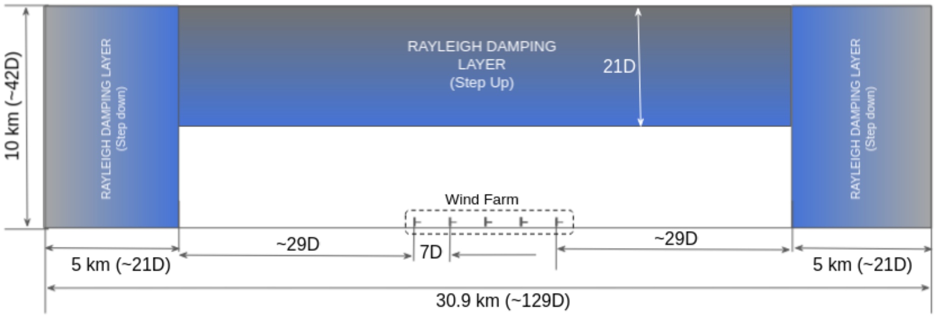

Figure 5.5: Planar view of the case setup taken along the middle column of turbines (XZ plane) (Side View)

Based on the literature perused in subsection 3.4.3, very little guidance is provided to determine the thickness and the value of the damping layer coefficient for the present problem. In the present study, based on the range of values suggested in the studies cited in subsection 3.4.3, the Rayleigh damping thickness were determined to be $5000\ m$ at the entrance, exit and the top of the domain with a common Rayleigh damping coefficient of $0.03s^{-1}$ through trial and error.

Further, unlike the earlier studies (Allaerts and Meyers, 2017, Hills and Durran, 2012, Klemp and Lilly, 1978) which assumed a uniformly increasing damping through the layer, the present study employs a step-up $(f = +1)$ or step down configuration $(f = -1)$. The difference between the step-up and step down configurations can be understood as an increase in the magnitude of forcing as one moves from the start to the end of the layer. Through a step-up configuration, the forcing increases from the beginning to the end, and the opposite is true for a step-down configuration.

At the inlet (upstream of the farm), the step-down configuration is used, as this region are expected to only contain weak AGW reflections from the top of the domain. However, the top of the domain and at the exit (downstream of the farm), would contain the AGWs excited by the wind farm and their reflections from the boundaries. There, in these two regions, the step-up configuration is implemented.

The initial and boundary values of all flow variables (viz. k, ϵ, θ) within the mesh are obtained as planar averaged values [4] from the single cell precursor simulation. Furthermore, the initial and boundary values of $\overline{\mathbf{U}}$ are specified by rotating the vertical profile of the horizontal flow direction by a requisite angle to obtain perpendicular flow at the actuator disk at the hub height. Also, the imposed pressure gradient is split into its components in the stream and span-wise directions in order to remain relatively similar in direction with respect to the rotated velocity profile.

The lateral faces were imposed with a cyclic or periodic boundary condition. Due to this, one may argue that the novelty of the present study, which considers flow over a wind farm of finite span-wise length, has been lost. However, since the sum total of distances on either side of the wind farm $> 1.5\times$ the span-wise farm length, there exists no lateral interaction between one farm and its periodic neighbour placed in the span-wise direction.

5.3. Results and Discussion

The wind, flowing into the farm, is decelerated by the wind turbines which extract energy from it. This forms a region of momentum deficit within the farm (as observed from Figure 5.6). To compensate for the reduced mass flow within the farm, (the continuity constraint) an upward flow deflection results upstream of the farm (as observed in Figure 5.8). This pushes the inversion layer upwards (see Figure 5.13), and causes an increase in the height of ABL.

Also, the upward flow deflection causes the lifting of cold air from below to a region of air having higher temperature (creating the anomaly referred to by Smith (2009)). The combination of temperature stratification and boundary layer displacement excites AGWs. The excited AGWs are of two types, viz. free AGWs in the Free Atmosphere above the inversion layer and the trapped waves that propagate along the density discontinuity (the inversion layer itself) similar to the prediction by Sachsperger et al. (2015).

The vertical wavelength (λ_z) of the triggered AGWs in the Free Atmosphere is given by the mathematical relation $\lambda_{vertical} = 2\pi U/N$ (Allaerts, 2016), where the Brunt–Väisälä frequency $N = \sqrt{\frac{g}{\theta_0}\frac{\partial\theta}{\partial z}}$. The FALR in the present case is $1\ K/km$. which results in $\lambda_z = 10.893\ km$. Since the vertical extent of the domain in to only $10\ km$, of which $5\ km$ is composed of the Rayleigh damping layer, only 50% of the free AGW can be observed. Further, the horizontal wavelength of the free AGWs in the free atmosphere is $\approx 42D$ (which is $\approx 1.5\times$ farm length).

---

[4] values averaged at each XY plane

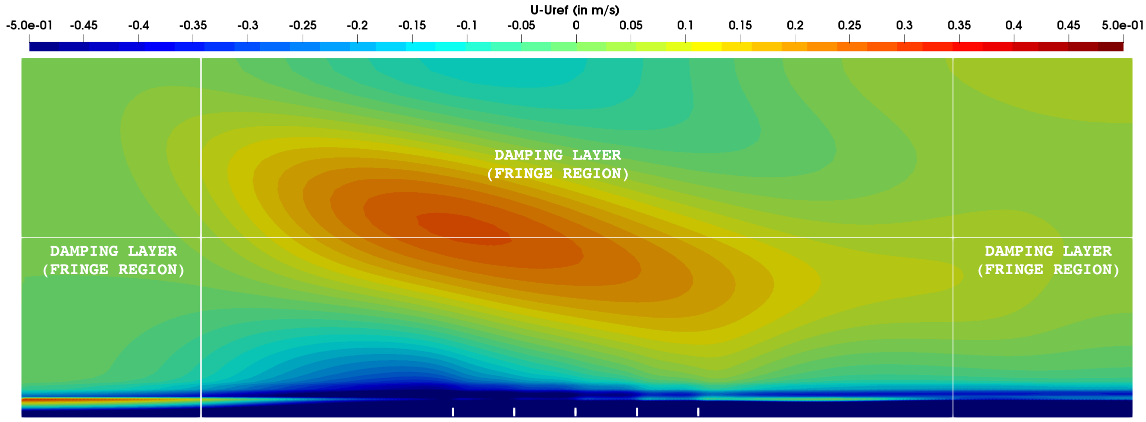

Figure 5.6: Contours of velocity deficit ($|\overline{U}| - U_{ref}$) (in m/s) taken on a XZ slice located at the central turbine column for Case 0 ($CIS = 2.5K; CIH = 500m; FALR = 1K/km$). The vertical and horizontal white lines spanning the domain dimension indicate the fringe regions. The small vertical white lines at the bottom of the domain indicate turbine positions.

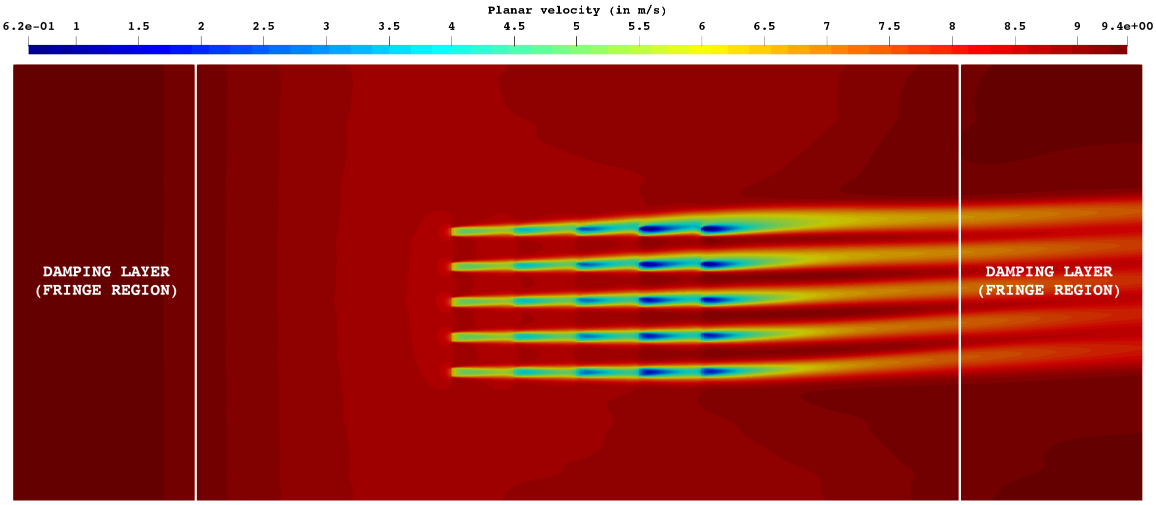

Figure 5.7: Contours of planar velocity ($\sqrt{u^2 + v^2}$ (in m/s)) taken on an XY slice at hub height for Case 0 ($CIS = 2.5K; CIH = 500m; FALR = 1K/km$)

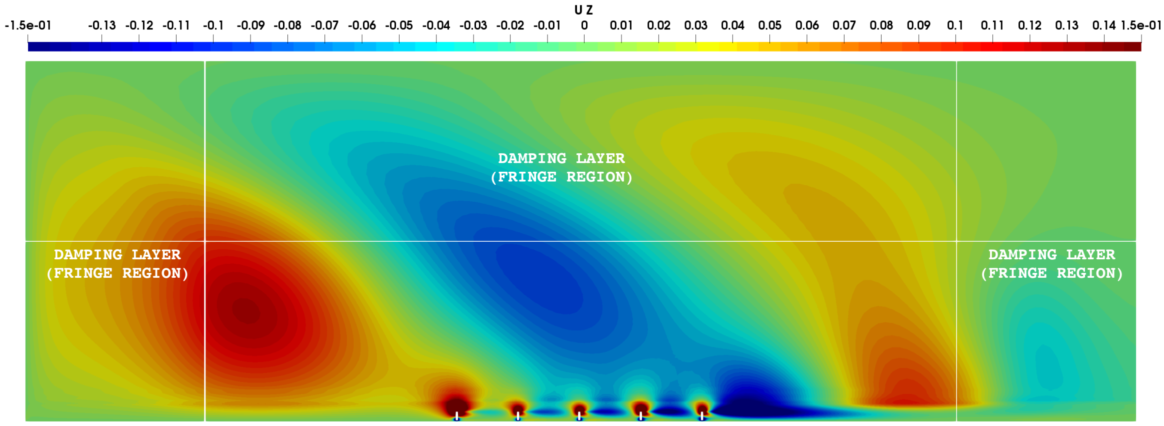

Figure 5.8: Vertical velocity contours (in m/s) for Case 0 ($CIS = 2.5K; CIH = 500m; FALR = 1K/km$) taken on a XZ slice located at the central turbine column. The vertical and horizontal white lines spanning the domain dimension indicate the fringe regions. The small vertical white lines at the bottom of the domain indicate turbine positions.

Furthermore, the low temperature anomaly (predicted by (Smith, 2009)) creates a region of high pressure upstream of the farm (see Figure 5.10). The adverse pressure gradient upstream of the farm decelerates the incoming flow (as seen in Figure 5.7) ahead of the farm, causing AGW induced wind farm blockage. Since the base of the inversion layer is at $445\ m$, the trapped waves propagating along the density discontinuity cause fluctuations in the vertical component of velocity at the hub height of the turbines (as observed in Figure 5.8). These fluctuations in vertical velocity assist in the wake recovery between consecutive turbines (observed as an increase in Figure 5.12a). The trapped AGWs also cause an increase in the velocity ahead of the third and fifth turbine rows. The velocity fluctuations, causing a local increase in power production at these two turbine rows (as seen in Figure 5.12b. Similar fluctuations were reported by (Allaerts, 2016, Smith, 2009).

As the farm considered in the present study has a finite span-wise length, the flow occurring around the wind farm needs to be studied. From Figure 5.11b, it can be seen that at each individual turbine, the incoming flow is deflected around the turbine (shown by the positive and negative horizontal flow angles in Figure 5.11b). At the level of the entire farm, the flow around the farm is shown by the positive horizontal flow direction north of the northern-most column (N2) and the negative flow direction south of the southernmost column (S2) (refer Figure 5.9).

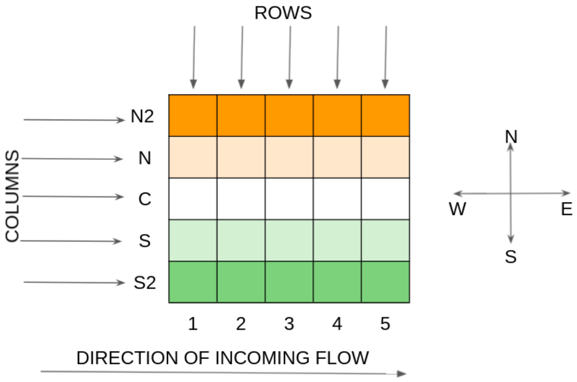

Figure 5.9: Notations used to refer to turbine rows/columns within the farm

The maximum change of flow direction is 4° on either side of the wind farm. Further, the change in the disk-averaged value of the horizontal flow direction of incoming wind along each column of turbines can be observed in Figure 5.11a. Also, from Figure 5.11a, it can be observed that the southernmost column (S2) shows a maximum flow deflection of $\approx 0.6^{\circ}$, while the maximum flow deflection is $\approx 5.1^{\circ}$ at the northernmost column (N2). These values of the change in wind direction at the turbine disks show an overall northerly deflection of the incoming wind direction. The wind direction at the hub height is affected by the applied pressure gradient, the flow around individual turbines, friction with the ground and the trapped waves propagating horizontally along the low hanging capping inversion. However, the effect of the Coriolis force on the wind direction at the hub height is minimal, as the flow is decelerated by the turbines.

The collective wake of the farm shows a northerly deflection of $\approx 5^{\circ}$ (as seen in Figure 5.11b), which is similar to the trends predicted by Paul van der Laan et al. (2015). Also, from Figure 5.10, it can be observed that in the lee of the farm, there exists a region of low pressure at the hub height of the turbines. This region of low pressure causes the flow to turn towards this favourable pressure gradient (the central turbine column) as seen in Figure 5.11a.

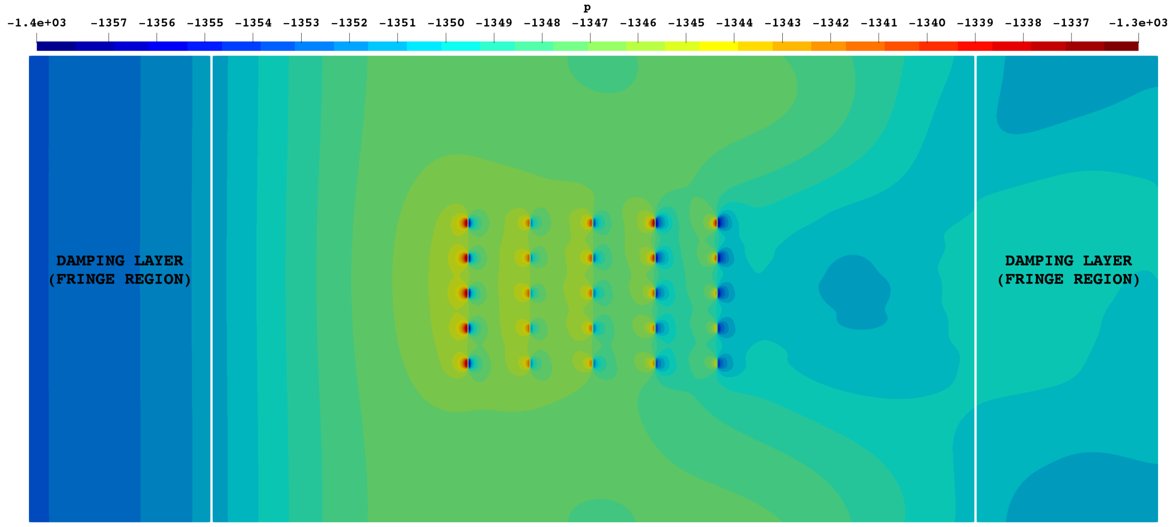

Figure 5.10: Contours of the pressure (relative to the $\mathrm{P}_{ambient})(in\mathrm{N/m}^2$) taken at the XY slice of the domain at hub height (Case 0 $(CIS = 2.5K; CIH = 500m; FALR = 1K/km)$)

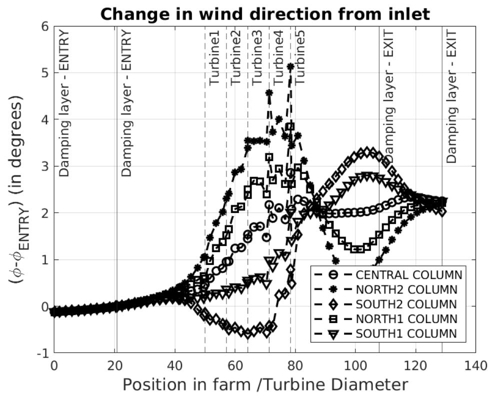

(a) Change in the direction of incoming velocity (disk averaged value) (Case 0 $(CIS = 2.5K; CIH = 500m; FALR = 1K/km)$) as compared its value the exit of Rayleigh damping layer placed at entry

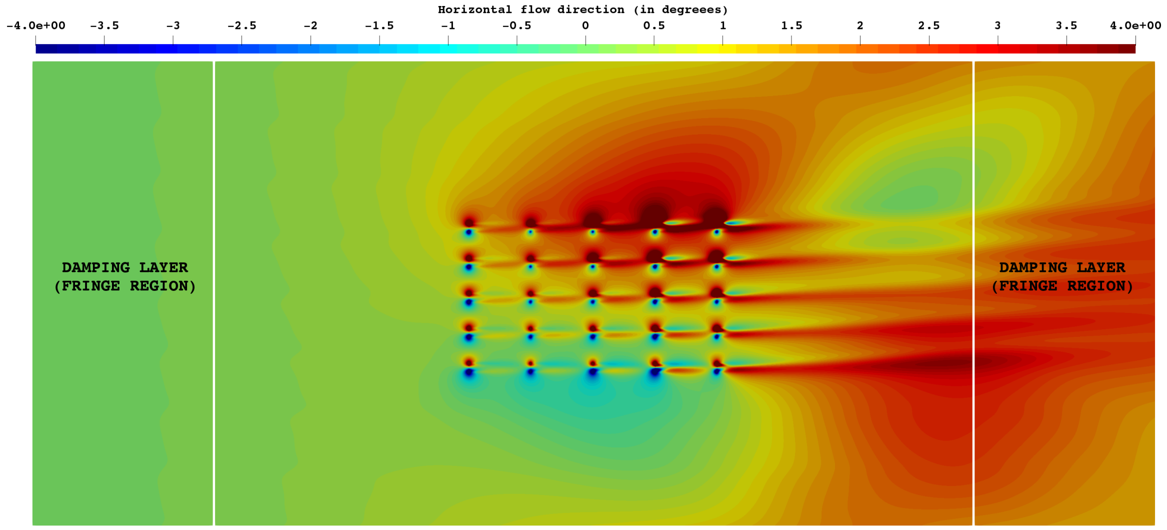

(b) Contours of horizontal flow direction (in degrees) taken at XY slice at hub height (Case 0 $(CIS = 2.5K; CIH = 500m; FALR = 1K/km)$)

Figure 5.11: Plots showing the change in the horizontal flow direction (from the inlet) and the horizontal flow direction at the hub height of the turbine(Case 0 $(CIS = 2.5K; CIH = 500m; FALR = 1K/km)$)

The resulting pressure distribution at the hub height is influenced by the vertically propagating AGWs in the free atmosphere and its horizontal counterparts propagating along the capping inversion. An AGW induced adverse pressure gradient is observed ahead of the wind farm, which causes flow deceleration (also referred to as AGW induced flow blockage). Further, the blockage is measured as the relative drop in incoming velocity with respect to the value at the exit of the damping layer placed at the inlet. From Figure 5.12a, it can be observed that the AGW induced blockage is $\approx 6\%$ at an upstream distance of, $\approx 10D$ respectively. This translates to a $\approx 5.8\%$ drop in the available incoming wind power.

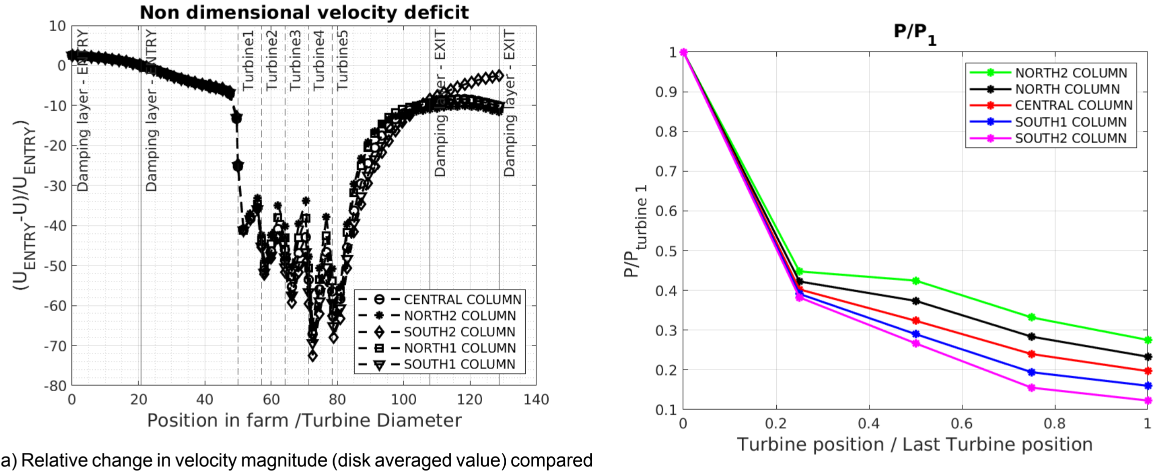

(a) Relative change in velocity magnitude (disk averaged value) compared to the inlet value (value at the exit of the fringe region placed at the inlet)

(b) Power down the line analysis P/P_1.

Figure 5.12: Relative drop in incoming velocity and power down the lines Case 0 ($CIS = 2.5K; CIH = 500m; FALR = 1K/km$)

From Figure 5.12b, it can be observed that a significant power drop $\approx 60\%$ from the first to the second row of turbines in each turbine column. Similar values were reported by (Allaerts, 2016). Also, (Stevens et al., 2014, Wu and Porté-Agel, 2013) had reported a similar trend of a large drop in power output between the first two turbine rows in aligned wind farm layouts. However, the highest reported value of $\approx 60\%$ is higher than the typical $\approx 40\%$ documented in literature.

Moreover, from Figure 5.12b, it can be observed that the highest drop in power output is in the southernmost (S2) column, while the opposite is true for the northernmost turbine column (N2). This can be attributed to the wake re-energization by the overall wind flow in the northern direction and the flow re-energization through the high-speed flow channels existing between turbines (see Figure 5.7).

Further, in the case of large wind farms, it is necessary to analyse the growth of the Internal Boundary Layer (IBL) which develops above the wind farm. The importance of the IBL was highlighted by Chamorro and Porté-Agel (2011). It is identified as the region where the flow is controlled by the incoming flow and the wind turbines. The height of the IBL is calculated similar to the work by Wu and Porté-Agel (2013), Allaerts (2016), where the IBL height is the height at which the ratio of the velocity magnitude of the converged RANS solution and the inflow velocity magnitude taken at the same height taken two kilometres upstream reaches a threshold of 97%.

From Figure 5.13, it can be observed that the base of the initial inversion layer gets lifted by the upward flow deflection ahead of the farm and also above the farm. Further, the IBL growth in all the turbine rows shows a different value for each turbine coli,m(shown by the coloured dotted lines). On an average, the southernmost column (S2) shows the lowest IBL height, while the northernmost column (N2) shows the highest IBL height. The heights are also affected by the flow of wind around the farm. The average of all the IBL heights taken along all 5 columns is shown by the black solid line in Figure 5.13.

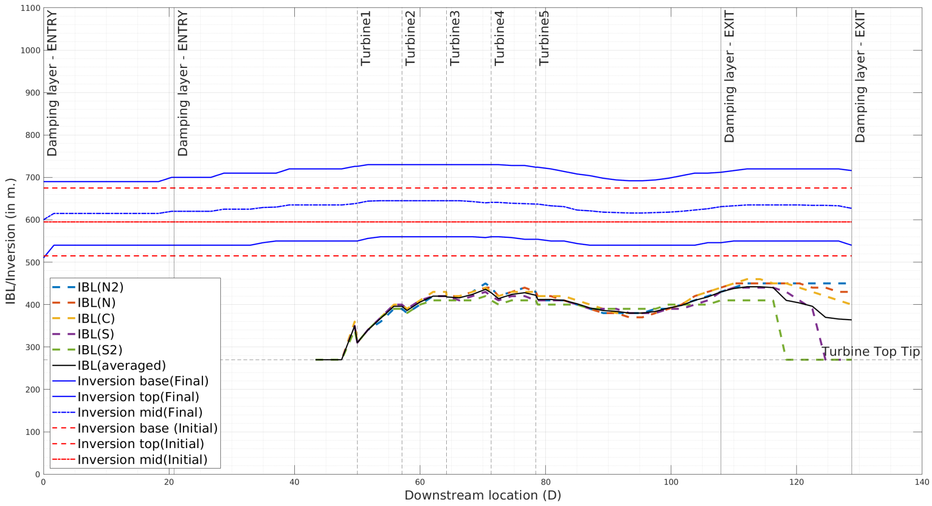

Figure 5.13: Growth of the IBL and lifting of the Inversion layer (Case 0 ($CIS = 2.5K; CIH = 500m; FALR = 1K/km$)). The vertical lines show the extent of the fringe layers at the entry, exit of the domain and the turbine positions

Unlike Allaerts and Meyers (2015), who reported a collision between the IBL and inversion layer heights for a shallow inversion base height of $300m$, in the present study, the IBL does not collide with the base of the inversion layer above. However, it can be observed that the IBL follows a similar trend as the inversion layer above, i.e., where the height of the IBL increases, the base of the inversion layer is pushed up and vice-versa. The presence of the turbines within the farm increases the height of the IBL. It is the highest between turbine rows 3 and 4. However, the IBL height beyond these rows shows a drop, as the flow accelerates near the last two rows due to the self-induced trapped AGWs. Thus, the IBL profiles are dependent upon the self-induced AGWs excited by the wind farm itself.

5.3.1. Impact of the Capping Inversion Strength (CIS)

The importance of the capping inversion and its role in enhancing or reducing the turbulence entrainment from the free atmosphere was discussed in section 1.4. Further, the impact of the same on wind farm flow was studied by, Allaerts and Meyers (2015) who showed that a higher capping inversion strength leads to a lower farm power output. The study mentioned that, the capping inversion prevents the entry of turbulent gusts from the free atmosphere into the turbine layer, and acts like a semi-rigid lid.

Further, Scorer (1949) used the internal AGW framework to develop a theory for lee waves in a two layer atmosphere. Furthermore, Sachsperger et al. (2015) had mentioned that trapped lee waves could develop if the structure of the atmosphere promotes vertical trapping and horizontal propagation of wave energy. This can occur when the Scorer parameter (l^2) [5] decreases with height or in the presence a density discontinuity (a capping inversion).

The horizontal wave propagation results from the linear superposition of two internal gravity wave modes viz. one is the upward propagating wave, excited by the flow over the topography and the other is a downward propagating wave arising from wave reflection at the interface of the two layers. In the present study, the capping inversion acts as a semi-rigid lid which serves as the interface between the surface layer below and the free atmosphere above.

Further, Sachsperger et al. (2015) had also summarized four wave types that could occur in common atmospheric conditions. Of these, the forced interfacial waves are observed in the present study. Forced interfacial waves are observed when the capping inversion has a neutral surface layer below and a stably stratified free atmosphere above (Sachsperger et al., 2015).

---

[5] $l^2 = \frac{N^2}{U^2} - \frac{1}{U}\frac{d^2U}{dz^2}$ where N is the buoyancy frequency and U is the incoming wind speed)

In the present case, the importance of the CIS is investigated by comparing Case 1 ($CIS = 2.5K, CIH = 500m, FALR = 10K/km$) and Case 5 ($CIS = 10K, CIH = 500m, FALR = 10K/km$). The two cases report a vertically propagating AGW in the free atmosphere, along with a trapped counterpart propagating along the density discontinuity (the capping inversion). Since the Free atmosphere is stratified (at 10 K/km) in Case 1, 5), it leads to the formation of trapped AGWs at the density discontinuity (the capping inversion itself) and the free atmosphere aloft. Further, the height of capping inversion base in both cases 1 and 5 are $500\ m$ (low capping inversion base height).

The density discontinuity is close to the topography exciting the AGWs (the wind farm) [6]. The effect of these trapped AGWs and its vertically propagating counterparts in the free atmosphere manifest as velocity fluctuations within the wind farm as observed in Figure 5.16. Figure 5.14a and Figure 5.14b show the contours of vertical velocity along the central turbine column. In both the figures, the small vertical white lines depict the position of the turbines. Further, the flow around the wind turbine disks can be observed from the positive and negative vertical velocity values.

Further, from Figure 5.14b, it can be observed that there are considerable velocity fluctuations propagating downstream of the farm as compared to Figure 5.14a. This is because of the stronger capping inversion in Case 5 vis-à-vis Case 1. The stronger capping inversion traps the AGWs excited by the wind farm, causing higher velocity fluctuation downstream of the same.

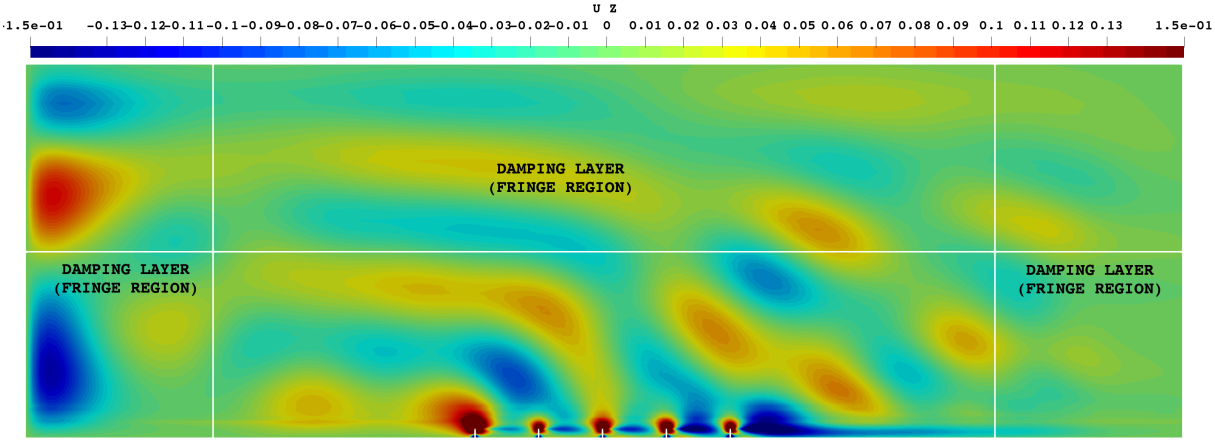

(a) Vertical velocity contours (in m/s) on an XZ slice of the domain passing through the central turbine column (Case 1 ($CIS = 2.5K, CIH = 500m, FALR = 10K/km$))

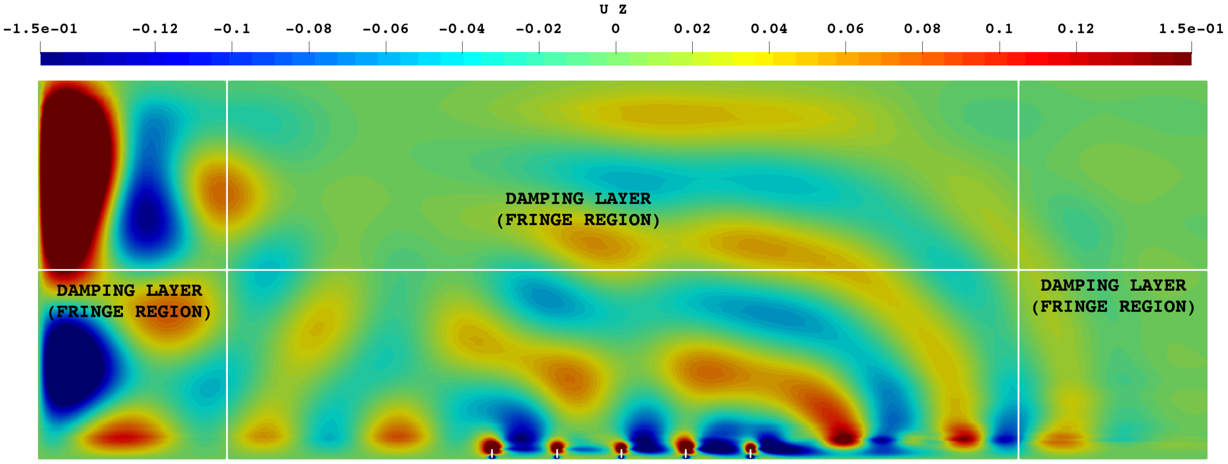

(b) Vertical velocity contours (in m/s) on the XZ slice of the domain passing through the central turbine column (Case 5 ($CIS = 10K, CIH = 500m, FALR = 10K/km$))

Figure 5.14: Contour plots of vertical velocity (in m/s) taken on an XZ slice (along the central turbine column) for Cases 1 and 5

Furthermore, in both cases, there are velocity fluctuations observed upstream of the farm. These

---

[6] a gap of $\approx 250m$ exists between the top of the turbine and the base of the inversion layer above

velocity fluctuations are an effect of the sub-critical flow ($Fr < 1$) and spurious AGWs reflections from the domain boundaries.

The Froude number (Fr) is calculated as ($Fr = \frac{\overline{U}}{g'L}$) (Allaerts, 2016), where $\overline{U}$ is the bulk velocity of fluid in the free atmosphere at the exit of the fringe region placed at the inlet, $g' = \frac{g\Delta\theta}{\theta_0}$ and L is the height of the ABL (taken as the centre of the inversion layer in the present study) of the incoming flow in Case 5 is lesser than unity. Upon substituting values of the flow velocity in the free atmosphere $\overline{U} = 10m/s$, $\Delta\theta$ as $2.5K$ and $10K$ for Case 1 and Case 5 respectively, $\theta_0 = 290K$ and $H = 540m$ yields Froude numbers of 1.5 and 0.7 for Cases 1 and 5 respectively. Thus, the incoming flow is super-critical in Case 1 and sub critical in Case 5.

Further, in the case of a sub-critical flow (Case 5), the effect of the waves propagate upstream (Allaerts and Meyers, 2019, Smith, 2009) as velocity fluctuations in the vertical direction (as observed in Figure 5.14b. Furthermore, in the super-critical case (Case 1), the impact of the AGWs are observed downstream of the exciting topography. Thus, the upstream velocity fluctuations in Case 1 can be attributed solely to the spurious AGW reflections from the domain boundaries.

Also, the excited AGWs (the vertically propagating wave and its horizontally propagating counterpart) create pressure fluctuations at the hub height of the turbines (shown in Figure 5.15a and Figure 5.15b). However, for Case 5 (the stronger capping inversion and sub-critical flow), the effect of the AGWs propagate upstream, creating alternating regions of increased and reduced pressure ahead of the wind farm.

Furthermore, in the lee of the farm, the horizontally propagating trapped AGWs are observed that have a wavelength of ≈ $21D$ (which is almost $3/5\times$ the farm length in the stream-wise direction). In Figure 5.15a (Case 1 - weaker capping inversion and super-critical flow), it can be observed that the adverse pressure gradient ahead of the farm is not as widespread as compared to Case 5. Further, the impact of these pressure fluctuations manifest as velocity and power fluctuations at individual turbines and also change the horizontal flow direction in and around the farm.

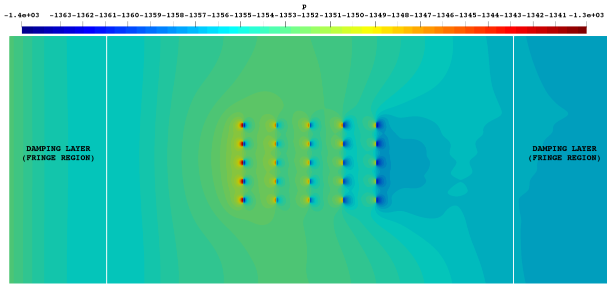

(a) Pressure contours (relative to the $P_{ambient}$) (in N/m^2) taken on an XY slice at the hub height of $150m$ (Case 1 ($CIS = 2.5K, CIH = 500m, FALR = 10K/km$))

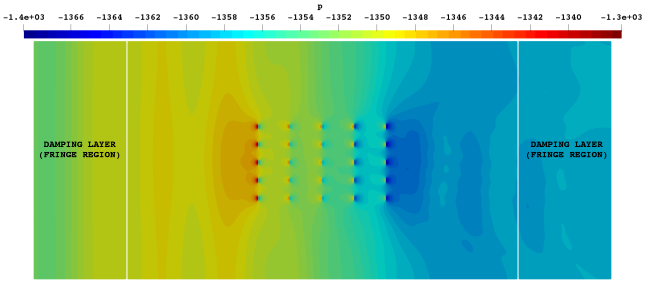

(b) Pressure contours (relative to the $P_{ambient}$) (in N/m^2) taken on an XY slice at the hub height of $150m$ (Case 5 ($CIS = 10K, CIH = 500m, FALR = 10K/km$))

Figure 5.15: Contour plots of pressure (relative to the $P_{ambient}$)(in N/m^2) taken along an XY slice (taken at the hub height of the turbines) for Cases 1 and 5

The excited AGWs cause a velocity reduction ahead of the wind farm and also cause velocity fluctuations within the farm as observed in Figure 5.14a. Further, from Figure 5.14a, it can be observed that within the farm, an overall higher velocity deficit is observed in the case of weaker inversion strength (Case 1) as compared to the stronger capping inversion (Case 5). The stronger capping inversion traps the AGWs created by the farm, which causes velocity fluctuations between turbine rows that reduces the velocity deficit between the same.

Ahead of the wind farm, for Case 1, AGW induced flow blockage can be observed as the relative drop in incoming flow velocity. A drop of $\approx 5\%$ is observed in incoming velocity at $\approx 10D$, upstream of the first turbine row. This translates into $\approx 15\%$ lower incoming wind energy at the first turbine row. However, in case 5, where the flow is sub critical, the trapped AGWs propagate upstream, which cause pressure and velocity fluctuations that in turn affect the AGW induced blockage. A marginally lower amount of blockage is observed in the case of a stronger capping inversion.

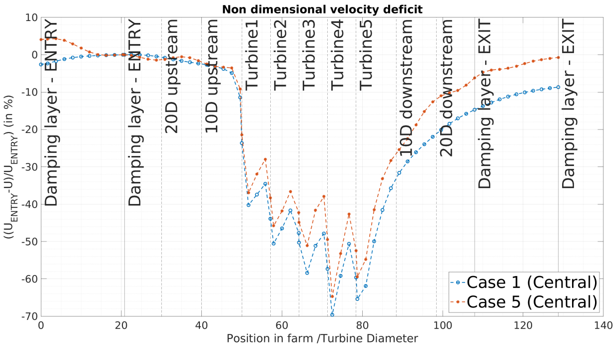

Figure 5.16: Relative change in velocity (disk averaged value) with respect to the value at the inlet (Central Column) for Cases 1 and 5

Further, Figure 5.17a and Figure 5.17b show the wake velocity deficit on an XY plane taken at the hub height of the turbines. The wake velocity deficit is taken as the relative change in the velocity magnitude at a given span-wise location with respect to its value at the same span-wise location at the exit of the fringe region placed at the inlet. For the case with the higher capping inversion strength (Case 5), a lower value of wake velocity deficit can be observed at each turbine column at the two downstream distances of $10D$ and $20D$. This implies a faster wake recovery in Case 5 as compared to Case 1. In the case of a stronger capping inversion, the trapped lee waves cause large scale velocity fluctuations in that region, that cause an earlier/ faster wake recovery.

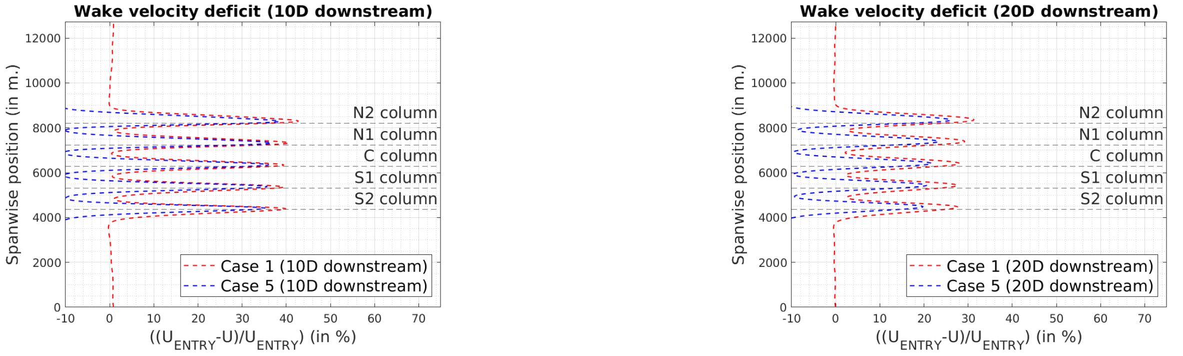

(a) Wake velocity deficit at 10D downstream of the last turbine row (Case 1 ($CIS = 2.5K, CIH = 500m, FALR = 10K/km$)) and (Case 5 ($CIS = 10K, CIH = 500m, FALR = 10K/km$))

(b) Wake velocity deficit at 20D downstream of the last turbine row (Case 1 ($CIS = 2.5K, CIH = 500m, FALR = 10K/km$)) and (Case 5 ($CIS = 10K, CIH = 500m, FALR = 10K/km$))

Figure 5.17: Wake velocity deficit (in %) taken on an XY slice at the hub height of the turbines for Case 1 ($CIS = 2.5K; CIH = 500m; FALR = 10K/km$) and Case 5 ($CIS = 10K; CIH = 500m; FALR = 10K/km$)

The pressure fluctuations at the hub height of the turbines alter the flow direction in this plane. From Figure 5.18a, it can be observed that the maximum direction change of the incoming flow is at the N2 and S2 columns. However, in the lee of the farm, the region of low pressure behind the last turbine row (Figure 5.15a) causes the flow emanating from N2 and S2 columns to turn back towards the central turbine column.

However, in Case 5, in the wake of the wind farm the alternating regions of increased and decreased pressure (see Figure 5.15b) cause the flow to be continuously changing direction in the lee of the farm. These fluctuations in the horizontal flow direction are observed even in the far wake of the farm (see Figure 5.18b).

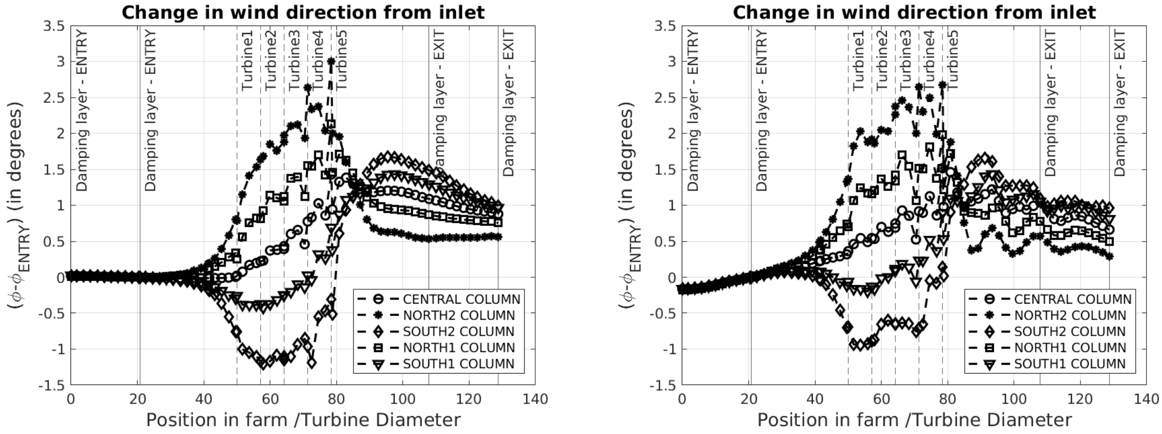

(a) Change in the horizontal flow direction (in degrees) (Case 1 ($CIS = 2.5K, CIH = 500m, FALR = 10K/km$))

(b) Change in the horizontal flow direction (in degrees) (Case 5 ($CIS = 10K, CIH = 500m, FALR = 10K/km$))

Figure 5.18: Change in the horizontal flow direction (in degrees) (disk averaged value) for Case 1 ($CIS = 2.5K; CIH = 500m; FALR = 10K/km$) and Case 5 ($CIS = 10K; CIH = 500m; FALR = 10K/km$)

Furthermore, from Figure 5.19, it can be observed that the power down the line curves follow similar trends of the velocity. The overall drop in power output is the highest between the first and second turbine rows. However, the drop is higher for Case 1 ($\approx 60\%$) as compared to Case 5 ($\approx 40\%$). Further, in both cases, there is a local increase in power between the second and third turbine rows. Similar fluctuations were also observed between the last two turbine rows. This local increase in power can be attributed to AGW activity and also to the re-energization of the flow within the farm wakes by the unperturbed flow occurring around the farm. However, a detailed energy budget analysis would be needed to understand the same which is beyond the scope of the present thesis work.

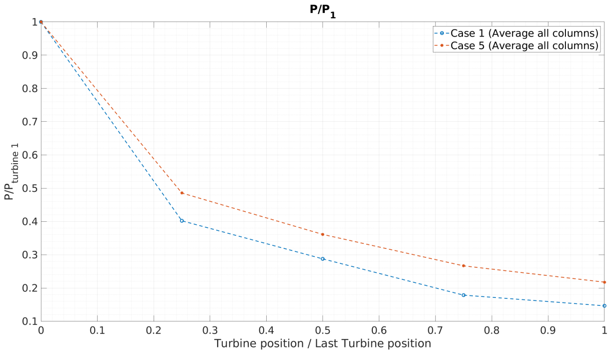

Figure 5.19: Power down the line analysis for Case 1 ($CIS = 2.5K; CIH = 500m; FALR = 10K/km$) and Case 5 ($CIS = 10K; CIH = 500m; FALR = 10K/km$) (average of all columns)

5.3.2. Impact of the Capping Inversion Height (CIH)

Sachsperger et al. (2015) who had used a linear 2D model and uniform incoming wind velocity, had mentioned that the forced interface waves propagating along the capping inversion were subject to forcing from the internal waves above. Further, the study had calculated a $\Delta\theta_{critical}$ and $h_{1critical}$, that were critical values of the capping inversion strength and base height, which determined whether the inversion was low and strong enough to cause wave trapping.

Furthermore, Allaerts and Meyers (2017) had observed that for low capping inversion heights, the capping inversion base interacted with the IBL below and also the wind farm induced AGWs caused formation of favourable and unfavourable pressure gradients in and around the farm which significantly impacted the power output of the same. Also, the study had concluded that higher CI base heights lead to higher wind farm power output.

Two values of capping inversion height were considered in the present study, viz. $500m$ and $1000m$ [7]. To understand the impact of the capping inversion height on self-induced AGWs from wind farms, results from Case 1 ($CIS = 2.5K; CIH = 500m; FALR = 10K/km$) and Case 3 ($CIS = 2.5K; CIH = 1000m; FALR = 10K/km$) are compared.

From Figure 5.14a and Figure 5.20, it can be observed that the AGWs excitation in Case 3 is lower than Case 1. This is observed in the wave fronts of the AGW's propagating vertically upwards in the free atmosphere. It can be observed that in Case 1, the wave fronts in the vertical direction become evanescent at a lower altitude as compared to Case 3.

The reasoning for the same is that, the upward flow deflection upstream of the farm (responsible for AGW excitation) encounters the capping inversion (the semi-rigid lid) at a higher altitude in Case 3 as compared to Case 1. Thus, in Case 3, the upward flow deflection (which causes the AGW excitation), is attenuated before lifting the inversion, which leads to a weaker excitation of AGWs in the Free Atmosphere. Further, a higher capping inversion height reduces the plausibility of wave trapping within the capping inversion.

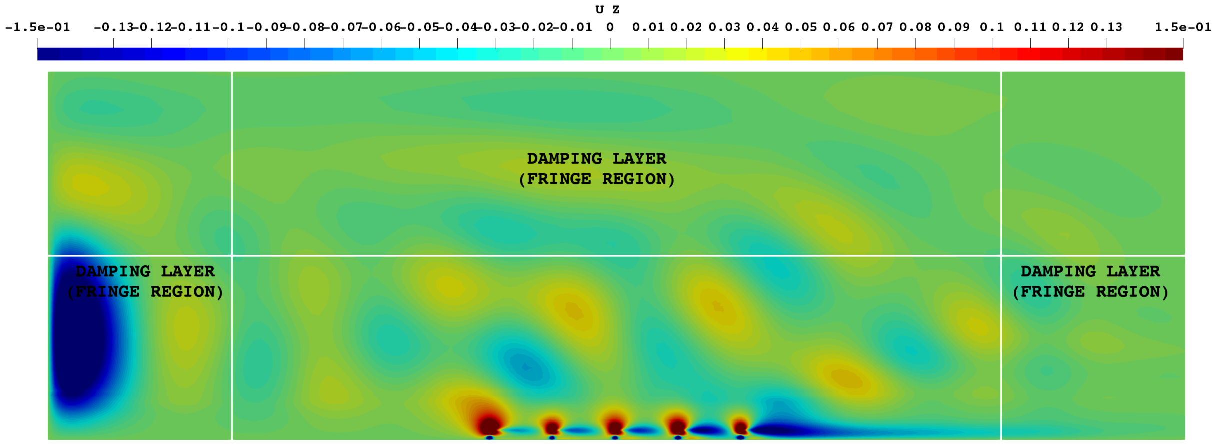

Figure 5.20: Contours of vertical velocity taken along an XZ slice passing through the central turbine column (Case 3($CIS = 2.5K; CIH = 1000m; FALR = 10K/km$))

Further, Figure 5.21a and Figure 5.21b show the relative change in the horizontal flow directions for Cases 1 and 3 respectively. It can be observed that, for a lower Capping inversion height (Case 1), the change in the horizontal flow direction (with respect to the incoming flow) in each turbine column is higher than Case 3.

Unlike a wind farm of infinite span-wise length, where the maximum wind deviation is dependent on the imposed pressure gradient and flow deceleration in the proximity of turbines, the present study shows

---

[7] The author considers the height of the capping inversion as the average height of the top and bottom of the CI. Thickness of the CI is assumed to be $110\ m$ in the present study.

that the flow around the wind farm has a non-negligible impact on the flow direction at the hub height of turbines.

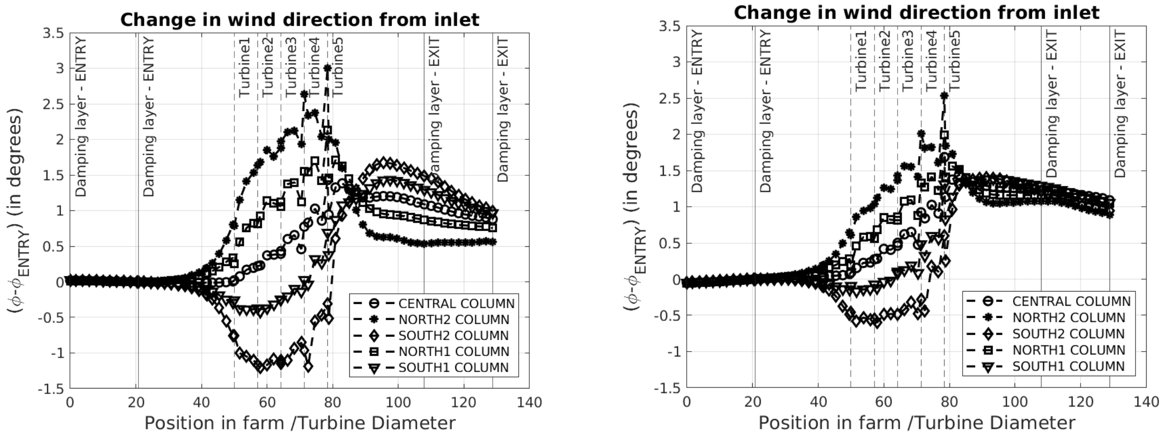

(a) Change in horizontal wind direction ($tan^{-1}(v/u)$) (Case 1 ($CIS = 2.5K; CIH = 500m; FALR = 10K/km$))

(b) Change in horizontal wind direction ($tan^{-1}(v/u)$)(Case 3 ($CIS = 2.5K; CIH = 1000m; FALR = 10K/km$))

Figure 5.21: Plots showing the change in the disk averaged values of the horizontal flow direction with respect to its value at the exit of the fringe region placed at the inlet (disk average for Case 1 and Case 3

From Figure 5.22a and Figure 5.22b, it can be observed that for a higher placed capping inversion (Case 3), the weak AGW excitation by the wind farm cause weaker pressure fluctuations at the hub height of the turbine. From Figure 5.22b, it can be observed that there are no visible AGW induced pressure fluctuations at the hub height.

The lower amount of pressure fluctuations manifest as smaller changes in the incoming wind direction, velocity deficits and power fluctuations. From Figure 5.22a, it can be observed that in the wake of the farm, a region of low pressure is formed, which causes a higher amount of inward flow deflection (to the farm center) in Case 1 as compared to Case 3.

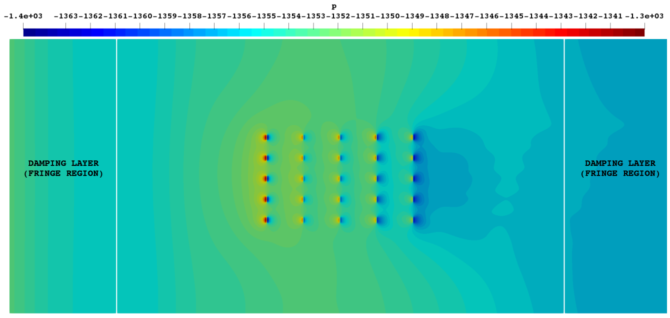

(a) Pressure contours (relative to the $P_{ambient}$) (in N/m^2) taken on an XY slice at the hub height of $150m$ (Case 1: $CIS = 2.5K; CIH = 500m; FALR = 10K/km$)

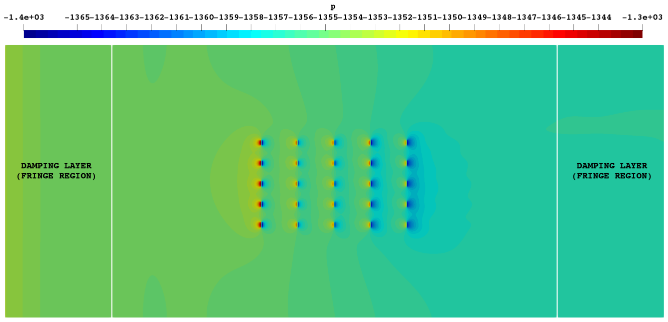

(b) Pressure contours (relative to the $P_{ambient}$) (in N/m^2) taken on an XY slice at the hub height of $150m$ (Case 3: $(CIS = 2.5K; CIH = 1000m; FALR = 10K/km)$

Figure 5.22: Contours of pressure (relative to the $P_{ambient}$) (in N/m^2) taken at the hub height for Cases1, 3

From Figure 5.23, it can be observed that a higher capping inversion height (Case 3) reduces the amount of blockage ahead of the farm. This reduces the amount of blockage related power losses. Further, from Figure 5.23, it can also be observed that the overall velocity in Case 3 is higher than Case 1, which results in higher power output in Case 3 as opposed to Case 1.

However, in Case 3, the blockage ahead of the wind farm is significantly higher than Case 1 ($\approx 3\%$ at a distance of $10D$ upstream of the farm). This translates to a $\approx 8.7\%$ drop in incoming power. These observations predict a similar trend of Allaerts and Meyers (2017), who had also predicted that the case with a higher capping inversion base height had a higher power output.

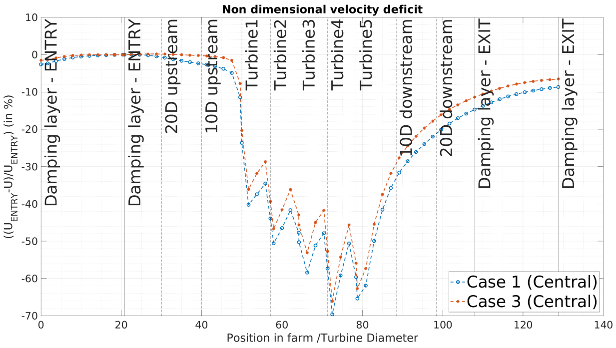

Figure 5.23: Relative velocity magnitude deficit (disk averaged value) (Central Column)(Case 1, Case 3)

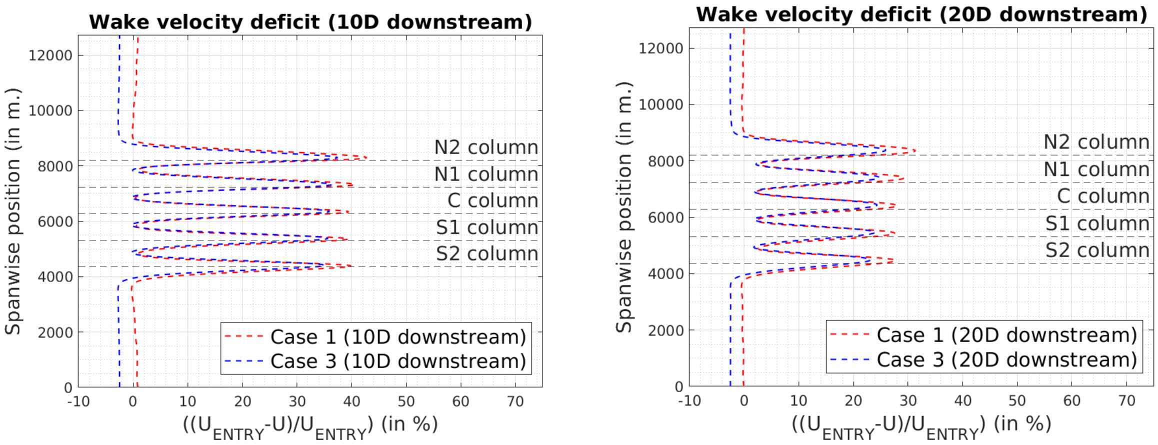

(a) Wake velocity deficit at 10D downstream of the last turbine row (Case 1 ($CIS = 2.5K, CIH = 500m, FALR = 10K/km$)) and (Case 3 ($CIS = 2.5K; CIH = 1000m; FALR = 10K/km$))

(b) Wake velocity deficit at 20D downstream of the last turbine row (Case 1 ($CIS = 2.5K, CIH = 500m, FALR = 10K/km$)) and (Case 3 ($CIS = 2.5K; CIH = 1000m; FALR = 10K/km$))

Figure 5.24: Plots showing the wake velocity deficit behind all the turbine rows (Cases 1 and 3)

Further, Figure 5.24a and Figure 5.24b show the wake velocity deficit behind the last turbine row. It can be observed, that, for a higher capping inversion height (Case 3), the magnitude of the wake velocity deficit is lower than that in Case 1, which indicates a faster wake recovery. Thus, it can be concluded that the wake recovery is faster for a higher placed capping inversion.

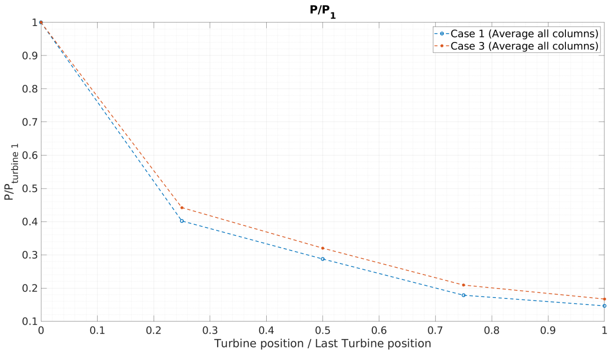

Figure 5.25: Power down the line analysis (average of all columns)(Case 1, Case 3)

Furthermore, from Figure 5.25, it can be observed that the highest drop in power occurs between the first two turbine rows, $\approx 55\%$. However, downstream of the same, the power gradually decreases in all rows. In both cases, one can observe that the power drop between the fourth and fifth turbine row is lesser than its predecessor. This is due to higher AGW induced pressure fluctuations at the hub height in Case 1 which causes the flow to accelerate and turn towards the central column, thereby causing a local increase in power output.

5.3.3. Impact of the Free Atmosphere Lapse Rate (FALR)

Previously, Sachsperger et al. (2015), Vosper (2004) had concluded that the possible range of lee wavelengths was limited by the stratification in the free atmosphere. Also, the study had predicted that the wavelength of the interfacial disturbances decreases with an increase in the stratification in the upper layer. Further, Abkar and Porté-Agel (2013) reported that the case with a higher FALR reports a lower power output as compared to its lower counterpart.

Also, Wu and Porté-Agel (2017) had considered two magnitudes of the FALR in their study. They reported that for a weaker free atmosphere stratification, the flow in and above the wind farm never reached the fully developed regime. They reported that, under a stronger free atmosphere stratification, the vertical deflection of flow triggered standing AGWs which cause blockage ahead of the farm.

In the present study, the impact of FALR upon the characteristics of the excited AGWs is studied by comparing results obtained from Case 0 ($CIS = 2.5K; CIH = 500m; FALR = 1K/km$) and Case 1 ($CIS = 2.5K; CIH = 500m; FALR = 10K/km$). From Figure 5.26a and Figure 5.26b, it can be observed that the vertical wavelength of the AGWs propagating in the free atmosphere changes with the FALR. A shorter vertical wavelength ($\lambda_z \approx 3.4km$) is observed for a higher FALR ($10K/km$) (represented by Case1) as compared to Case0 ($\lambda_z \approx 10.8km$) (see Figure 5.26).

Further, since the Froude number in both cases is greater than unity, the flow is super critical and this allows the waves to convect along the flow direction. Furthermore, the excited AGWs in the free atmosphere, cause pressure fluctuations at the hub height of the domain, which leads to flow deceleration or acceleration depending on the location within the farm.

From Figure 5.27a and Figure 5.27b, it can be observed that in both the cases, a region of high pressure is created ahead of the farm (due to flow deceleration). In Case 0 (weaker FALR), the pressure gradient is stronger and limited to a smaller upstream distance as compared to Case 1. Further, towards the last two turbine rows, the pressure gradient becomes favourable, which could lead to a flow acceleration within this region and upstream of the same.

The stronger and shorter adverse pressure gradient, in Case 0, causes a higher amount of blockage than Case 1 (see Figure 5.28) ($\approx 6\%$ (velocity deficit) in Case 0 and $\approx 2.5\%$ (velocity deficit) for Case 1 at $10D$ upstream of the farm). These velocity deficits translate $\approx 17\%$ and $\approx 7.3\%$ deficits in the incoming wind energy at the aforementioned distances. Also, in case 0, at turbine rows 4 and 5, it can be observed that the velocity deficit between the said rows is lower than Case 1 which is indicative of a faster wake recovery due to the presence of a favourable pressure gradient imposed by the AGWs.

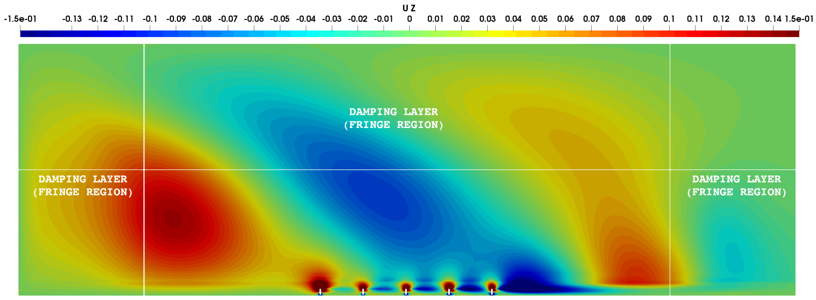

(a) Vertical velocity contours (in m/s) on the XZ slice of the domain passing through the central turbine column (Case 0 ($CIS = 2.5K; CIH = 500m; FALR = 1K/km$))

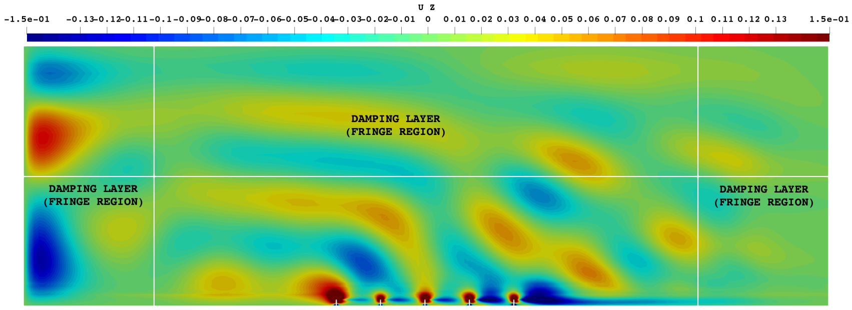

(b) Vertical velocity contours (in m/s) taken on an XZ slice of the domain passing through the central turbine column (Case 1 ($CIS = 2.5K; CIH = 500m; FALR = 10K/km$)

Figure 5.26: Contour plots of vertical velocity (in m/s) taken along the XZ slice (along the central turbine column) for Cases 0 and 1

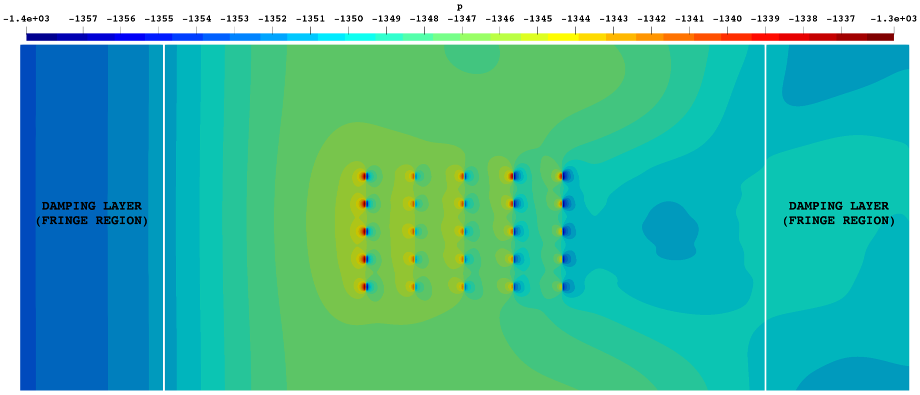

(a) Contours of pressure (relative to the $P_{ambient}$) (in N/m^2) taken on an XY slice located at the hub height of the domain (Case 0 ($CIS = 2.5K; CIH = 500m; FALR = 1K/km$))

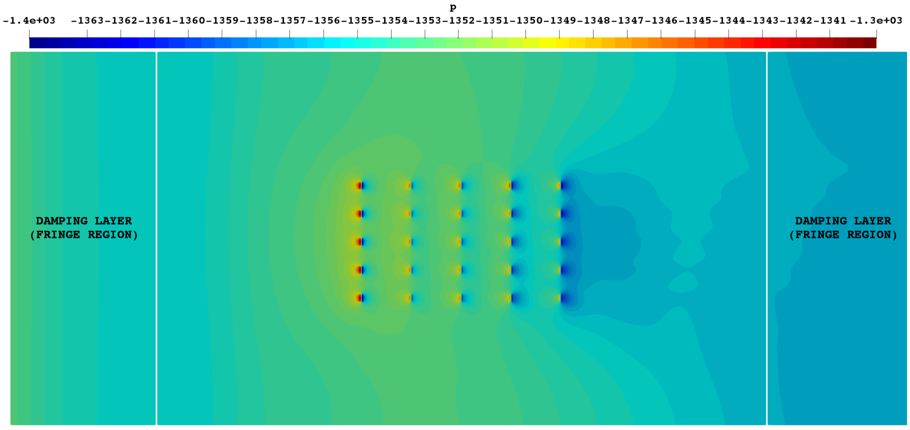

(b) Contours of pressure (relative to the $P_{ambient}$) (in N/m^2) taken on an XY slice located at the hub height of the domain (Case 1 ($CIS = 2.5K; CIH = 500m; FALR = 10K/km$))

Figure 5.27: Contours of pressure (relative to the $P_{ambient}$) (in N/m^2) taken on an XY slice located at the hub height (Cases 0 and 1)

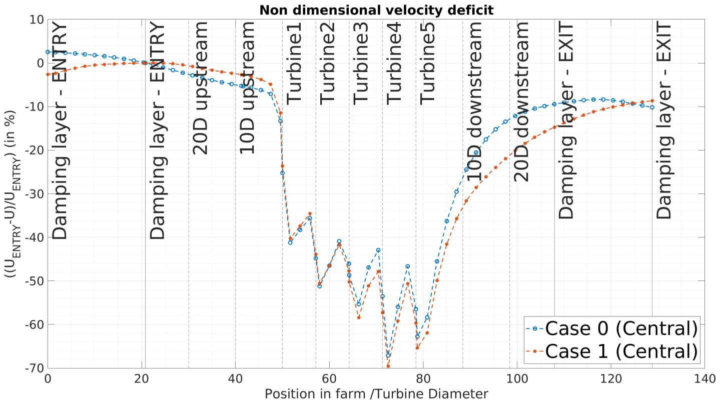

Figure 5.28: Relative velocity drop (disk averaged value) (Central column) for Case 0 ($CIS = 2.5K; CIH = 500m; FALR = 1K/km$) and Case 1 ($CIS = 2.5K; CIH = 500m; FALR = 10K/km$)

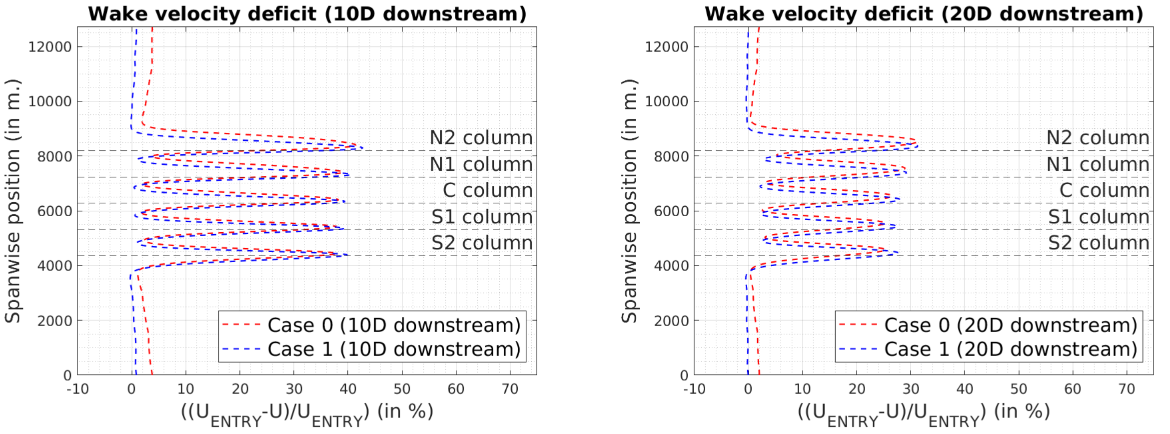

(a) Wake velocity deficit at 10D downstream of the last turbine row (Case 0 ($CIS = 2.5K; CIH = 500m; FALR = 1K/km$) and Case 1 ($CIS = 2.5K, CIH = 500m, FALR = 10K/km$))

(b) Wake velocity deficit at 20D downstream of the last turbine row (Case 0 ($CIS = 2.5K; CIH = 500m; FALR = 1K/km$) and Case 1 ($CIS = 2.5K, CIH = 500m, FALR = 10K/km$))

Figure 5.29: Plots showing the wake velocity deficit behind all the turbine rows (Cases 0 and 1)

Furthermore, from Figure 5.29a and Figure 5.29b, it can be observed that the wake velocity deficit along each turbine column is higher in Case 1 (higher FALR) than in Case 0, this implies that the wake recovers faster in the case of a lower value of FALR.

Further, the velocity fluctuations ahead of the farm and within the same result in power fluctuations at each individual turbine. This can be observed in Figure 5.30. In Case 0, presence of a region of favourable pressure at the last two turbine rows accelerates the flow in this region. This results in a higher power output (or a lower drop in the power output between rows 4 and 5 vis-à-vis rows 3 and 4) in the power down the line analysis.

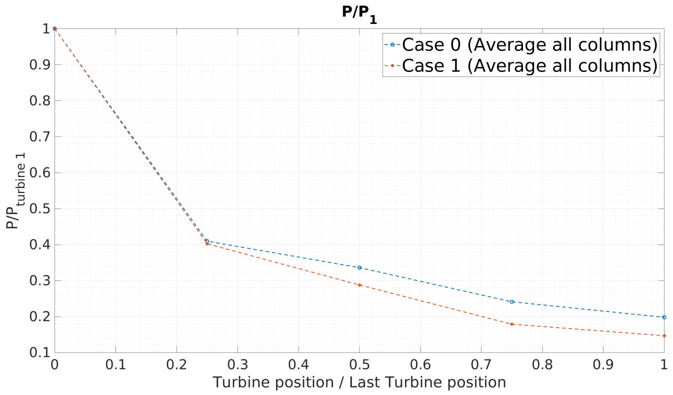

Figure 5.30: Power down the line analysis (for all turbine columns) (Case 0 ($CIS = 2.5K; CIH = 500m; FALR = 1K/km$) and Case 1 ($CIS = 2.5K; CIH = 500m; FALR = 10K/km$))

Thus, it can be understood that changing the FALR changes the characteristics of the AGWs propagating in the free atmosphere. Based on the characteristics of the AGWs triggered in the Free atmosphere, the resulting pressure fluctuations change at the hub height, which can further lead to a blockage ahead of the farm and accelerated flow towards the last two turbines.

5.4. Summary of main conclusions

The chapter sheds light upon the characteristics of the AGWs excited by the wind farm and the impact of them upon the wind farm itself. The key conclusions from the present chapter include:

- The wind turbines extracting energy from the turbines cause a flow deceleration ahead of the farm. To compensate for reduced mass flow through the farm, an upward flow deflection occurs. This pushes the inversion layer upwards, triggering AGWs. In all the cases considered in the present study, there has been AGWs excited in the Free Atmosphere. However, in some cases, based on the inversion strength and height, wave trapping was observed. The excited AGWs cause pressure fluctuations at the hub height of the wind turbine. These pressure fluctuations lead to a flow deceleration ahead of the wind farm and an acceleration towards the lee of the same. Further, these pressure fluctuations at the hub height of the turbines is dependent on the type of waves excited by the wind farm. Furthermore, the Froude number of the incoming flow decides whether the AGWs propagate upstream of the exciting topography (the wind farm).

- A stronger low hanging capping inversion excites AGWs in the free atmosphere and also forced interfacial waves travelling horizontally along the capping inversion. The resulting pressure fluctuations cause change in the velocity and direction upstream of the farm (depending on the Fr of the incoming flow) and downstream of the same. The trapped AGWs propagating horizontally cause velocity fluctuations within the farm and in the lee of the same. The velocity fluctuations within the farm aid in the wake recovery between turbine rows. However, the AGWs propagating upstream create alternating regions of increased and reduced pressure ahead of the farm, causing local acceleration/ deceleration. It was observed that in spite of these pressure fluctuations, a higher blockage (based on the definition of the same in the present study (refer subsection 2.1.5) was observed for a higher capping inversion strength ($\approx 5\%$ at an upstream distance of $\approx 10D$), which causes a drop of $\approx 15\%$ in the incoming wind power. Also, the AGW assisted wake recovery observed in the stronger CI case resulted in a higher power output. Furthermore, the velocity fluctuations due to the presence of trapped AGWs propagating along the capping inversion resulted a quicker wake recovery in the lee of the farm.
- The height of the capping inversion determined the magnitude of the AGW excitation in the free atmosphere. For a higher capping inversion, weaker AGWs were excited in the Free Atmosphere. The higher capping inversion exhibited milder AGW induced pressure fluctuations at the hub height. This can be attributed to the increased distance between the exciting topography (the farm) and the AGWs. However, AGW induced pressure fluctuations were observed for a low hanging capping inversion, which also caused changes in the direction of the incoming wind. A higher Capping inversion resulted in a lower blockage ahead of the farm, a lower velocity deficit within the farm, and also an earlier wake recovery.
- The Free Atmosphere Lapse Rate determines the vertical wavelength of the AGWs propagating in the free atmosphere. A higher FALR excites waves of shorter vertical wavelength in the free atmosphere. The AGW induced adverse pressure gradient ahead of the farm is shorter and more severe in the case of a lower capping inversion. This leads to a higher flow blockage ahead of the farm.

6

Conclusions and Recommendations

The summary listed in the previous chapter contains all the main conclusions from the results obtained. However, there are a few limitations to the present analysis. These are

6.1. Main conclusions

The main conclusions of the present thesis are summarized as follows:

- For all the cases simulated, the deceleration of the flow within the farm, led to an upward flow deflection, which lifted the base of the inversion layer, thereby exciting AGWs in the free atmosphere.
- The excited AGWs created an adverse pressure gradient upstream of the farm and a favourable pressure gradients downstream of the same. These changed the flow direction in and around the farm, and also caused fluctuations in the velocity magnitude at each individual turbine, which lead to a power fluctuation at each individual turbine.
- A higher capping inversion strength led to higher wave trapping in the lee of the farm. The trapped waves propagated horizontally along the capping inversion. As the flow in the considered case was sub critical, the trapped AGW's were also propagating against the mean flow direction. These caused pressure fluctuations that affected the direction of the velocity magnitude and the flow direction upstream of the farm and around the same. This leads to a lower flow blockage and therefore a higher power output for the higher capping inversion strength. Also, the trapped lee waves were cause fluctuations in the flow direction and velocity magnitude in the lee of the farm.
- A higher capping inversion height led to a lower AGW excitation and therefore lower pressure and subsequently lower velocity fluctuations at the hub height of the turbine. A higher capping inversion height led to a lower AGW induced flow blockage and therefore higher overall power output as compared to its low hanging counterpart.
- The FALR determines the vertical wavelength of the AGW in the free atmosphere. The characteristics of the AGW's excited determine the nature of the pressure fluctuations at the hub height of the turbine. In the present study, a higher FALR led to a lower flow blockage and a higher wind farm power output.

6.2. Recommendations

6.2.1. Future case setup

The present study uses a grid of $10\ km$ in the vertical direction, half of which is the Rayleigh damping layer. The mesh therefore does not completely capture a complete vertical wavelength in the case of a lower FALR.

Further, expanding the grid and changing the position of the inversion layer led to a divergence in the solutions. This was also the case when the mesh above the inversion layer was refined. The flow solution would diverge after a few iterations. This tendency was also observed while performing the trial and error operation to determine the optimal damping thicknesses and coefficients. Since the layout of the wind farm remains unchanged throughout the process, the main reason for the divergence of the solver could be speculated as follows - Changing the grid resolution may lead to over or underestimation of the mass flux at each of the vertical cell faces. This could then lead to an over excitation of the AGW by the wind turbines. Thus, the obtained values of the damping thickness and coefficient may no longer be valid.

Furthermore, research needs to be carried out in determining the optimal placement of the damping layers in the domain. In that it should specifically answer the following questions posed:

- What is the ideal distance of each of the damping layers from the wind farm?
- Is there a universal value of damping coefficient and thickness that would provide a working CFD simulation for all configurations of the CNBL or are the aforementioned parameters dependent upon the CNBL characteristics?
- What is the right set of damping coefficients and thicknesses for minimizing or negating the amount of AGW reflections from the boundaries of the domain?

6.2.2. Solver fidelity

In the present case, URANS simulations are used to provide planar averaged data as input and initial values in the main mesh. The simulations are run on a single column model, assuming that the CFD RANS solver assumes horizontal homogeneity. However, this is not the case. For the same grid resolution and a different mesh dimensions, the planar averaged values of the velocity magnitude ($\sqrt{u^2 + v^2}$) and horizontal flow angle ($tan^{-1}(v/u)$) showed different vertical profiles. The reason for the same needs to be understood in future research works that use the same URANS solver to run the precursor simulation.

The current RANS solver depends on statistical averaging, which also uses an isotropic eddy viscosity model to address the turbulence closure problem. Although the $k - \epsilon$ model has been widely used to simulate ABL flows, it only provides a very approximate solution to the flow problem at hand. The unsteady impacts of self-induced AGW's needs to be researched using a CFD solver of higher fidelity (eg. LES or DNS), which could also account for the unsteady impact of AGWs on the wind farm.

6.2.3. Recommendations regarding modelling of wind farm

The present study only considers a single aligned layout of the turbines within the farm. Altering the wind farm layouts, the span and stream-wise distances between turbines effect of the self-induced gravity waves upon the farm needs to be researched further.

Also, the impact of varying the thickness of the capping inversion layer is yet another factor that has not been considered in the present study. The dependence of AGW excitation upon the same needs to be understood further. In the present study, a pressure gradient of $0.001 N/m^2$ is imposed in the domain to drive the geostrophic velocity. Instead, real time data could also be used from weather forecasting models (such as WRF) to impose additional forcing terms in the momentum equations, that would present a more realistic image of the AGW propagation within the domain.

The present study does not account for the tower shadow of the turbines and therefore does not consider the impact it has on the effective wind direction and power output of the farm. While the impact of the vortices shed by the flow around a single tower may be minimal. The cumulative impact of the same on the flow direction may be a non-negligible quantity.

Lastly, it should be understood that the current study describes the surface roughness of the sea, using a constant aerodynamic surface roughness length. However, this is a major simplification. An alternate approach could be to study the wave topology and time periods, and implement them as forcing terms in the momentum equation.

7

Appendix

7.1. SIMPLE Algorithm

The incompressible continuity and momentum equations can be written as:

$$\nabla \cdot \mathbf{U} \tag{7.1}$$

$$\mathbf{U} \cdot \nabla\mathbf{U} - \nabla \cdot (\frac{\mu}{\rho}\nabla\mathbf{U}) = -\nabla p \tag{7.2}$$

where in Equation 7.2 p is the kinematic pressure p/ρ. These form a set of 4 equations and four unknowns U_x,U_y,U_z and p. There exists 4 equations, however there is no equation specifically solving for p. Also the computed values of U_x,U_y,U_z obtained from the momentum equations should together satisfy the continuity equation. Further, the equation of state cannot be used to compute pressure as density and temperature may be assumed constant. The main objectives of the SIMPLE algorithm are to derive an equation for pressure from the momentum and continuity equation and to derive a corrector for the velocity field such that it satisfies the continuity equation.

Rewriting the momentum equations in general matrix form is as follows:

$$\mathbf{MU} = -\nabla p \tag{7.3}$$

where in Equation 7.3, $\mathbf{M}$ is the coefficient matrix that is calculated by discretizing the terms in the momentum equations. These depend on the numerical scheme used to discretize each of the partial differential equation.

This can be called a semi-discretized form of the momentum equations. Consider the x component of momentum then the momentum equation can be written in the matrix form as follows:

$$\underbrace{\begin{bmatrix} M_{1,1} & M_{1,2} & M_{1,3} & \dots & M_{1,n} \\ M_{2,1} & M_{2,2} & M_{2,3} & \dots & M_{2,n} \\ M_{3,1} & M_{3,2} & M_{3,3} & \dots & M_{3,n} \\ \vdots & \vdots & \vdots & \vdots & \vdots \\ M_{n,1} & M_{n,2} & M_{n,3} & \dots & M_{n,n} \end{bmatrix}}_{\mathbf{M}} \underbrace{\begin{bmatrix} U_1 \\ U_2 \\ U_3 \\ \vdots \\ U_n \end{bmatrix}}_{\mathbf{U}} = \underbrace{\begin{bmatrix} (\partial p/\partial x)_1 \\ (\partial p/\partial x)_2 \\ (\partial p/\partial x)_3 \\ \vdots \\ (\partial p/\partial x)_n \end{bmatrix}}_{-\nabla p} \tag{7.4}$$

In Equation 7.4, there are n equations for n cell centroids. The coefficients $M_{i,j}$ are all known values. The coefficient matrix ($\mathbf{M}$) is then decomposed into diagonal and off diagonal components. The semi-discretized momentum equation then assumes the form:

$$\mathbf{MU} = -\nabla p \implies \underbrace{\mathbf{A}}_{diagonalterms} \mathbf{U} - \underbrace{H}_{off-diagonalterms} = -\nabla p \tag{7.5}$$

The diagonal matrix $\mathbf{A}$ is of the form:

$$\begin{bmatrix} A_{1,1} & 0 & 0 & \dots & 0 \\ 0 & A_{2,2} & 0 & \dots & 0 \\ 0 & 0 & A_{3,3} & \dots & 0 \\ \vdots & \vdots & \vdots & \vdots & \vdots \\ 0 & 0 & 0 & \dots & A_{n,n} \end{bmatrix} \tag{7.6}$$

The advantage of doing the decomposition is that the diagonal matrix can easily be inverted. Further, the matrix $\mathbf{H}$, which is a known quantity, is evaluated from the off-diagonal terms and the velocity from the prior iteration.

$$\mathbf{H} = \mathbf{AU} - \mathbf{MU} \tag{7.7}$$

The velocity field $\mathbf{U}$ can now be calculated as:

$$\mathbf{U} = \mathbf{A}^{-1}\mathbf{H} - \mathbf{A}^{-1}\nabla p \tag{7.8}$$

This the explicit pressure corrector stage. By substituting this into the continuity equation $\nabla \cdot \mathbf{U}$, a Poisson equation for pressure can be derived as follows

$$\nabla \cdot (\mathbf{A}^{-1}\nabla p) = \nabla \cdot (\mathbf{A}^{-1}\mathbf{H}) \tag{7.9}$$

Thus, there are now 4 equations with 4 unknowns (viz. U_x, U_y, U_z, p), with an explicit equation for pressure. The numerical computation is as follows: As the SIMPLE algorithm is recommended for steady cases where there is no time derivative.

$$\frac{\partial \mathbf{U}}{\partial t} = \frac{\mathbf{U}_p^{i+1} - \mathbf{U}_p^{i}}{\Delta t} \tag{7.10}$$

When the Δt in the above relation is small, the time derivative is higher than the other terms in the equations ($\nabla^2\mathbf{U}$ and $\nabla \cdot (\mathbf{UU})$. The time derivatives are always placed upon the diagonal of the matrix ($\mathbf{M}$). A small-time step (Δt) ensures that these terms becomes larger, and thus the system becomes diagonally dominant. In the case of steady flows, an under relaxation is required to artificially increase diagonal dominance. This implies that the equations become more stable, and they take lesser iterations to solve. This is achieved using an under relaxation factor (α, where $0 < \alpha < 1$).

The momentum equation can be rewritten as:

$$\underbrace{a_p\mathbf{U}_p}_{diagonalterms} + \underbrace{\Sigma_N(a_N\mathbf{U_N})}_{offdiagonalterms} = RHS \tag{7.11}$$

Under-relaxing the momentum equation gives the following:

$$\underbrace{\frac{1-\alpha}{\alpha}a_p\mathbf{U_p}}_{1} + a_p\mathbf{U_p} + \Sigma_N(a_N\mathbf{U_N}) = RHS + \underbrace{\frac{1-\alpha}{\alpha}a_p\mathbf{U^{OLD}}_p}_{2} \tag{7.12}$$

When the equations converge, $\mathbf{U^{OLD}}_p = \mathbf{U_p}$ and terms 1 and 2 would disappear. Further, Equation 7.12 can be re-written as:

$$\underbrace{\frac{1}{\alpha}a_p\mathbf{U_p}}_{3} + a_p\mathbf{U_p} + \Sigma_N(a_N\mathbf{U_N}) = RHS + \frac{1-\alpha}{\alpha}a_p\mathbf{U_p^{OLD}} \tag{7.13}$$

In Equation 7.13, term 3, which is the diagonal of the $\mathbf{M}$ matrix is scaled by $\frac{1}{\alpha}$. As $0 < \alpha < 1$, the diagonal terms become significantly bigger as α becomes smaller.

Similar under relaxation can be applied to the pressure solution ($p = \alpha p_{NEW} + (1-\alpha)p_{OLD}$) and to the solutions of other scalar transport equations (such as θ, k, ϵ).

The SIMPLE algorithm follows the solution process as follows:

- The momentum equation in the semi-discretized form $\mathbf{MU} = -\nabla p$ is solved to obtain the velocity field. This is obtained from the initial field values of pressure. The obtained velocity field does not satisfy the continuity equation, it only satisfies the momentum equation. This step is also called the momentum predictor.
- The Poisson equation $(\nabla \cdot (\mathbf{A}^{-1}\nabla p) = \nabla \cdot (\mathbf{A}^{-1}\mathbf{H})$ is then solved to obtain the pressure field.
- The obtained pressure field p is used to correct the velocity field such that it satisfies the continuity equation $\mathbf{U} = \mathbf{A}^{-1}\mathbf{H} - \mathbf{A}^{-1}\nabla p$. The corrected velocity field now satisfies the continuity equation. However, the corrected velocity field does not satisfy the momentum equations as the value of H is changed.
- The additional turbulence scalars of k, ϵ and potential temperature θ equations are solved within the loop after the velocity correcter. This is because the kinematic eddy viscosity term is updated from the turbulence scalar transport equation, which is fed back into the momentum equation into the next looping routine.
- Further, to account for non-orthogonality of the mesh considered, correction factors are incorporated as source terms. This is referred to as the non-orthogonal correction step which involves solving the Posisson equation for pressure multiple times.
- All the above steps are repeated till a divergence free velocity field is obtained which satisfies the continuity equations.

7.2. PISO algorithm

PISO algorithm is used to model unsteady or transient flow.

The algorithm works as follows:

- In the case of the PISO algorithm, the momentum predictor (Equation 7.3) is just solved once.
- Following this, $\mathbf{H}$ is determined from, $\mathbf{H} = \mathbf{AU} - \mathbf{MU}$ followed by the solution to the pressure equation $(\nabla \cdot (\mathbf{A}^{-1}\nabla p) = \nabla \cdot (A^{-1}\mathbf{H}))$ and updating the velocity field $(\mathbf{U} = \mathbf{A}^{-1}\mathbf{H} - \mathbf{A}^{-1}\nabla p)$.

  The velocity field predicted is used directly to solve for $\mathbf{H}$, followed by solution of the pressure equation and then updating the velocity.
- Attaining a complete convergence for each time-step is computationally expensive. Thus, if the time step is small enough $(C < 1)$, then the momentum predictor and inner loop pressure corrections can be solved (the number of times each of these equations are solved is specified by the user) to attain partial convergence (limit specified by the user). As the time steps are already small, the system is already diagonally dominant. Thus, there is no need to incorporate under-relaxation in transient solutions.

7.3. Results - SCM - Cases 1 to 7

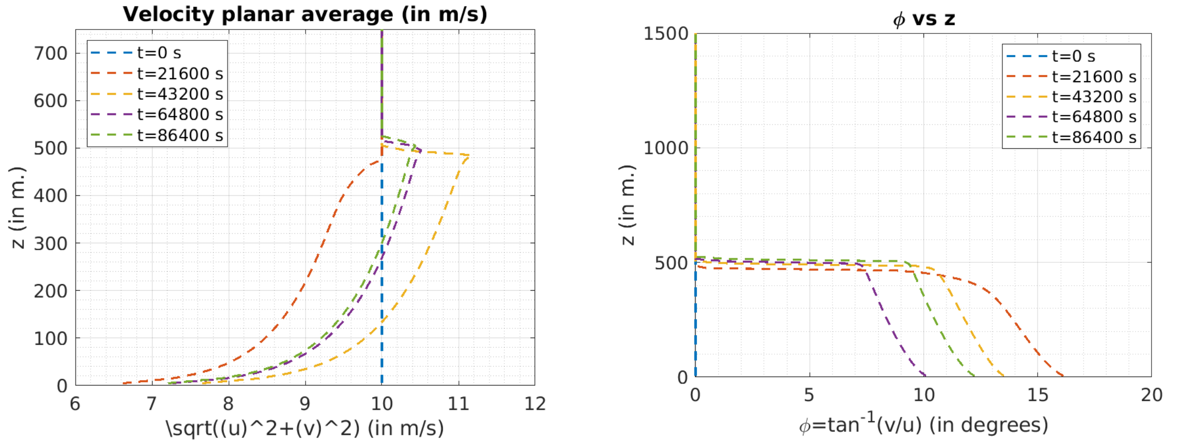

(a) Evolution of the planar velocity $\sqrt{u^2 + v^2}$ over 24 hours

(b) Evolution of horizontal flow direction $tan^{-1}\frac{V}{U}$ profiles over 24 hours

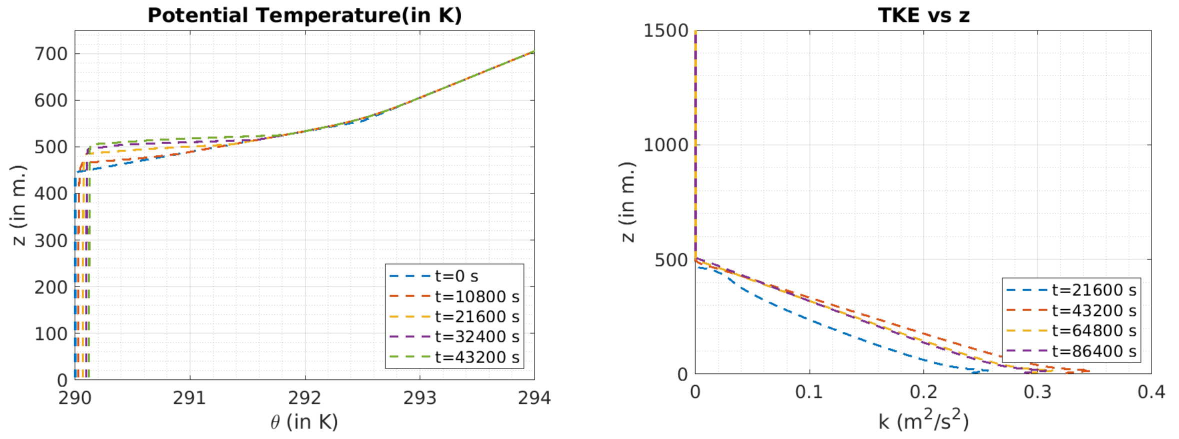

(c) Evolution of the θ over time

(d) Evolution of the TKE profiles over 24 hours

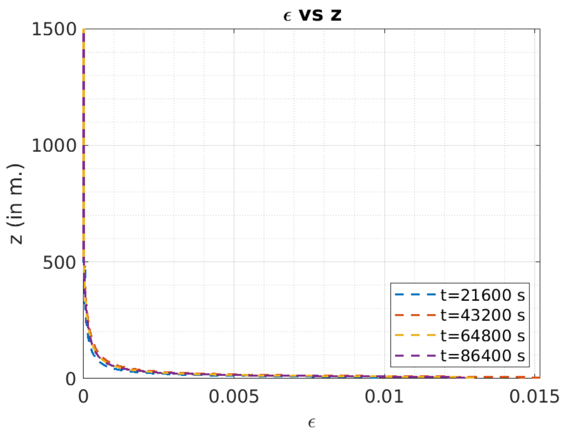

(e) Evolution of ϵ over 24 hours

Figure 7.1: Evolution of profiles of the flow variables over 24 hours for Case 1 (CIS=2.5K; CIH=500m; FALR=10K/km)

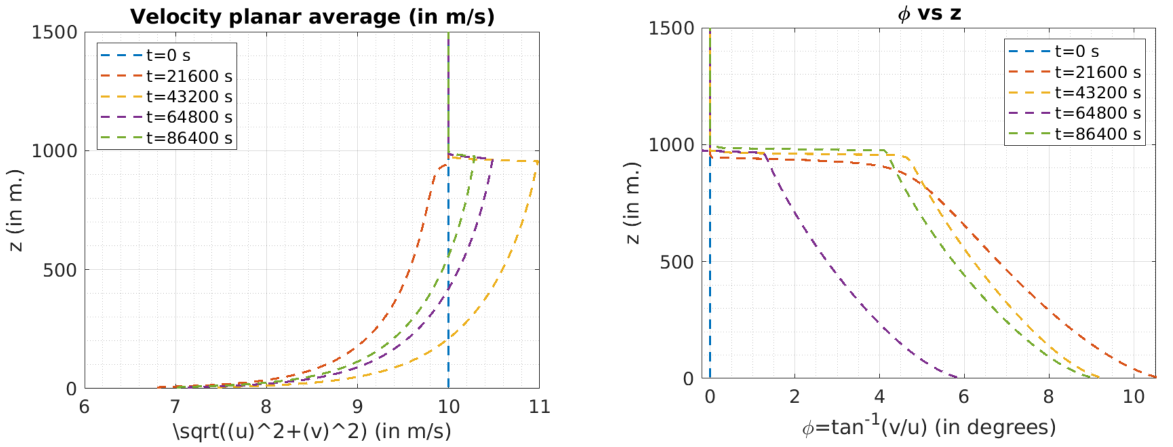

(a) Evolution of the planar velocity $\sqrt{u^2 + v^2}$ over 24 hours

(b) Evolution of horizontal flow direction $tan^{-1}\frac{V}{U}$profiles over 24 hours

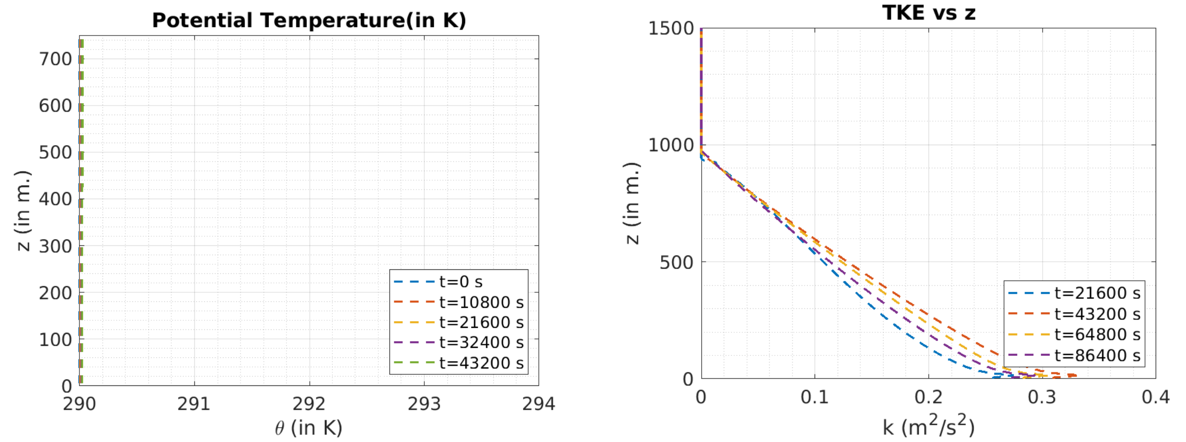

(c) Evolution of the θ over time

(d) Evolution of the TKE profiles over 24 hours

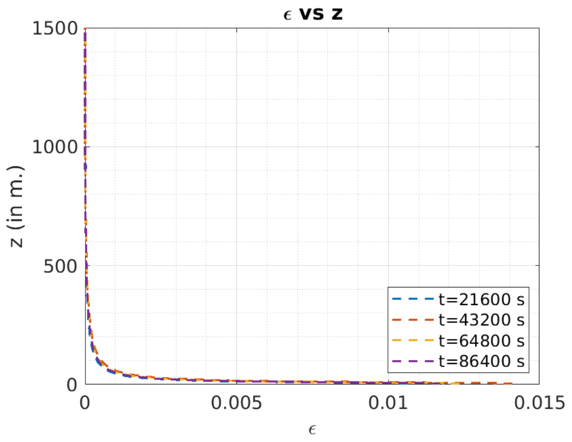

(e) Evolution of ϵ over 24 hours

Figure 7.2: Evolution of profiles of the flow variables over 24 hours for Case 2 (CIS=2.5K; CIH=1000m; FALR=1K/km)

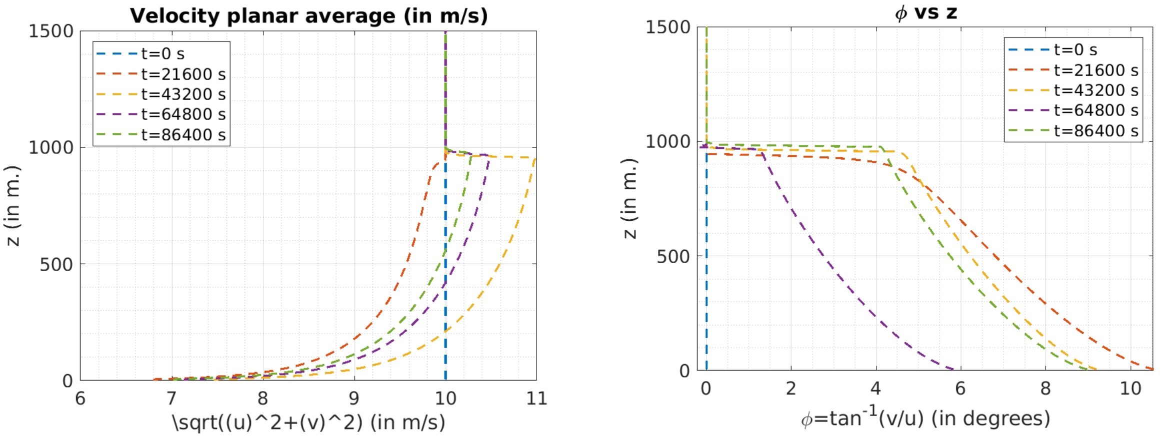

(a) Evolution of the planar velocity $\sqrt{u^2 + v^2}$ over 24 hours

(b) Evolution of horizontal flow direction $tan^{-1} \frac{V}{U}$ profiles over 24 hours

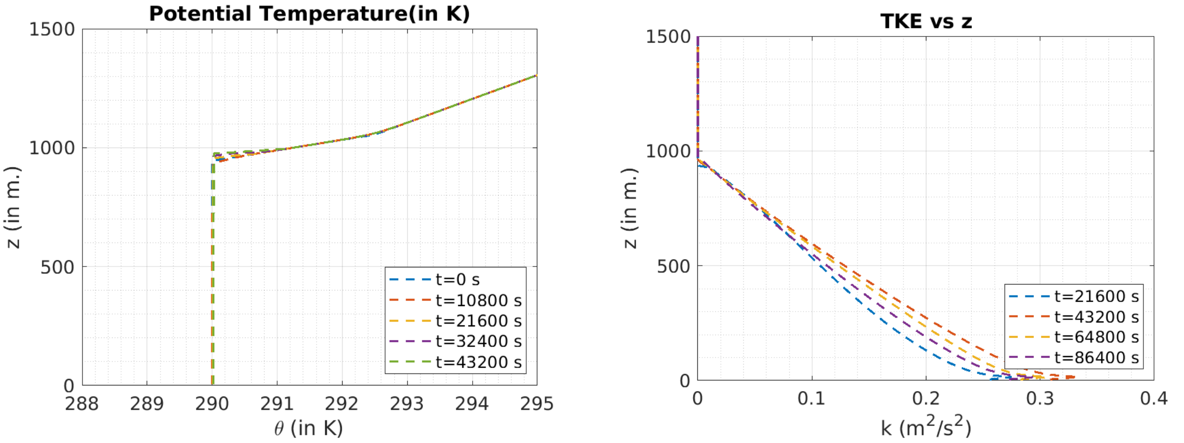

(c) Evolution of the θ over time

(d) Evolution of the TKE profiles over 24 hours

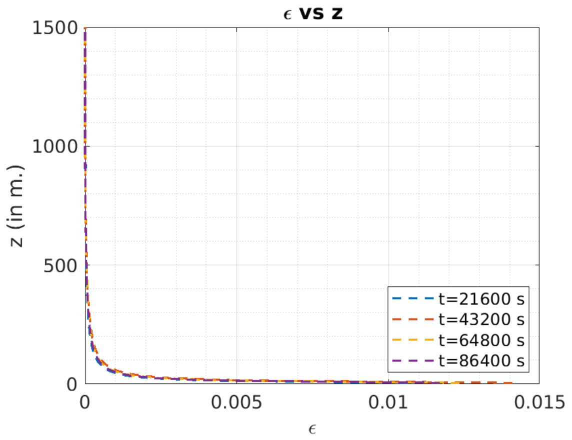

(e) Evolution of ϵ over 24 hours

Figure 7.3: Evolution of profiles of the flow variables over 24 hours for Case 3 (CIS=2.5K; CIH=1000m; FALR=10K/km)

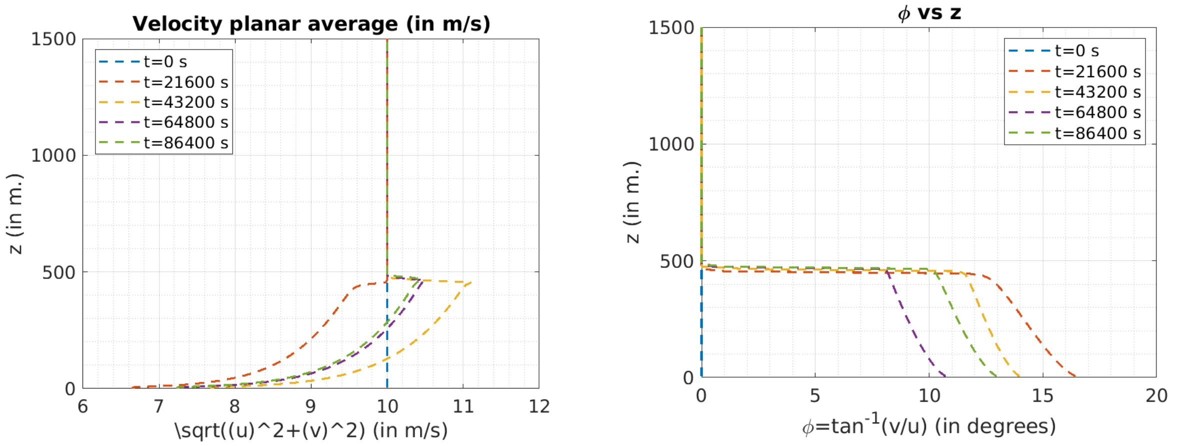

(a) Evolution of the planar velocity $\sqrt{u^2 + v^2}$ over 24 hours

(b) Evolution of horizontal flow direction $tan^{-1}\frac{V}{U}$ profiles over 24 hours

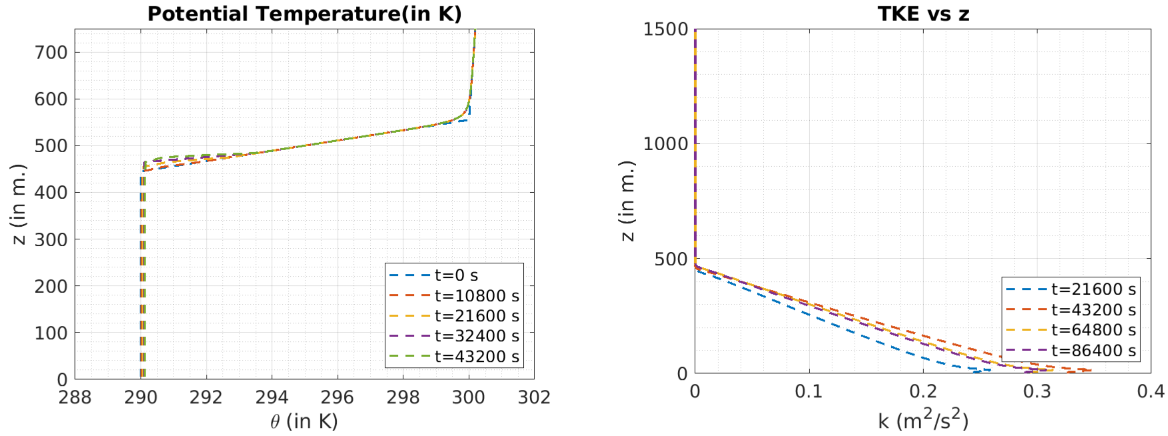

(c) Evolution of the θ over time

(d) Evolution of the TKE profiles over 24 hours

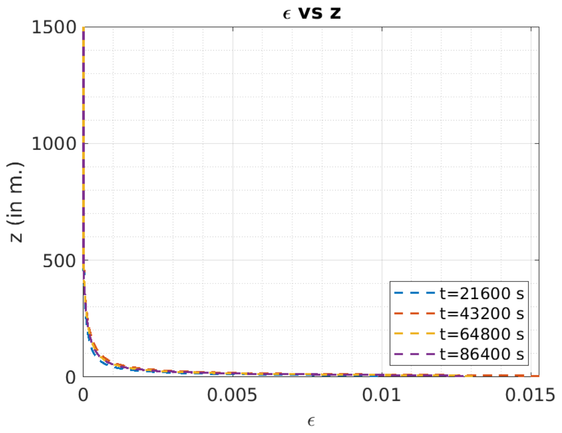

(e) Evolution of ϵ over 24 hours

Figure 7.4: Evolution of profiles of the flow variables over 24 hours for Case 4 (CIS=10K; CIH=500m; FALR=1K/km)

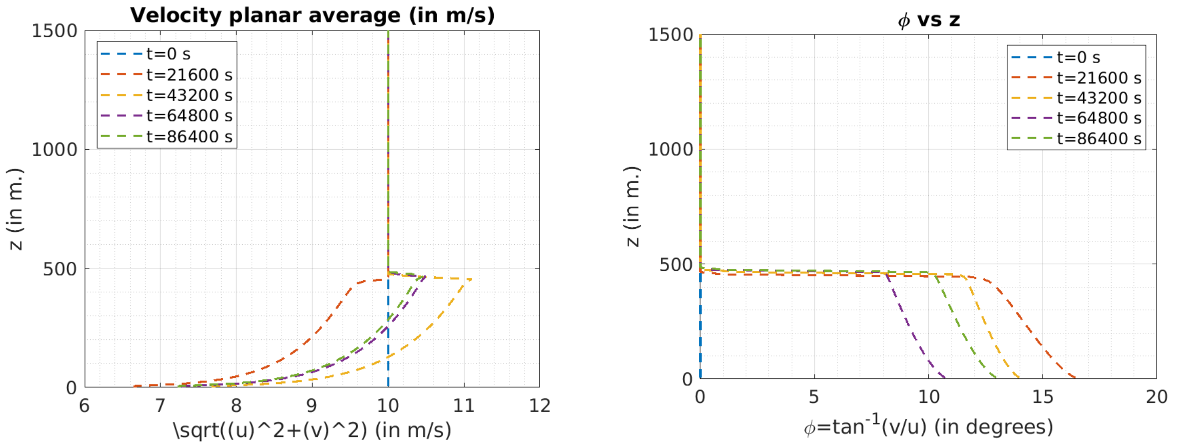

(a) Evolution of the planar velocity $\sqrt{u^2+v^2}$ over 24 hours

(b) Evolution of horizontal flow direction $tan^{-1}\frac{V}{U}$ profiles over 24 hours

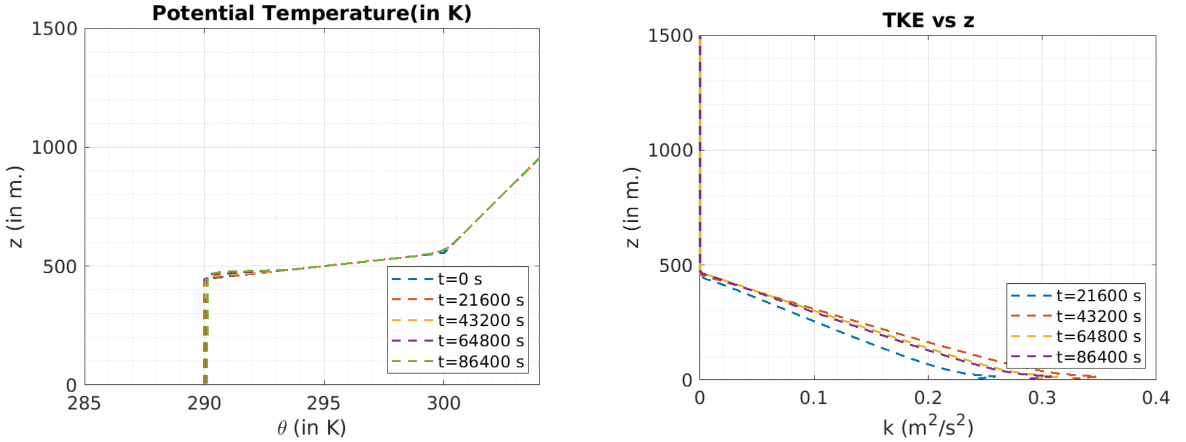

(c) Evolution of the θ over time

(d) Evolution of the TKE profiles over 24 hours

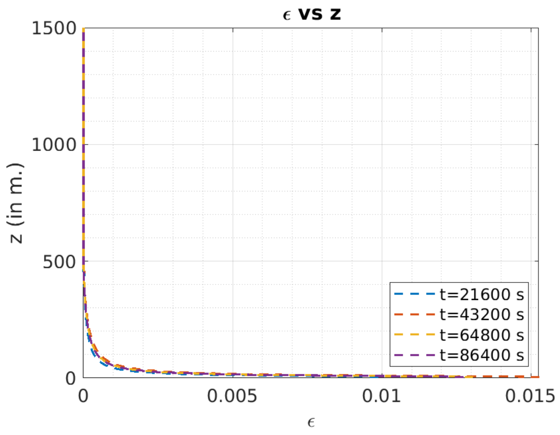

(e) Evolution of ϵ over 24 hours

Figure 7.5: Evolution of profiles of the flow variables over 24 hours for Case 5 (CIS=10K; CIH=500m; FALR=10K/km)

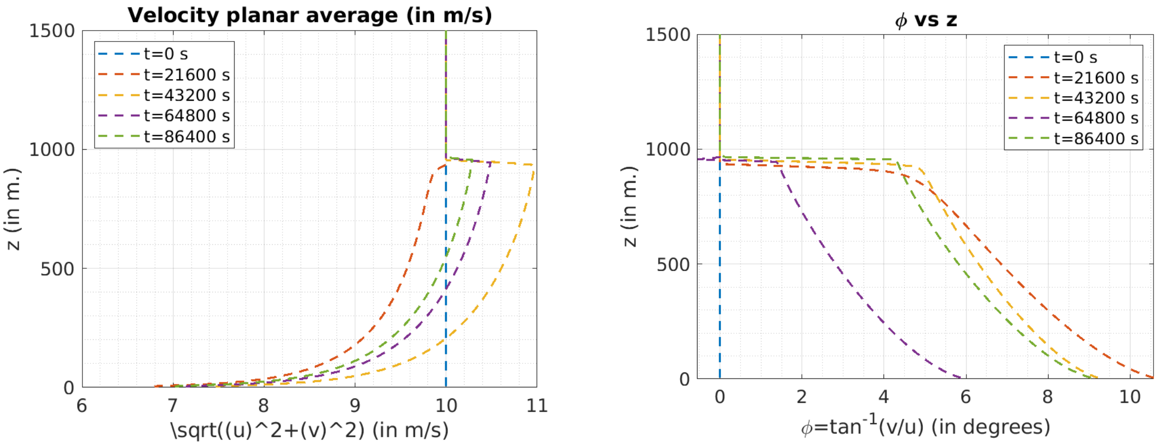

(a) Evolution of the planar velocity $\sqrt{u^2 + v^2}$ over 24 hours

(b) Evolution of horizontal flow direction $tan^{-1}\frac{V}{U}$ profiles over 24 hours

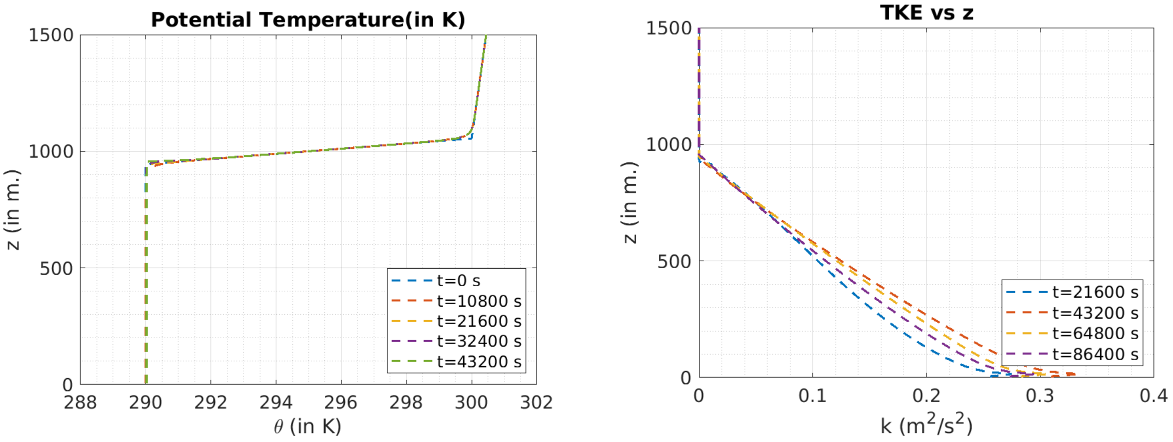

(c) Evolution of the θ over time

(d) Evolution of the TKE profiles over 24 hours

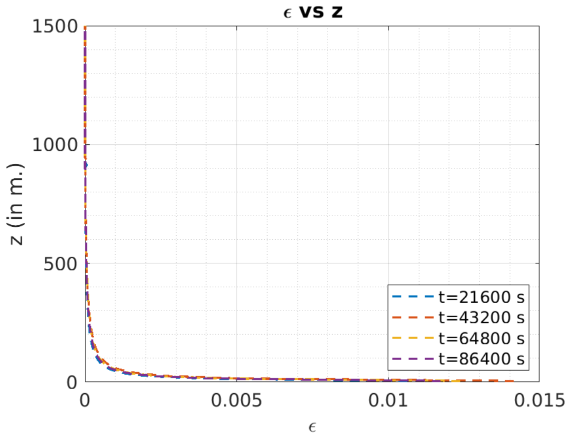

(e) Evolution of ϵ over 24 hours

Figure 7.6: Evolution of profiles of the flow variables over 24 hours for Case 6 (CIS=10K; CIH=1000m; FALR=1K/km)

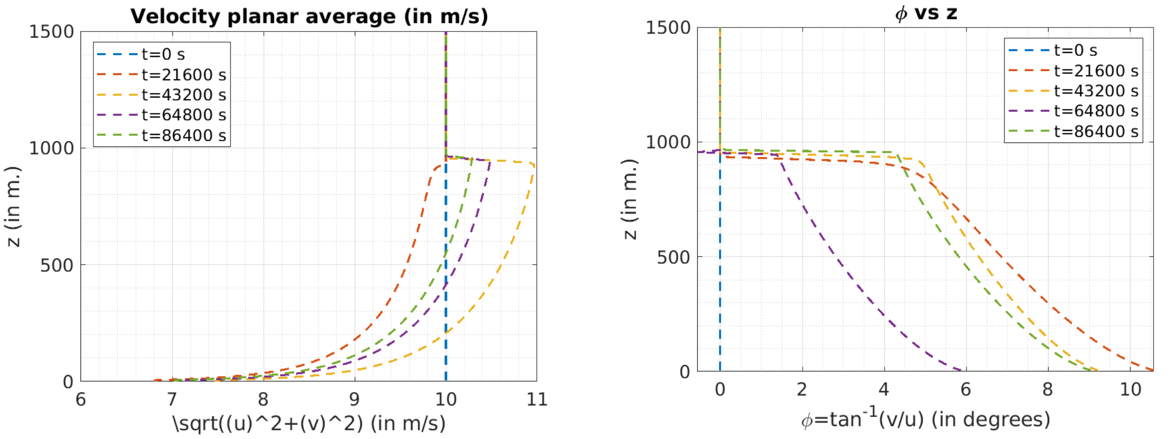

(a) Evolution of the planar velocity $\sqrt{u^2+v^2}$ over 24 hours

(b) Evolution of horizontal flow direction $tan^{-1}\frac{V}{U}$ profiles over 24 hours

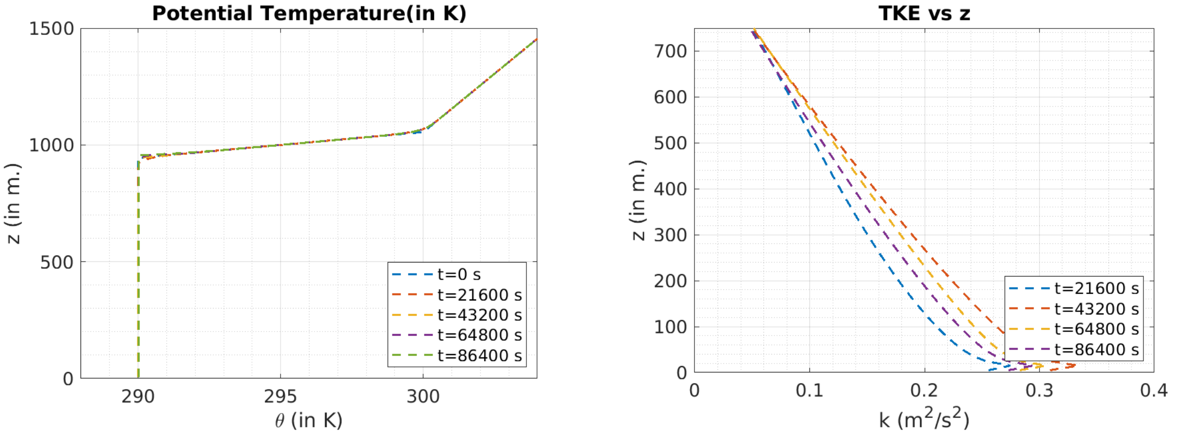

(c) Evolution of the θ over time

(d) Evolution of the TKE profiles over 24 hours

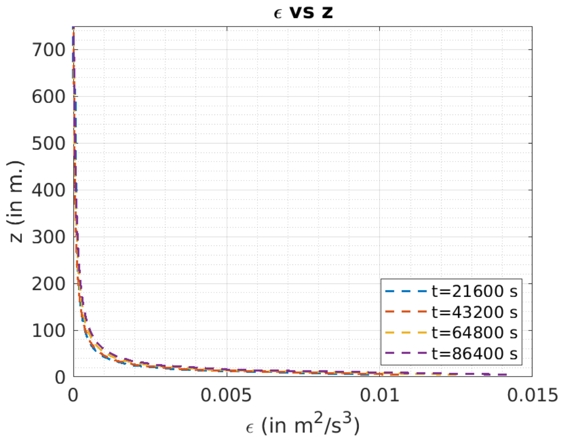

(e) Evolution of ϵ over 24 hours

Figure 7.7: Evolution of profiles of the flow variables over 24 hours for Case 7 (CIS=10K; CIH=1000m; FALR=10K/km)

Bibliography

M. Abkar and F. Porté-Agel. The effect of free-atmosphere stratification on boundary-layer flow and power output from very large wind farms. *Energies*, 6(5):2338–2361, 2013. ISSN 19961073. doi: 10.3390/en6052338.

M. Abkar and F. Porté-Agel. Mean and turbulent kinetic energy budgets inside and above very large wind farms under conventionally-neutral condition, 2014. ISSN 09601481.

M. Abkar and F. Porté-Agel. Influence of atmospheric stability on wind-turbine wakes: A large-eddy simulation study. *Physics of Fluids*, 27(3):035104, Mar. 2015. ISSN 1070-6631, 1089-7666. doi: 10.1063/1.4913695. URL `http://aip.scitation.org/doi/10.1063/1.4913695`.

D. Allaerts. Faculty of Engineering Science Large-eddy simulation of wind farms in conventionally neutral and stable atmospheric boundary layers. (November), 2016.

D. Allaerts and J. Meyers. Wind farm performance in conventionally neutral atmospheric boundary layers with varying inversion strengths. *Journal of Physics: Conference Series*, 524(1), 2014. ISSN 17426596. doi: 10.1088/1742-6596/524/1/012114.

D. Allaerts and J. Meyers. Large eddy simulation of a large wind-turbine array in a conventionally neutral atmospheric boundary layer. *Physics of Fluids*, 27(6):065108, June 2015. ISSN 1070-6631, 1089-7666. doi: 10.1063/1.4922339. URL `http://aip.scitation.org/doi/10.1063/1.4922339`.

D. Allaerts and J. Meyers. Boundary-layer development and gravity waves in conventionally neutral wind farms. *Journal of Fluid Mechanics*, 814:95–130, Mar. 2017. ISSN 0022-1120, 1469-7645. doi: 10.1017/jfm.2017.11. URL `https://www.cambridge.org/core/product/identifier/S0022112017000118/type/journal_article`.

D. Allaerts and J. Meyers. Gravity Waves and Wind-Farm Efficiency in Neutral and Stable Conditions. *Boundary-Layer Meteorology*, 166(2):269–299, Feb. 2018. ISSN 0006-8314, 1573-1472. doi: 10.1007/s10546-017-0307-5. URL `http://link.springer.com/10.1007/s10546-017-0307-5`.

D. Allaerts and J. Meyers. Sensitivity and feedback of wind-farm-induced gravity waves. *Journal of Fluid Mechanics*, 862:990–1028, Mar. 2019. ISSN 0022-1120, 1469-7645. doi: 10.1017/jfm.2018.969. URL `https://www.cambridge.org/core/product/identifier/S0022112018009692/type/journal_article`.

D. Allaerts, S. V. Broucke, N. van Lipzig, and J. Meyers. Annual impact of wind-farm gravity waves on the Belgian–Dutch offshore wind-farm cluster. *Journal of Physics: Conference Series*, 1037:072006, June 2018. ISSN 1742-6588, 1742-6596. doi: 10.1088/1742-6596/1037/7/072006. URL `https://iopscience.iop.org/article/10.1088/1742-6596/1037/7/072006`.

I. Ammara, C. Leclerc, and C. Masson. A viscous three-dimensional differential/actuator-disk method for the aerodynamic analysis of wind farms. *Journal of Solar Energy Engineering-transactions of The Asme - J SOL ENERGY ENG*, 124, 11 2002. doi: 10.1115/1.1510870.

J. D. Anderson. *Fundamentals of aerodynamics*. McGraw-Hill, 5th edition, Feb. 2011. ISBN 9780073398105. URL `http://www.worldcat.org/isbn/9780073398105`.

A. Andren, A. R. Brown, P. J. Mason, J. Graf, U. Schumann, C.-H. Moeng, and F. T. M. Nieuwstadt. Large-eddy simulation of a neutrally stratified boundary layer: A comparison of four computer codes. *Quarterly Journal of the Royal Meteorological Society*, 120(520):1457–1484, 1994. doi: https://doi.org/10.1002/qj.49712052003. URL `https://rmets.onlinelibrary.wiley.com/doi/abs/10.1002/qj.49712052003`.

D. D. Apsley and I. A. N. P. Castro. A LIMITED-LENGTH-SCALE k-ϵ MODEL FOR THE NEUTRAL AND STABLY-STRATIFIED ATMOSPHERIC BOUNDARY LAYER. *Boundary-Layer Meteorology*, 83 (1):75–98, 1997. ISSN 1573-1472. doi: 10.1023/A:1000252210512. URL `https://doi.org/10.1023/A:1000252210512`.

S. Arya. Comparative effects of stability, baroclinity and the scale-height ratio on drag laws for the atmospheric boundary layer. *Journal of The Atmospheric Sciences - J ATMOS SCI*, 35:40–46, 01 1978. doi: 10.1175/1520-0469(1978)035<0040:CEOSBA>2.0.CO;2.

S. P. S. Arya. Comments on “similarity theory for the planetary boundary layer of time-dependent height”. *Journal of Atmospheric Sciences*, 32(4):839 – 840, 1975. doi: 10.1175/1520-0469(1975)032<0839:COTFTP>2.0.CO;2. URL `https://journals.ametsoc.org/view/journals/atsc/32/4/1520-0469_1975_032_0839_cotftp_2_0_co_2.xml`.

A. Banerjee, T. Chakraborty, V. Matsagar, and T. Datta. *Dynamic Analysis of Offshore Wind Turbine Structures*, pages 116–191. 08 2016. ISBN 9781522505891. doi: 10.4018/978-1-5225-0588-4.ch005.

R. M. Banta, Y. L. Pichugina, W. A. Brewer, J. K. Lundquist, N. D. Kelley, S. P. Sandberg, R. J. A. II, R. M. Hardesty, and A. M. Weickmann. 3d volumetric analysis of wind turbine wake properties in the atmosphere using high-resolution doppler lidar. *Journal of Atmospheric and Oceanic Technology*, 32 (5):904 – 914, 2015. doi: 10.1175/JTECH-D-14-00078.1. URL `https://journals.ametsoc.org/view/journals/atot/32/5/jtech-d-14-00078_1.xml`.

R. Barthelmie, G. Larsen, S. Pryor, H. Jørgensen, H. Bergström, W. Schlez, K. Rados, B. Lange, P. Vølund, S. Neckelmann, S. Mogensen, G. Schepers, T. Hegberg, L. Folkerts, and M. Magnusson. Endow (efficient development of offshore wind farms): modelling wake and boundary layer interactions. *Wind Energy*, 7(3):225–245, 2004. doi: https://doi.org/10.1002/we.121. URL `https://onlinelibrary.wiley.com/doi/abs/10.1002/we.121`.

R. J. Barthelmie, S. C. Pryor, S. T. Frandsen, K. S. Hansen, J. G. Schepers, K. Rados, W. Schlez, A. Neubert, L. E. Jensen, and S. Neckelmann. Quantifying the impact of wind turbine wakes on power output at offshore wind farms. *Journal of Atmospheric and Oceanic Technology*, 27(8):1302 – 1317, 2010. doi: 10.1175/2010JTECHA1398.1. URL `https://journals.ametsoc.org/view/journals/atot/27/8/2010jtecha1398_1.xml`.

J. Bartl and L. Sætran. Blind test comparison of the performance and wake flow between two in-line wind turbines exposed to different turbulent inflow conditions. *Wind Energy Science*, 2(1):55–76, 2017. ISSN 23667451. doi: 10.5194/wes-2-55-2017.

M. Bastankhah and F. Porté-Agel. A new analytical model for wind-turbine wakes. *Renewable Energy*, 70:116–123, Oct. 2014. ISSN 09601481. doi: 10.1016/j.renene.2014.01.002. URL `https://linkinghub.elsevier.com/retrieve/pii/S0960148114000317`.

M. Bastankhah and F. Porté-Agel. Wind tunnel study of the wind turbine interaction with a boundary-layer flow: Upwind region, turbine performance, and wake region. *Physics of Fluids*, 29(6):065105, June 2017. ISSN 1070-6631, 1089-7666. doi: 10.1063/1.4984078. URL `http://aip.scitation.org/doi/10.1063/1.4984078`.

A. K. Betts. Reply to comment on the paper 'non-precipitating cumulus convection and its parameterization'. *Quarterly Journal of the Royal Meteorological Society*, 100(425):469–471, 1974. doi: https://doi.org/10.1002/qj.49710042517. URL `https://rmets.onlinelibrary.wiley.com/doi/abs/10.1002/qj.49710042517`.

F. Bingöl, J. Mann, and G. C. Larsen. Light detection and ranging measurements of wake dynamics part i: one-dimensional scanning. *Wind Energy*, 13(1):51–61, 2010. doi: https://doi.org/10.1002/we.352. URL `https://onlinelibrary.wiley.com/doi/abs/10.1002/we.352`.

A. K. Blackadar. Boundary Layer Wind Maxima and Their Significance for the Growth of Nocturnal Inversions. *Bulletin of the American Meteorological Society*, 38(5):283–290, 1957. ISSN 0003-0007. doi: 10.1175/1520-0477-38.5.283.

J. Bleeg, M. Purcell, R. Ruisi, and E. Traiger. Wind farm blockage and the consequences of neglecting its impact on energy production. *Energies*, 11(6), 2018. ISSN 19961073. doi: 10.3390/en11061609.

E. Branlard, E. Quon, A. R. Meyer Forsting, J. King, and P. Moriarty. Wind farm blockage effects: Comparison of different engineering models. *Journal of Physics: Conference Series*, 1618(6):1–11, 2020. ISSN 17426596. doi: 10.1088/1742-6596/1618/6/062036.

R. A. Brost, D. H. Lenschow, and J. C. Wyngaard. Marine Stratocumulus Layers. Part 1: Mean Conditions. *Journal of the Atmospheric Sciences*, 39(4):800–817, 04 1982. ISSN 0022-4928. doi: 10.1175/1520-0469(1982)039<0800:MSLPMC>2.0.CO;2. URL `https://doi.org/10.1175/1520-0469(1982)039<0800:MSLPMC>2.0.CO;2`.

M. Calaf, C. Meneveau, and J. Meyers. Large eddy simulation study of fully developed wind-turbine array boundary layers. *Physics of Fluids*, 22(1):015110, 2010. ISSN 1070-6631. doi: 10.1063/1.3291077.

M. Calaf, M. B. Parlange, and C. Meneveau. Large eddy simulation study of scalar transport in fully developed wind-turbine array boundary layers. *Physics of Fluids*, 23(12), 2011. ISSN 10706631. doi: 10.1063/1.3663376.

L. P. Chamorro and F. Porté-Agel. A Wind-Tunnel Investigation of Wind-Turbine Wakes: Boundary-Layer Turbulence Effects. *Boundary-Layer Meteorology*, 132(1):129–149, 2009. ISSN 1573-1472. doi: 10.1007/s10546-009-9380-8. URL `https://doi.org/10.1007/s10546-009-9380-8`.

L. P. Chamorro and F. Porté-Agel. Effects of Thermal Stability and Incoming Boundary-Layer Flow Characteristics on Wind-Turbine Wakes: A Wind-Tunnel Study. *Boundary-Layer Meteorology*, 136(3):515–533, 2010. ISSN 1573-1472. doi: 10.1007/s10546-010-9512-1. URL `https://doi.org/10.1007/s10546-010-9512-1`.

L. P. Chamorro and F. Porté-Agel. Turbulent Flow Inside and Above a Wind Farm: A Wind-Tunnel Study. *Energies*, 4(11):1916–1936, Nov. 2011. ISSN 1996-1073. doi: 10.3390/en4111916. URL `http://www.mdpi.com/1996-1073/4/11/1916`.

M. B. Christiansen and C. B. Hasager. Wake effects of large offshore wind farms identified from satellite sar. *Remote Sensing of Environment*, 98(2):251–268, 2005. ISSN 0034-4257. doi: https://doi.org/10.1016/j.rse.2005.07.009. URL `https://www.sciencedirect.com/science/article/pii/S0034425705002476`.

M. Churchfield, S. Lee, P. Moriarty, L. Martínez Tossas, S. Leonardi, G. Vijayakumar, and J. Brasseur. A large-eddy simulation of wind-plant aerodynamics. 01 2012. ISBN 978-1-60086-936-5. doi: 10.2514/6.2012-537.

G. N. Coleman. Similarity statistics from a direct numerical simulation of the neutrally stratified planetary boundary layer. *Journal of the Atmospheric Sciences*, 56(6):891 – 900, 1999. doi: 10.

1175/1520-0469(1999)056<0891:SSFADN>2.0.CO;2. URL https://journals.ametsoc.org/view/journals/atsc/56/6/1520-0469_1999_056_0891_ssfadn_2.0.co_2.xml.

G. N. Coleman, J. H. Ferziger, and P. R. Spalart. A numerical study of the turbulent ekman layer. *Journal of Fluid Mechanics*, 213:313–348, 1990. doi: 10.1017/S0022112090002348.

A. Crespo, J. Hernández, and S. Frandsen. Survey of modelling methods for wind turbine wakes and wind farms. *Wind Energy*, 2(1):1–24, 1999. doi: https://doi.org/10.1002/(SICI)1099-1824(199901/03)2:1<1::AID-WE16>3.0.CO;2-7. URL https://onlinelibrary.wiley.com/doi/abs/10.1002/%28SICI%291099-1824%28199901/03%292%3A1%3C1%3A%3AAID-WE16%3E3.0.CO%3B2-7.

G. Csanady. Equilibrium theory of the planetary boundary layer with an inversion lid. *Boundary-Layer Meteorology*, 6:63–79, 1974.

H. Daaou Nedjari, O. Guerri, and M. Saighi. Full rotor modelling and generalized actuator disc for wind turbine wake investigation. *Energy Reports*, 6(September 2019):232–255, 2020. ISSN 23524847. doi: 10.1016/j.egyr.2019.10.041. URL https://doi.org/10.1016/j.egyr.2019.10.041.

E. Deusebio, G. Brethouwer, P. Schlatter, and E. Lindborg. A numerical study of the unstratified and stratified ekman layer. *Journal of fluid mechanics*, 755:672–704, 2014.

C. Draxl, R. P. Worsnop, G. Xia, Y. Pichugina, D. Chand, J. K. Lundquist, J. Sharp, G. Wedam, J. M. Wilczak, and L. K. Berg. Mountain waves impact wind power generation. preprint, Wind and turbulence, May 2020. URL https://wes.copernicus.org/preprints/wes-2020-77/.

D. R. Durran and J. B. Klemp. Another look at downslope winds. Part II: nonlinear amplification beneath wave-overturning layers, 1987. ISSN 00224928.

M. Dörenkämper, B. Witha, G. Steinfeld, D. Heinemann, and M. Kühn. The impact of stable atmospheric boundary layers on wind-turbine wakes within offshore wind farms. *Journal of Wind Engineering and Industrial Aerodynamics*, 144:146–153, 2015. ISSN 0167-6105. doi: https://doi.org/10.1016/j.jweia.2014.12.011. URL https://www.sciencedirect.com/science/article/pii/S0167610514002694. Selected papers from the 6th International Symposium on Computational Wind Engineering CWE 2014.

V. W. Ekman. On the Influence of the Earth's Rotation on Ocean-Currents, 1905. URL http://www.aos.princeton.edu/WWWPUBLIC/gkv/history/general.html.

A. C. Fitch, J. B. Olson, J. K. Lundquist, J. Dudhia, A. K. Gupta, J. Michalakes, and I. Barstad. Local and Mesoscale Impacts of Wind Farms as Parameterized in a Mesoscale NWP Model. *Monthly Weather Review*, 140(9):3017–3038, Sept. 2012. ISSN 0027-0644, 1520-0493. doi: 10.1175/MWR-D-11-00352.1. URL http://journals.ametsoc.org/doi/10.1175/MWR-D-11-00352.1.

S. Frandsen. On the wind speed reduction in the center of large clusters of wind turbines. *Journal of Wind Engineering and Industrial Aerodynamics*, 39(1):251–265, 1992. ISSN 0167-6105. doi: https://doi.org/10.1016/0167-6105(92)90551-K. URL https://www.sciencedirect.com/science/article/pii/016761059290551K.

D. C. Fritts and M. J. Alexander. Gravity wave dynamics and effects in the middle atmosphere. *Reviews of Geophysics*, 41(1):1–64, 2003. ISSN 87551209. doi: 10.1029/2001RG000106.

S. N. Gadde and R. J. Stevens. Effect of Coriolis force on a wind farm wake. *Journal of Physics: Conference Series*, 1256(1), 2019. ISSN 17426596. doi: 10.1088/1742-6596/1256/1/012026.

E. Gaertner, J. Rinker, L. Sethuraman, F. Zahle, B. Anderson, G. E. Barter, N. J. Abbas, F. Meng, P. Bortolotti, W. Skrzypinski, G. N. Scott, R. Feil, H. Bredmose, K. Dykes, M. Shields, C. Allen, and A. Viselli. IEA Wind TCP Task 37: Definition of the IEA 15-Megawatt Offshore Reference Wind Turbine. pages 1–44, 2020. doi: 10.2172/1603478. URL `https://www.osti.gov/biblio/1603478{%}0Ahttps://www.osti.gov/servlets/purl/1603478`.

E. Gossard and W. Munk. On gravity waves in the atmosphere. *Journal of Atmospheric Sciences*, 11(4): 259–269, 1954. ISSN 0095-9634. doi: https://doi.org/10.1175/1520-0469(1954)011<0259:OGWITA>2.0.CO;2.

A. L. M. Grant. Observations of boundary layer structure made during the 1981 kontur experiment. *Quarterly Journal of the Royal Meteorological Society*, 112(473):825–841, 1986. doi: https://doi.org/10.1002/qj.49711247314. URL `https://rmets.onlinelibrary.wiley.com/doi/abs/10.1002/qj.49711247314`.

I. Grant and P. Parkin. A DPIV study of the trailing vortex elements from the blades of a horizontal axis wind turbine in yaw. *Experiments in Fluids*, 28(4):368–376, 2000. ISSN 1432-1114. doi: 10.1007/s003480050396. URL `https://doi.org/10.1007/s003480050396`.

Y. Han and M. K. Stoellinger. Rans simulations of neutral atmospheric boundary layer flow over complex terrain with comparisons to field measurements. *Wind Energy*, 23(2):91–119, 2020. doi: https://doi.org/10.1002/we.2412. URL `https://onlinelibrary.wiley.com/doi/abs/10.1002/we.2412`.

K. S. Hansen, R. J. Barthelmie, L. E. Jensen, and A. Sommer. The impact of turbulence intensity and atmospheric stability on power deficits due to wind turbine wakes at Horns Rev wind farm: Power deficits in offshore wind farms. *Wind Energy*, 15(1):183–196, Jan. 2012. ISSN 10954244. doi: 10.1002/we.512. URL `http://doi.wiley.com/10.1002/we.512`.

D. Hargreaves and N. Wright. On the use of the k–ε model in commercial cfd software to model the neutral atmospheric boundary layer. *Journal of Wind Engineering Industrial Aerodynamics*, 95(5): 355–369, 2007. doi: 10.1016/j.jweia.2006.08.002.

S. E. Haupt, L. K. Berg, A. Decastro, D. J. Gagne, P. Jimenez, T. Juliano, B. Kosovic, J. D. Mirocha, E. Quon, J. Sauer, D. Allaerts, M. J. Churchfield, C. Draxl, P. Hawbecker, A. Jonko, C. M. Kaul, T. McCandless, D. Munoz-Esparza, and W. J. Shaw. FY 2019 Report of the Atmosphere to Electrons Coupling Project. (November):NO.PNNL–29603, 2020. URL `https://www.osti.gov/biblio/1735568`.

G. D. Hess. The Neutral, Barotropic Planetary Boundary Layer, Capped by a Low-Level Inversion. *Boundary-Layer Meteorology*, 110(3):319–355, 2004. ISSN 1573-1472. doi: 10.1023/B:BOUN.0000007248.42321.d5. URL `https://doi.org/10.1023/B:BOUN.0000007248.42321.d5`.

M. O. Hills and D. R. Durran. Nonstationary trapped lee waves generated by the passage of an isolated jet. *Journal of the Atmospheric Sciences*, 69(10):3040–3059, 2012. ISSN 00224928. doi: 10.1175/JAS-D-12-047.1.

U. Högström, D. N. Asimakopoulos, H. Kambezidis, C. G. Helmis, and A. Smedman. A field study of the wake behind a 2 MW wind turbine. *Atmospheric Environment (1967)*, 22(4):803–820, 1988. ISSN 00046981. doi: 10.1016/0004-6981(88)90020-0.

M. F. Howland, A. S. Ghate, and S. K. Lele. Coriolis effects within and trailing a large finite wind farm. (January):1–16, 2020. doi: 10.2514/6.2020-0994.

X. M. Hu. Boundary Layer (Atmospheric) and Air Pollution: Air Pollution Meteorology. *Encyclopedia of Atmospheric Sciences: Second Edition*, 1(2):227–236, 2015. doi: 10.1016/B978-0-12-382225-3.00499-0.

S. Ivanell, R. Mikkelsen, J. N. Sørensen, and D. Henningson. Stability analysis of the tip vortices of a wind turbine. *Wind Energy*, 13(8):705–715, 2010a. doi: https://doi.org/10.1002/we.391. URL `https://onlinelibrary.wiley.com/doi/abs/10.1002/we.391`.

S. Ivanell, R. Mikkelsen, J. N. Sørensen, and D. Henningson. Stability analysis of the tip vortices of a wind turbine. *Wind Energy*, 13(8):705–715, 2010b. doi: https://doi.org/10.1002/we.391. URL `https://onlinelibrary.wiley.com/doi/abs/10.1002/we.391`.

N. Jenkins, A. Burton, D. Sharpe, and E. Bossanyi. *Wind Energy Handbook*. John Wiley Sons Ltd, United Kingdom, 2001. ISBN 0-4714-8997-2.

M. Jia, J. Yuan, C. Wang, H. Xia, Y. Wu, L. Zhao, T. Wei, J. Wu, L. Wang, S.-Y. Gu, L. Liu, D. Lu, R. Chen, X. Xue, and X. Dou. Long-lived high-frequency gravity waves in the atmospheric boundary layer: observations and simulations. *Atmospheric Chemistry and Physics*, 19(24):15431–15446, 2019. doi: 10.5194/acp-19-15431-2019. URL `https://acp.copernicus.org/articles/19/15431/2019/`.

R.-E. Keck, M. Maré, M. Churchfield, S. Lee, G. Larsen, and H. Madsen. On atmospheric stability in the dynamic wake meandering model. *Wind Energy*, 17, 11 2014. doi: 10.1002/we.1662.

D. W. Keith, J. F. DeCarolis, D. C. Denkenberger, D. H. Lenschow, S. L. Malyshev, S. Pacala, and P. J. Rasch. The influence of large-scale wind power on global climate. *Proceedings of the National Academy of Sciences*, 101(46):16115–16120, 2004. ISSN 0027-8424. doi: 10.1073/pnas.0406930101. URL `https://www.pnas.org/content/101/46/16115`.

S.-W. Kim, S.-U. Park, and C.-H. Moeng. Entrainment Processes in the Convective Boundary Layer with Varying Wind Shear. *Boundary-Layer Meteorology*, 108(2):221–245, 2003. ISSN 1573-1472. doi: 10.1023/A:1024170229293. URL `https://doi.org/10.1023/A:1024170229293`.

J. B. Klemp and D. K. Lilly. Numerical simulation of hydrostatic mountain waves. *Journal of Atmospheric Sciences*, 35(1):78 – 107, 1978. doi: 10.1175/1520-0469(1978)035<0078:NSOHMW>2.0.CO;2. URL `https://journals.ametsoc.org/view/journals/atsc/35/1/1520-0469_1978_035_0078_nsohmw_2_0_co_2.xml`.

T. Koblitz, A. Bechmann, A. Sogachev, N. Sørensen, and P. Réthoré. Computational fluid dynamics model of stratified atmospheric boundary-layer flow. *Wind Energy*, 18(1):75–89, 2015. doi: https://doi.org/10.1002/we.1684. URL `https://onlinelibrary.wiley.com/doi/abs/10.1002/we.1684`.

S. Lee, M. J. Churchfield, P. J. Moriarty, J. Jonkman, and J. Michalakes. A Numerical Study of Atmospheric and Wake Turbulence Impacts on Wind Turbine Fatigue Loadings. *Journal of Solar Energy Engineering*, 135(3), 02 2013. ISSN 0199-6231. doi: 10.1115/1.4023319. URL `https://doi.org/10.1115/1.4023319`. 031001.

L. Lignarolo, D. Mehta, R. Stevens, A. Yilmaz, G. van Kuik, S. Andersen, C. Meneveau, C. Ferreira, D. Ragni, J. Meyers, G. van Bussel, and J. Holierhoek. Validation of four les and a vortex model against stereo-piv measurements in the near wake of an actuator disc and a wind turbine. *Renewable energy*, 94:510–523, 2016. ISSN 0960-1481. doi: 10.1016/j.renene.2016.03.070.

D. K. Lilly. Models of cloud-topped mixed layers under a strong inversion. *Quarterly Journal of the Royal Meteorological Society*, 94(401):292–309, 1968. doi: https://doi.org/10.1002/qj.49709440106. URL `https://rmets.onlinelibrary.wiley.com/doi/abs/10.1002/qj.49709440106`.

L. Liu, S. N. Gadde, and R. J. Stevens. Universal Wind Profile for Conventionally Neutral Atmospheric Boundary Layers. *Physical Review Letters*, 126(10), 2021. ISSN 10797114. doi: 10.1103/PhysRevLett.126.104502.

R. R. Long. Some Aspects of the Flow of Stratified Fluids. *Tellus*, 7(3):341–357, 1955. ISSN 0040-2826. doi: 10.3402/tellusa.v7i3.8900.

F. Lott. Linear mountain drag and averaged pseudo-momentum flux profiles in the presence of trapped lee waves. *Tellus, Series A: Dynamic Meteorology and Oceanography*, 50(1):12–25, 1998. ISSN 02806495. doi: 10.3402/tellusa.v50i1.14509.

H. Lu and F. Porté-Agel. Large-eddy simulation of a very large wind farm in a stable atmospheric boundary layer. *Physics of Fluids*, 23(6):065101, June 2011. ISSN 1070-6631, 1089-7666. doi: 10.1063/1.3589857. URL `http://aip.scitation.org/doi/10.1063/1.3589857`.

M. Magnusson and A.-S. Smedman. Influence of atmospheric stability on wind turbine wakes. *Wind Engineering*, 18(3):139–152, 1994. ISSN 0309524X, 2048402X. URL `http://www.jstor.org/stable/43749538`.

J. Mann, N. Angelou, J. Arnqvist, D. Callies, E. Cantero, R. C. Arroyo, M. Courtney, J. Cuxart, E. Dellwik, J. Gottschall, S. Ivanell, P. Kühn, G. Lea, J. C. Matos, J. M. L. M. Palma, L. Pauscher, A. Peña, J. S. Rodrigo, S. Söderberg, N. Vasiljevic, and C. V. Rodrigues. Complex terrain experiments in the new european wind atlas. *Philosophical Transactions of the Royal Society A: Mathematical, Physical and Engineering Sciences*, 375(2091):20160101, 2017. doi: 10.1098/rsta.2016.0101. URL `https://royalsocietypublishing.org/doi/abs/10.1098/rsta.2016.0101`.

N. Marathe, A. Swift, B. Hirth, R. Walker, and J. Schroeder. Characterizing power performance and wake of a wind turbine under yaw and blade pitch. *Wind Energy*, 19, 07 2016. doi: 10.1002/we.1875.

P. J. Mason and D. J. Thomson. Large-eddy simulations of the neutral-static-stability planetary boundary layer. *Quarterly Journal of the Royal Meteorological Society*, 113(476):413–443, 1987. doi: https://doi.org/10.1002/qj.49711347602. URL `https://rmets.onlinelibrary.wiley.com/doi/abs/10.1002/qj.49711347602`.

D. Medici and P. H. Alfredsson. Measurements on a wind turbine wake: 3d effects and bluff body vortex shedding. *Wind Energy*, 9(3):219–236, 2006. doi: https://doi.org/10.1002/we.156. URL `https://onlinelibrary.wiley.com/doi/abs/10.1002/we.156`.

D. Mehta, A. van Zuijlen, B. Koren, J. Holierhoek, and H. Bijl. Large eddy simulation of wind farm aerodynamics: A review. *Journal of Wind Engineering and Industrial Aerodynamics*, 133:1–17, 2014. ISSN 0167-6105. doi: https://doi.org/10.1016/j.jweia.2014.07.002. URL `https://www.sciencedirect.com/science/article/pii/S0167610514001391`.

J. M. Meneveau and Charles. Optimal turbine spacing in fully developed wind farm boundary layers. *Wind Energy*, (April 2011):1–20, 2011. doi: 10.1002/we.469.

J. Meyers and C. Meneveau. Large Eddy Simulations of large wind-turbine arrays in the atmospheric boundary layer. *48th AIAA Aerospace Sciences Meeting Including the New Horizons Forum and Aerospace Exposition*, (January):1–10, 2010a. doi: 10.2514/6.2010-827.

J. Meyers and C. Meneveau. Large Eddy Simulations of large wind-turbine arrays in the atmospheric boundary layer. *48th AIAA Aerospace Sciences Meeting Including the New Horizons Forum and Aerospace Exposition*, (January):1–10, 2010b. doi: 10.2514/6.2010-827.

J. D. Mirocha, D. A. Rajewski, N. Marjanovic, J. K. Lundquist, B. Kosović, C. Draxl, and M. J. Churchfield. Investigating wind turbine impacts on near-wake flow using profiling lidar data and large-eddy simulations with an actuator disk model. *Journal of Renewable and Sustainable Energy*, 7(4):043143, 2015. doi: 10.1063/1.4928873. URL `https://doi.org/10.1063/1.4928873`.

C.-H. Moeng and P. P. Sullivan. A Comparison of Shear- and Buoyancy-Driven Planetary Boundary Layer Flows. *Journal of Atmospheric Sciences*, 51(7):999–1022, 1994. doi: 10.1175/1520-0469(1994)051<0999:ACOSAB>2.0.CO;2. URL `https://journals.ametsoc.org/view/journals/atsc/51/7/1520-0469_1994_051_0999_acosab_2_0_co_2.xml`.

M. Momen and E. Bou-Zeid. Large-eddy simulations and damped-oscillator models of the unsteady ekman boundary layer. *Journal of the Atmospheric Sciences*, 73(1):25 – 40, 2016. doi: 10.1175/JAS-D-15-0038.1. URL `https://journals.ametsoc.org/view/journals/atsc/73/1/jas-d-15-0038.1.xml`.

W. Munters, C. Meneveau, and J. Meyers. Turbulent Inflow Precursor Method with Time-Varying Direction for Large-Eddy Simulations and Applications to Wind Farms. *Boundary-Layer Meteorology*, 159(2): 305–328, 2016. ISSN 15731472. doi: 10.1007/s10546-016-0127-z. URL `https://doi.org/10.1007/s10546-016-0127-z`.

C. J. Nappo. *An Introduction to Atmospheric Gravity Waves*. Academic Press, 525 B Street, Suite 1900, San Diego, California 92101-4495, USA, second edition, 2002.

C. J. Nappo. Wave Stress. *International Geophysics*, 102:159–179, 2012. ISSN 00746142. doi: 10.1016/B978-0-12-385223-6.00006-9.

G. D. Nastrom and D. C. Fritts. Sources of mesoscale variability of gravity waves. Part I: topographic excitation, 1992. ISSN 00224928.

S. NICHOLLS. Aircraft observations of the Ekman layer during the Joint Air-Sea Interaction Experiment. *Quarterly Journal of the Royal Meteorological Society*, 111(468):391–426, 1985. ISSN 00359009. doi: 10.1256/smsqj.46806.

K. Nilsson, S. Ivanell, K. S. Hansen, R. Mikkelsen, J. N. Sørensen, S.-P. Breton, and D. Henningson. Large-eddy simulations of the Lillgrund wind farm. *Wind Energy*, 18(3):449–467, 2015. doi: https://doi.org/10.1002/we.1707. URL `https://onlinelibrary.wiley.com/doi/abs/10.1002/we.1707`.

N. G. Nygaard. Wakes in very large wind farms and the effect of neighbouring wind farms. *Journal of Physics: Conference Series*, 524(1), 2014. ISSN 17426596. doi: 10.1088/1742-6596/524/1/012162.

S. J. Ollier, S. J. Watson, and C. Montavon. Atmospheric gravity wave impacts on an offshore wind farm. *Journal of Physics: Conference Series*, 1037:072050, June 2018. ISSN 1742-6588, 1742-6596. doi: 10.1088/1742-6596/1037/7/072050. URL `https://iopscience.iop.org/article/10.1088/1742-6596/1037/7/072050`.

A. Parente, C. Gorlé, J. Beeck, and C. Benocci. A comprehensive modelling approach for the neutral atmospheric boundary layer: Consistent inflow conditions, wall function and turbulence model. *Boundary-Layer Meteorology*, 140:411–428, 09 2011. doi: 10.1007/s10546-011-9621-5.

M. P. Paul van der Laan and N. N. Sørensen. Why the Coriolis force turns a wind farm wake clockwise in the Northern Hemisphere. *Wind Energy Science Discussions*, 25(December):1–12, 2016. ISSN 2366-7443. doi: 10.5194/wes-2016-46.

M. P. Paul van der Laan, K. S. Hansen, N. N. Sørensen, and P. E. Réthoré. Predicting wind farm wake interaction with RANS: An investigation of the Coriolis force. *Journal of Physics: Conference Series*, 625(1), 2015. ISSN 17426596. doi: 10.1088/1742-6596/625/1/012026.

J. G. Pedersen, S. E. Gryning, and M. Kelly. On the Structure and Adjustment of Inversion-Capped Neutral Atmospheric Boundary-Layer Flows: Large-Eddy Simulation Study. *Boundary-Layer Meteorology*, 153(1):43–62, 2014a. ISSN 00068314. doi: 10.1007/s10546-014-9937-z.

J. G. Pedersen, S.-E. Gryning, and M. Kelly. On the Structure and Adjustment of Inversion-Capped Neutral Atmospheric Boundary-Layer Flows: Large-Eddy Simulation Study. *Boundary-Layer Meteorology*, 153(1):43–62, Oct. 2014b. ISSN 0006-8314, 1573-1472. doi: 10.1007/s10546-014-9937-z. URL `http://link.springer.com/10.1007/s10546-014-9937-z`.

F. Porté-Agel, M. Bastankhah, and S. Shamsoddin. Wind-Turbine and Wind-Farm Flows: A Review. *Boundary-Layer Meteorology*, 174(1):1–59, 2020. ISSN 1573-1472. doi: 10.1007/s10546-019-00473-0. URL `https://doi.org/10.1007/s10546-019-00473-0`.

P. Queney. The Problem of Air Flow Over Mountains: A Summary of Theoretical Studies. *Bulletin of the American Meteorological Society*, 29(1):16–26, Jan. 1948. ISSN 0003-0007, 1520-0477. doi: 10.1175/1520-0477-29.1.16. URL `http://journals.ametsoc.org/doi/10.1175/1520-0477-29.1.16`.

G. Rampanelli and D. Zardi. A Method to Determine the Capping Inversion of the Convective Boundary Layer. *JOURNAL OF APPLIED METEOROLOGY*, 43:9, 2004.

R. M. Rauber and M. Ramamurthy. *Mesoscale Meteorology: Cloud and Precipitation Bands*, volume 3. Elsevier, second edition edition, 2015. ISBN 9780123822260. doi: 10.1016/B978-0-12-382225-3.00215-2. URL `http://dx.doi.org/10.1016/B978-0-12-382225-3.00215-2`.

O. Reynolds. Iv. on the dynamical theory of incompressible viscous fluids and the determination of the criterion. *Philosophical Transactions of the Royal Society of London. (A.)*, 186:123–164, 1895. doi: 10.1098/rsta.1895.0004. URL `https://royalsocietypublishing.org/doi/abs/10.1098/rsta.1895.0004`.

D. F. G. Richard J.A.M. Stevens and C. Meneveau. Effects of turbine spacing on the power output of extended wind-farms. (2015):1–12, 2015. doi: 10.1002/we.1835.

J. S. Rodrigo, R. C. Arroyo, P. Gancarski, F. B. Guillén, M. Avila, J. Barcons, A. Folch, D. Cavar, D. Allaerts, J. Meyers, and A. Dutrieux. Comparing Meso-Micro Methodologies for Annual Wind Resource Assessment and Turbine Siting at Cabauw. *Journal of Physics: Conference Series*, 1037(7), 2018. ISSN 17426596. doi: 10.1088/1742-6596/1037/7/072030.

J. Sachsperger, S. Serafin, and V. Grubišić. Lee waves on the boundary-layer inversion and their dependence on free-atmospheric stability. *Frontiers in Earth Science*, 3:70, 2015. ISSN 2296-6463. doi: 10.3389/feart.2015.00070. URL `https://www.frontiersin.org/article/10.3389/feart.2015.00070`.

L. Sætran and J. Bartl. Invitation to the 2015 “ Blind test 4 ” Workshop Combined power output of two in-line turbines at different inflow conditions Abstract : Schedule : Background : Motivation :. pages 1–16, 2015.

J. Sanz Rodrigo, M. Churchfield, and B. Kosovic. A methodology for the design and testing of atmospheric boundary layer models for wind energy applications. *Wind Energy Science*, 2(1):35–54, 2017. ISSN 23667451. doi: 10.5194/wes-2-35-2017.

S. Sarmast, A. Segalini, R. F. Mikkelsen, and S. Ivanell. Comparison of the near-wake between actuator-line simulations and a simplified vortex model of a horizontal-axis wind turbine. *Wind Energy*, 19 (3):471–481, 2016. doi: https://doi.org/10.1002/we.1845. URL `https://onlinelibrary.wiley.com/doi/abs/10.1002/we.1845`.

H. Schümann, F. Pierella, and L. Sætran. Experimental investigation of wind turbine wakes in the wind tunnel. *Energy Procedia*, 35:285–296, 2013. ISSN 1876-6102. doi: https://doi.org/10.1016/j.egypro.2013.07.181. URL `https://www.sciencedirect.com/science/article/pii/S1876610213012678`. DeepWind'2013 – Selected papers from 10th Deep Sea Offshore Wind RD Conference, Trondheim, Norway, 24 – 25 January 2013.

R. S. Scorer. Theory of waves in the lee of mountains. *Quarterly Journal of the Royal Meteorological Society*, 75(323):41–56, 1949. ISSN 1477870X. doi: 10.1002/qj.49707532308.

A. Segalini and J. Å. Dahlberg. Blockage effects in wind farms. *Wind Energy*, 23(2):120–128, 2020. ISSN 10991824. doi: 10.1002/we.2413.

A. Singh, K. B. Howard, and M. Guala. On the homogenization of turbulent flow structures in the wake of a model wind turbine. *Physics of Fluids*, 26(2), 2014. ISSN 10897666. doi: 10.1063/1.4863983.

I. N. Smalikho, V. A. Banakh, Y. L. Pichugina, W. A. Brewer, R. M. Banta, J. K. Lundquist, and N. D. Kelley. Lidar investigation of atmosphere effect on a wind turbine wake. *Journal of Atmospheric and Oceanic Technology*, 30(11):2554 – 2570, 2013. doi: 10.1175/JTECH-D-12-00108.1. URL `https://journals.ametsoc.org/view/journals/atot/30/11/jtech-d-12-00108_1.xml`.

A.-S. Smedman, H. Bergström, and B. Grisogono. Evolution of stable internal boundary layers over a cold sea. *Journal of Geophysical Research: Oceans*, 102(C1):1091–1099, Jan. 1997. ISSN 01480227. doi: 10.1029/96JC02782. URL `http://doi.wiley.com/10.1029/96JC02782`.

R. B. Smith. Gravity wave effects on wind farm efficiency. *Wind Energy*, 13(5):449–458, Dec. 2009. ISSN 10954244, 10991824. doi: 10.1002/we.366. URL `http://doi.wiley.com/10.1002/we.366`.

A. Sogachev, M. Kelly, and M. Y. Leclerc. Consistent Two-Equation Closure Modelling for Atmospheric Research: Buoyancy and Vegetation Implementations. *Boundary-Layer Meteorology*, 145(2):307–327, 2012. ISSN 1573-1472. doi: 10.1007/s10546-012-9726-5. URL `https://doi.org/10.1007/s10546-012-9726-5`.

I. Sood, W. Munters, and J. Meyers. Effect of conventionally neutral boundary layer height on turbine performance and wake mixing in offshore windfarms. *Journal of Physics: Conference Series*, 1618 (6), 2020. ISSN 17426596. doi: 10.1088/1742-6596/1618/6/062049.

Z. Sorbjan. Effects Caused by Varying the Strength of the Capping Inversion Based on a Large Eddy Simulation Model of the Shear-Free Convective Boundary Layer. *Journal of the Atmospheric Sciences*, 53(14):2015–2024, 07 1996. ISSN 0022-4928. doi: 10.1175/1520-0469(1996)053<2015:ECBVTS>2.0.CO;2. URL `https://doi.org/10.1175/1520-0469(1996)053<2015:ECBVTS>2.0.CO;2`.

A. N. Starkov, P. P. Bezroukikh, M. M. R. D. I. o. E. E. R. Borisenko Moscow (RU)], and L. R. N. L. Landberg Roskilde (DK)]. Russian wind atlas. Technical report, Denmark, 2000.

N. Stergiannis, C. Lacor, J. V. Beeck, and R. Donnelly. CFD modelling approaches against single wind turbine wake measurements using RANS. *Journal of Physics: Conference Series*, 753(3), 2016. ISSN 17426596. doi: 10.1088/1742-6596/753/3/032062.

R. J. Stevens, J. Graham, and C. Meneveau. A concurrent precursor inflow method for large eddy simulations and applications to finite length wind farms. *Renewable Energy*, 68:46–50, 2014. ISSN 0960-1481. doi: https://doi.org/10.1016/j.renene.2014.01.024. URL `https://www.sciencedirect.com/science/article/pii/S0960148114000536`.

R. B. Stull. *An Introduction to Boundary Layer Meteorology*. KLUWER ACADEMIC PUBLISHERS, P.O. 80x 17. 3300 AA Dordred1t. The NetheflandS., first edition, 1988.

B. Subramanian, N. Chokani, and R. S. Abhari. Impact of atmospheric stability on wind turbine wake evolution. *Journal of Wind Engineering and Industrial Aerodynamics*, 176(January 2017):174–182, 2018. ISSN 01676105. doi: 10.1016/j.jweia.2018.03.014. URL `https://doi.org/10.1016/j.jweia.2018.03.014`.

P. P. Sullivan, J. C. McWilliams, and C.-H. Moeng. A subgrid-scale model for large-eddy simulation of planetary boundary-layer flows. *Boundary-Layer Meteorology*, 71(3):247–276, 1994. ISSN 1573-1472. doi: 10.1007/BF00713741. URL `https://doi.org/10.1007/BF00713741`.

M. Tabib, M. S. Siddiqui, E. Fonn, A. Rasheed, and T. Kvamsdal. Near wake region of an industrial scale wind turbine: comparing LES-ALM with LES-SMI simulations using data mining (POD). *Journal of Physics: Conference Series*, 854:012044, may 2017. doi: 10.1088/1742-6596/854/1/012044. URL `https://doi.org/10.1088/1742-6596/854/1/012044`.

H. Tennekes. A model for the dynamics of the inversion above a convective boundary layer. *Journal of Atmospheric Sciences*, 30(4):558 – 567, 1973. doi: 10.1175/1520-0469(1973)030<0558:AMFTDO>2.0.CO;2. URL `https://journals.ametsoc.org/view/journals/atsc/30/4/1520-0469_1973_030_0558_amftdo_2_0_co_2.xml`.

M. Tjernström and A.-S. Smedman. The vertical turbulence structure of the coastal marine atmospheric boundary layer. *Journal of Geophysical Research: Oceans*, 98(C3):4809–4826, Mar. 1993. ISSN 01480227. doi: 10.1029/92JC02610. URL `http://doi.wiley.com/10.1029/92JC02610`.

I. Troen and E. Lundtang Petersen. *European Wind Atlas*. Risø National Laboratory, 1989. ISBN 87-550-1482-8.

G. K. Vallis. *Atmospheric and oceanic fluid dynamics: fundamentals and large-scale circulation*. Cambridge University Press, Cambridge, second edition, 2017.

M. P. Van Der Laan, M. Kelly, and M. Baungaard. A pressure-driven atmospheric boundary layer model satisfying Rossby and Reynolds number similarity. *Wind Energy Science*, 6(3):777–790, 2021. ISSN 23667451. doi: 10.5194/wes-6-777-2021.

M. C. vanZanten, P. G. Duynkerke, and J. W. M. Cuijpers. Entrainment parameterization in convective boundary layers. *Journal of the Atmospheric Sciences*, 56(6):813 – 828, 1999. doi: 10.1175/1520-0469(1999)056<0813:EPICBL>2.0.CO;2. URL `https://journals.ametsoc.org/view/journals/atsc/56/6/1520-0469_1999_056_0813_epicbl_2.0.co_2.xml`.

L. Vermeer, J. Sørensen, and A. Crespo. Wind turbine wake aerodynamics. *Progress in Aerospace Sciences*, 39(6):467–510, 2003. ISSN 0376-0421. doi: https://doi.org/10.1016/S0376-0421(03)00078-2. URL `https://www.sciencedirect.com/science/article/pii/S0376042103000782`.

P. J. H. Volker, J. Badger, A. N. Hahmann, and S. Ott. The explicit wake parametrisation v1.0: a wind farm parametrisation in the mesoscale model wrf. *Geoscientific Model Development*, 8(11):3715–3731, 2015. doi: 10.5194/gmd-8-3715-2015. URL `https://gmd.copernicus.org/articles/8/3715/2015/`.

S. B. Vosper. Inversion effects on mountain lee waves. *Quarterly Journal of the Royal Meteorological Society*, 130(600 PART A):1723–1748, 2004. ISSN 00359009. doi: 10.1256/qj.03.63.

T. T. Warner. *Numerical Weather and Climate Prediction*. Cambridge University Press, 2010. doi: 10.1017/CBO9780511763243.

X. Wei, B. Huang, T. Kanemoto, and L. Wang. Near wake study of counter-rotating horizontal axis tidal turbines based on PIV measurements in a wind tunnel. *Journal of Marine Science and Technology*, 22(1):11–24, 2017. ISSN 1437-8213. doi: 10.1007/s00773-016-0389-7. URL `https://doi.org/10.1007/s00773-016-0389-7`.

J. Whale, C. Anderson, R. Bareiss, and S. Wagner. An experimental and numerical study of the vortex structure in the wake of a wind turbine. *Journal of Wind Engineering and Industrial Aerodynamics*, 84

(1):1–21, 2000. ISSN 0167-6105. doi: https://doi.org/10.1016/S0167-6105(98)00201-3. URL `https://www.sciencedirect.com/science/article/pii/S0167610598002013`.

K. Wu and F. Porté-Agel. Flow Adjustment Inside and Around Large Finite-Size Wind Farms. *Energies*, 10(12):2164, Dec. 2017. ISSN 1996-1073. doi: 10.3390/en10122164. URL `http://www.mdpi.com/1996-1073/10/12/2164`.

K. L. Wu and F. Porté-Agel. Flow adjustment inside and around large finite-size wind farms. *Energies*, 10(12):4–9, 2017. ISSN 19961073. doi: 10.3390/en10122164.

Y. T. Wu and F. Porté-Agel. Modeling turbine wakes and power losses within a wind farm using LES: An application to the Horns Rev offshore wind farm. *Renewable Energy*, 75:945–955, 2015. ISSN 18790682. doi: 10.1016/j.renene.2014.06.019.

Y.-T. Wu and F. Porté-Agel. Large-Eddy Simulation of Wind-Turbine Wakes: Evaluation of Turbine Parametrisations. *Boundary-Layer Meteorology*, 138(3):345–366, Mar. 2011. ISSN 0006-8314, 1573-1472. doi: 10.1007/s10546-010-9569-x. URL `http://link.springer.com/10.1007/s10546-010-9569-x`.

Y.-T. Wu and F. Porté-Agel. Simulation of Turbulent Flow Inside and Above Wind Farms: Model Validation and Layout Effects. *Boundary-Layer Meteorology*, 146(2):181–205, Feb. 2013. ISSN 0006-8314, 1573-1472. doi: 10.1007/s10546-012-9757-y. URL `http://link.springer.com/10.1007/s10546-012-9757-y`.

J. C. Wyngaard. *Turbulence in the Atmosphere*. Cambridge University Press, 2010. doi: 10.1017/CBO9780511840524.

B. W. Yan, Q. S. Li, Y. C. He, and P. W. Chan. RANS simulation of neutral atmospheric boundary layer flows over complex terrain by proper imposition of boundary conditions and modification on the k-ϵ model. *Environmental Fluid Mechanics*, 16(1):1–23, 2016. ISSN 1573-1510. doi: 10.1007/s10652-015-9408-1. URL `https://doi.org/10.1007/s10652-015-9408-1`.

X. Yang, K. B. Howard, M. Guala, and F. Sotiropoulos. Effects of a three-dimensional hill on the wake characteristics of a model wind turbine. *Physics of Fluids*, 27(2):1–18, 2015. ISSN 10897666. doi: 10.1063/1.4907685.

D. V. Zaitseva, M. A. Kallistratova, V. S. Lyulyukin, R. D. Kouznetsov, and D. D. Kuznetsov. The Effect of Internal Gravity Waves on Fluctuations in Meteorological Parameters of the Atmospheric Boundary Layer. *Izvestiya, Atmospheric and Oceanic Physics*, 54(2):173–181, 2018. ISSN 1555-628X. doi: 10.1134/S0001433818020160. URL `https://doi.org/10.1134/S0001433818020160`.

W. Zhang, C. D. Markfort, and F. Porté-Agel. Near-wake flow structure downwind of a wind turbine in a turbulent boundary layer. *Experiments in Fluids*, 52(5):1219–1235, 2012. ISSN 1432-1114. doi: 10.1007/s00348-011-1250-8. URL `https://doi.org/10.1007/s00348-011-1250-8`.

W. Zhang, C. D. Markfort, and F. Porté-Agel. Wind-Turbine Wakes in a Convective Boundary Layer: A Wind-Tunnel Study. *Boundary-Layer Meteorology*, 146(2):161–179, 2013. ISSN 1573-1472. doi: 10.1007/s10546-012-9751-4. URL `https://doi.org/10.1007/s10546-012-9751-4`.

S. Zilitinkevich and A. Baklanov. Calculation Of The Height Of The Stable Boundary Layer In Practical Applications. *Boundary-Layer Meteorology*, 105(3):389–409, 2002. ISSN 1573-1472. doi: 10.1023/A:1020376832738. URL `https://doi.org/10.1023/A:1020376832738`.

Numerical Study On The Impact Of Self Induced Gravity Waves On Offshore Wind Farms

FACULTY OF AEROSPACE ENGINEERING,
WIND ENERGY RESEARCH GROUP,
DELFT UNIVERSITY OF TECHNOLOGY,
Kluyverweg 1, 2629HS
Delft, The Netherlands